UNIVERSITÀ DEGLI STUDI DI TRIESTE

XXXII CICLO DEL DOTTORATO DI RICERCA IN FISICA

SOLVATION EFFECTS OF IONIC LIQUID/WATER MIXTURES ON BIOMOLECULES

Settore scientifico-disciplinare: **FIS/03 – Fisica della Materia**

DOTTORANDA
CETTINA BOTTARI

COORDINATORE
PROF. FRANCESCO LONGO

SUPERVISORE DI TESI
DR. CLAUDIO MASCIOVECCHIO

CO-SUPERVISORE DI TESI
DR.SSA BARBARA ROSSI

ANNO ACCADEMICO 2018/2019

Contents

Introduction

Ionic liquids (ILs) belong to a broad class of ionic compounds that, differently from conventional salts, are usually liquid at T $<$ 100°C. They are characterized by vanishing vapour pressure, good thermal stability, high ion density and ionic conductivity. Thanks to the large variety of available ions, the physico-chemical properties of ILs can be modulated by careful selection of both cation and anion with specific characteristics for tailored applications. A more convenient strategy for an efficient tuning of the performances of ILs consists in mixing ILs with other ionic or molecular liquids, such as e.g. water. It is observed that addition of water to ILs allows to improve some of their properties and performances, especially for applications in biological field. For instance, recent studies reported on the capability of IL/water solutions to enhance the structural stability of proteins, enzymes and deoxyribonucleic acid (DNA) also at high temperatures.

This PhD thesis aims to show the usefulness of synchrotron-based UV Resonance Raman (SR-UVRR) spectroscopy for investigating i) the structural dynamics of IL/water solutions and ii) the solvation effects of these IL-based solvents on bio-molecules, such as peptides and DNA. UVRR spectroscopy exhibits several advantages with respect to conventional spontaneous Raman spectroscopy, as the significant increment of the detection limit that allows to study the samples in very high diluted conditions and the selective enhancement of the Raman cross section of vibrations associated to specific molecular groups of the same system. Thanks to the unique tunability of the synchrotron emission, the UVRR spectra of aqueous solutions of imidazolium-based ILs have been collected at different wavelengths finely matching with the resonance transitions occurring in the system. These spectra showed to have good

sensitivity to the modifications induced on the local structure of solutions of ILs by i) the change of the anion and ii) the substitution on the imidazolium ring of progressively longer alkyl-chains. Additionally, some UVRR signals are specifically informative on the effect induced by addition of water on the strength of hydrogen bonds (H-bonds) in IL-water solutions. The molecular view provided by SR-UVRR experiments has been further complemented by the structural parameters extracted by Small Angle Neutron Scattering (SANS) measurements performed on the same IL/water mixtures.

The investigation of the structure-dynamic relationship in IL/water solutions is the preliminary step for the deep comprehension of the effects of these mixtures on the solvation dynamics of molecules of biological interest, such as peptides and DNA. This is an issue of special interest by considering that the solute-solvent interactions are strongly related to the biological activity of bio-macromolecules. Some results will be presented in this thesis, concerning the case of two different type of bio-systems:

i) small peptides dissolved in IL/water solutions: the UVRR spectra of peptides contain several spectroscopic markers of the structural rearrangement induced by the hydration shell on peptides, such as the Amide bands that are usually not well detectable in spontaneous spectra. The analysis of these spectral features can provide insights on the peculiar effect induced on the hydration dynamics of peptides by different ILs;

ii) DNA dissolved in IL/water solutions: a suitable choice of the exciting radiation allows to collect UVRR spectra of DNA where the vibrational signals associated to the different nitrogenous bases are selectively enhanced. This gives the unique opportunity to disentangle specific bands in the spectra of DNA that appear usually very complex. Such approach can be conveniently used to obtain insights on the molecular mechanism responsible of the different thermal stability exhibited by DNA structure in the presence of different IL/water solutions. UV absorbance and circular dichroism measurements can complement the UVRR results in order to obtain a comprehensive picture of the solute-solvent interactions in DNA/ILs systems.

The present thesis is organized as it follows:

Chapter 1: the basics of the quantum theory of Raman spectroscopy are reported, with particular emphasis to the Resonance Raman effect;

Chapter 2: the synchrotron-based Resonance Raman spectroscopic instrument developed at BL10.2-IUVS beamline of Elettra synchrotron radiation facility is briefly described;

Chapter 3: the chapter reports on the investigation of local structure and intermolecular interactions in solution of imidazolium-based ILs as probed mainly by synchrotron-based UV Resonance Raman scattering;

Chapter 4: the case of solvation of the tripeptide glutathione in aqueous solutions of imidazolium-based ILs is addressed with the aim to investigate the role of the specific peptide-IL interactions in the hydration dynamics of this small peptide;

Chapter 5: the chapter reports some results on the thermal stability of DNA in IL/water mixtures with particular attention to the role played by ILs in stabilizing the DNA natural conformation.

Chapter 6: this chapter collects some complementary results concerning the usefulness of UVRR technique for investigating hydrophobic/hydrophilic effects in hydration water.

Chapter 1

Introduction to Resonance Raman Spectroscopy

1.1 Light scattering and Raman effect

The phenomenon of the scattering of light refers to the process in which incident photons with characteristic energy and momentum are diffused due to the interaction with matter. If the energy of the incident photon is the same of the diffused one we refer to "elastic scattering" otherwise it is called "inelastic scattering". For simplicity, we will consider a diatomic molecule [1, 2]. In the scattering process the oscillating electric vector of the incident electromagnetic field induces on the molecules an oscillating electric dipole moment $\bar{\mu}$. The induced electric dipole moment is proportional to the incident electromagnetic vector $\bar{E}$ through the polarizability tensor α that is related to the tendency of the molecules to deform their electronic cloud.

$$\bar{\mu} = \alpha \cdot \bar{E}. \tag{1.1}$$

Each component can be expressed as:

$$\mu_\rho = \sum_{\sigma=x}^{z} \alpha_{\rho\sigma} E_\sigma. \tag{1.2}$$

where the $\alpha_{\rho\sigma}$ refers to the component of the tensor α. The electric field $\bar{E}$ is related to the frequency ν_0 of the incident electromagnetic wave by the relation

$E_\sigma = E(0)_\sigma \cos(2\pi\nu_0 t)$. Therefore, the components of the induced dipole can be written as:

$$\mu_\rho = \sum_{\sigma=x}^{z} \alpha_{\rho\sigma} E(0)_\sigma \cos(2\pi\nu_0 t). \tag{1.3}$$

Assuming harmonic vibrations by the diatomic molecule, the time dependence of the nuclear normal coordinates Q_k can be expressed as:

$$Q_k = Q(0)_k \cos(2\pi\nu t). \tag{1.4}$$

The variation of the polarizability α due to the molecular vibrations, can be described by expanding each component in Taylor series of Q:

$$\alpha_{\rho\sigma} = \alpha(0)_{\rho\sigma} + \sum_k \left(\frac{\partial\alpha_{\rho\sigma}}{\partial Q_k}\right)_0 + \frac{1}{2}\sum_{k.l}\left(\frac{\partial^2\alpha_{\rho\sigma}}{\partial Q_k \partial Q_l}\right)_0 Q_k Q_l. \tag{1.5}$$

By neglecting the higher order terms, the induced dipole moment becomes:

$$\mu_\rho Q_k = \sum_{\sigma=x}^{z} \alpha_{\rho\sigma} E(0)_\sigma \cos(2\pi\nu_0 t) + \tag{1.6}$$

$$+\frac{1}{2}\sum_{\sigma=x}^{z} E(0)_\sigma Q(0)_k \left(\frac{\partial\alpha_{\rho\sigma}}{\partial Q_k}\right)_0 [\cos[2\pi(\nu_0+\nu)t] + \cos[2\pi(\nu_0-\nu)t]].$$

Looking at the expression above, the radiation emitted by the oscillating dipole induced by the electromagnetic field on the molecule has three different components

$$\sum_{\sigma=x}^{z} \alpha(0)_{\rho\sigma} E(0)_\sigma \cos(2\pi\nu_(0)t). \tag{1.7}$$

which accounts for the Rayleigh or elastic scattering and,

$$\frac{1}{2}\sum_{\sigma=x}^{z} E(0)_\sigma Q(0)_k \left(\frac{\partial\alpha_{\rho\sigma}}{\partial Q_k}\right)_0 [\cos[2\pi(\nu_0+\nu)t] + \cos[2\pi(\nu_0-\nu)t]]. \tag{1.8}$$

for Anti Stokes and Raman Sotkes respectively. For a given a vibrational mode, the total instensity of the Raman scattering will be defined as:

$$I(\theta) = B(\nu_0 \pm \nu)^4 I_0 \left(\frac{\partial\alpha_{\rho\sigma}}{\partial Q_k}\right)_0^2 \sin^2(\theta). \tag{1.9}$$

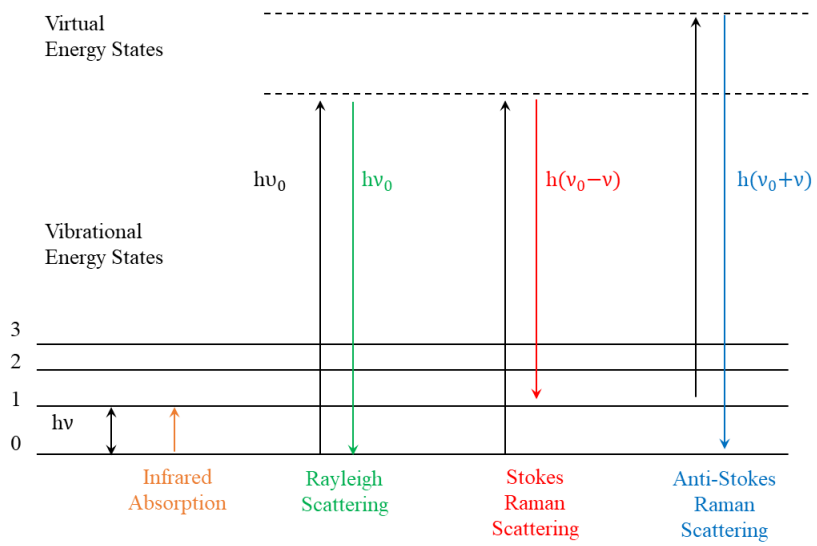

Figure 1.1: Quantum mechanical diagram describing the elastic and inelastic scatering processes.

where I_0 and θ are the intensity of the incident light and the angle between the induced dipole and the direction of the electromagnetic field respectively. Inspecting relation 1.9, it clearly appears that the intensity of Raman spectra mainly depends on two terms:

1. $\left(\frac{\partial \alpha_{\rho\sigma}}{\partial Q_k}\right)_0^2$ related to the change induced in the polarizability of the molecule by the vibration;

2. $(\nu_0 \pm \nu)^4$ that refers to the wavelength of the incident radiation.

1.2 Quantum theory of Raman Scattering

According to quantum theory, transmission and emission of a radiation is the result of the energy transfer between the eletcromagnetic field and the molecule. In Fig. 1.1 is shown the quantum dynamical description of the molecule by the elctromagnetic wave with energy $E_h\nu(0)$. As stated in the section above, there are three diferrent components related to the scattering:

- Rayleigh scattering $[E = h\nu_{(0)}]$: is the elastic scattering term, which is the most dominant scattering process with an intensity 10^{-6} lower

than the excitation light. The interaction between light and matter does not change the energy state of the molecule and therefore the scattering photons have the same energy as the incident ones.

- Stokes Raman scattering [$E = h(\nu_0 - \nu)$]: refers to the inelastic scattering process where there is an energy transfer from the electromagnetic wave to a vibrational level of the molecule. Hence the scattered photons have a lower energy (red shift) compared to the incident ones. The amount of the energy transferred corresponds to the energy necessary to promote the vibrational transition. Neverthless an intensity about 10^{-10} times lower then the excitation light, the Stokes component is the most commonly acquired in a Raman spectroscopy experiment because it is the most intense component containing molecular vibration information.

- Anti-Stokes Raman scattering [$E = h(\nu_0 + \nu)$]: is the inelastic scattering process, where a specific amount of energy is transferred from a molecular vibrations to the photons. So, conversely to the Stokes component, scattered photons have an energy higher (blue shift) compared to the incident ones. The information contained in the Anti-Stokes profile is the same as the Stoke profile but less intense.

The transition from an initial state described by the wavefunction Ψ_i to a final state Ψ_f induces a variation of the dipole moment μ_{fi}:

$$\mu_{fi} = \langle \Psi_f | \, \hat{\mu} \, | \Psi_i \rangle \neq 0. \tag{1.10}$$

Here $\hat{\mu}$ is the permanent electric dipole operator for absorption or emission (Infrared) of an electromagnetic field $\bar{E}$. For scattering phenomena, the induced dipole moment for the transition becomes:

$$\mu_{fi} = \langle \Psi_f | \, \hat{\mu} \, | \Psi_i \rangle \, \bar{E}. \tag{1.11}$$

where Ψ_f and Ψ_i are the vibrational wavefunctions of the final and initial vibrational states. To obtain a more rigorous definition of the total Raman intensity $I(\theta)$ using quantum-mechanincs, is necessary to substitute the polarizability term $\left(\frac{\partial \alpha_{\rho\sigma}}{\partial Q_k}\right)_0$ with the Raman scattering tensor $[\alpha_{\rho\sigma}]_{fi}$ which components are

obtained accordingly to the Kramers-Heisemberg expression:

$$[\alpha_{\rho\sigma}]_{10} = \frac{1}{hc} \sum_{e,k} \left\{ \frac{\langle g_1 | M_\rho | e_k \rangle \langle e_k | M_\sigma | g_0 \rangle}{v_{ek} - v_0 - v_{exc} + i\Gamma_{ek}} + \frac{\langle g_1 | M_\sigma | e_k \rangle \langle e_k | M_\rho | g_0 \rangle}{v_{ek} - v_1 - v_{exc} + i\Gamma_{ek}} \right\}. \tag{1.12}$$

In Eq. 1.12 the terms g_0 and g_1 are the vibronic wavefunctions of the ground electronic level for the starting and final vibrational levels 1 and 0 respectively, the ek are the vibronic wavefunctioins describing the virtual states, Γ_{ek} the width of the band associated with $|ek\rangle$ vibronic state and M_σ, M_ρ are the electric dipole moments. In the case of spontaneous Raman scattering, the energy of the incident electromagnetic beam v_{exc} does not coincides with any transition frequency; in this condition the Raman signal associated to a given normal mode is relatively weak.

1.3 Resonance Raman Scattering

Concerning the intensity of Raman spectra $I(\theta)$, it is necessary to distinguish between conventional and Resonance Raman (RR) scattering. In both cases the transition involves a process between the vibrational states of the electronic ground state. The difference consist in the fact that in the conventional Raman scattering the electronic excited states which take part in the process are virtual intermediate states, while in the RR scattering are real intermediate states. In the case where v_{exc} match (or is very close to) the frequency for an electronic transition of the molecule (RR conditions), the Kramers-Heisemberg expression for the Raman scattering tensor can be simplified as:

$$[\alpha_{\rho\sigma}]_{10} = \frac{1}{hc} \sum_{k} \left\{ \frac{\langle g_1 | M_\rho | e_k \rangle \langle e_k | M_\sigma | g_0 \rangle}{v_{ek} - v_0 - v_{exc} + i\Gamma_{ek}} \right\}. \tag{1.13}$$

Since only the terms having as denominator $v_{ek} - v_0 - v_{exc}$ becomes dominant, the summation in the equation above is dependent from the vibrational quantum number of the electronic excited state k. If the conditions for the RR scattering are satisfied, the scattering tensor $[\alpha_{\rho\sigma}]_{10}$ becomes greater than the case of conventional Raman scattering and the Raman intensity $I(\theta)$ associated to the corresponding normal mode is strongly enhanced. The immaginary

term that appears in the denominator of Eq.1.13 takes into account that in resonance conditions the effect of the electromagnetic perturbation is related to the life time of the excited states; hence Γ is a quantity inversely proportional to the life time of the vibronic excited states ek. In the case of an electronic transition excitation of a specific molecular portion (chromophore), some Raman normal modes result intensified more than others. The resonance active Raman signals can result orders of magnitude higher (from 3 to 8) than those out of resonance conditions. As a consequence, the sensitivity of RR technique is strongly increased. By exploiting resonance Raman effect, it is possible to analyze in a selective manner the signals coming from molecular portions of a heterogeneous sample or specific components in a complex mixture. Eq.1.13 can be further simplified, accordingly to the Born-Hoppenhaimer and the Condon approximations [1, 2] as:

$$[\alpha_{\rho\sigma}]_{10} = \langle g| M_\rho |e\rangle_0 \langle e| M_\sigma |g\rangle_0 \sum_k \left\{ \frac{\langle 1|k\rangle\langle k|0\rangle}{v_{ek} - v_0 - v_{exc} + i\Gamma_{ek}} \right\} \tag{1.14}$$

which takes the name of Albrecht's term A for RR. This term is $A \neq 0$ if two conditions are fullfilled (RR scattering selection rules):

- The transition dipole moments $\langle g| M_\rho |e\rangle_0$ and $\langle e| M_\sigma |g\rangle_0$ are both $\neq 0$;
- The Franck-Condon factors $\langle 1|k\rangle$ and $\langle k|0\rangle$ are $\neq 0$ for at least some values of k.

While the first condition is satisfied if the corresponding electronic transition is allowed, the validity of the second condition requires to consider the harmonic oscillator and symmetry of the normal modes.

Fig.1.2 represents the RR scattering process in terms of the ground and excited electronic states as a harmonic potential. In correspondence of a fundamental band of the Raman spectra, the transition from the ground state $i = 0$ at the intermediate states and from the intermediate states at the final state $f = 1$, is non-zero if:

1. the potential curves of the involved electronic states are shifted with each other ($\Delta Q \neq 0$);

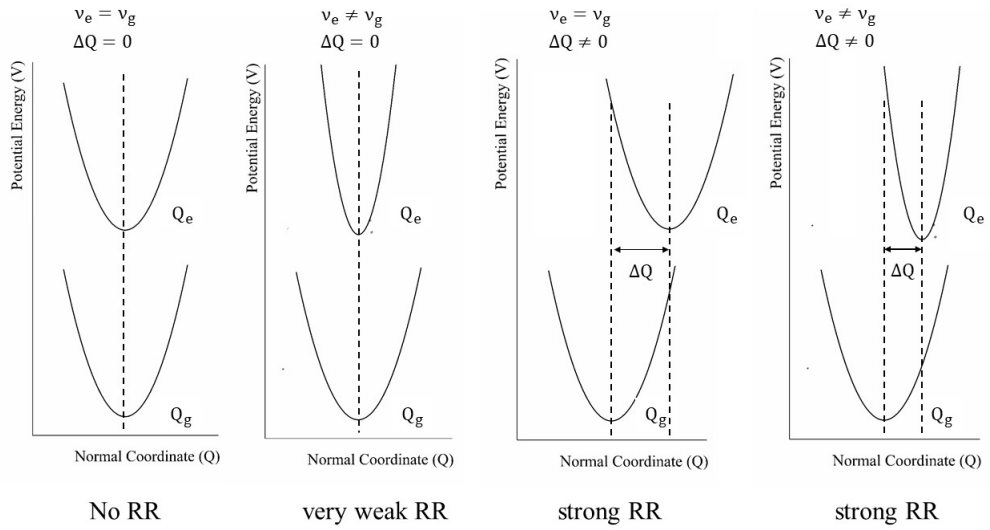

Figure 1.2: Diagrams of the potential energy (V) as a function of the normal coordinate (Q) of the ground g and excited states e.

2. there is a difference in the vibrational wavenumber between the ground and the electronic states, $v_e \neq v_a$;

3. both of the above conditions are satisfied.

Has to be noted that condition 2 is verified only for totally-symmetric vibrational modes, unless molecular symmetry changes in the excited states.

1.4 Advantages and limitations of RR spectroscopy

The vibrational spectroscopic techniques are a powerful tool to investigate the changes induced in the structure of molecular systems by chemical reactions and/or physical interactions of the system with the environment. Thanks to its capability to extract both qualitative and quantitative informations of the investigated samples, analysis of Raman spectra is suitable to be applied in a lot of research fields spanning from analytical to biological one. Compared to infrared absorption spectroscopy, both conventional and Resonance

Raman spectroscopy can be very valuable techniques for investigating samples in aqueous solution due to the relative low polarizability of water. Study of biologic molecules in physiologic conditions (i.e. aqueous solution) is strongly recommended, in order to mimic the real environment in which these systems exhibit their peculiar functionality. Water shows a very strong infrared absorption and usually the OH bending signal covers the wavenumber region between 1000-1800 cm^{-1} where the main vibrational features of organic and biological molecules fall. This seriously hampers the analysis of the vibrational fingerprints in the infrared spectra of samples dissolved in water solution. Conversely, Resonance Raman spectroscopy allows to analyze aqueous solutions without the necessity of isotopic substitution and in condition of very high diluition. This is due mainly to the greater sensitivity of RR spectroscopy with respect to its non-resonance counterpart that ensures a significant increment of the detection limit of the technique. As a matter of fact, while conventional Raman scattering can detect samples with concentrations usually no lower than 0.1 M, RR technique is capable of analyzing samples with concentrations lower than 10^{-8} M. A second advantage of the Resonance Raman technique is related to the possibility to aquire more simplifyied spectra compared to non-resonance one, due to the selective enhancement of specific signals associated to the chromophores excited in the sample. This allows to disentangle different vibrational signals in the Resonance spectra that usually are strongly superimposed in the spontaneous Raman profiles. By means of RR spectroscopy it is also possible to collect the excitation profile of a particular Raman active mode that consists in the signal intensity as a function of the excitation frequency into the absorption band. These excitation profiles contain information of the vibronic transitions associated with the particular normal mode before that the system relaxes from the electronic excited state levels. One of the limitation during a RR experiment is related to the self-absorption phenomenon that occurs when a portion of the scattered light is strongly reabsorbed by the sample. This process reduces the total scattered light also affecting the relative intensity of Raman peaks in the spectra. Another possible limitation of RR technique is the possibility of the photo degradation of the sample, due to local heating and/or photoreactions occurring at resonance conditions. In order to avoid this inconvenience, several strategies can be implemented, as it

will be discussed forward.

Chapter 2

UV Resonance Raman spectroscopic setup

2.1 Synchrotron radiation-based UV Resonance Raman spectroscopic set-up at Elettra

UV Resonance Raman (UVRR) spectroscopy is a very suitable tool for collecting specific information on the chemical nature of a large variety of systems, due to the properties of organic molecules to exhibit many and strong absorption transition in the UV range. However, it is necessary to overcome some major issue to have a full exploitation of the UVRR spectroscopy, mostly related to the need of appropriate sources:

- Up to now, there is a poor knowledge about the electronic transitions that occur in the UV region below 7 eV ($\sim$ 180 nm) due also to the difficulty of vacuum-UV spectral measurements required to explore this range. It is important to extend the UV domain investigation range in order to obtain information related to outer electronic transition in matter (i.e. up to $\sim 10-15$ eV) by selectively exploring specific orbitals and bands.

- The use of a continuous tunable excitation source permits to map the whole resonance range of the sample investigated, in order to achieve a fine matching between the exciting radiation energy and the resonance

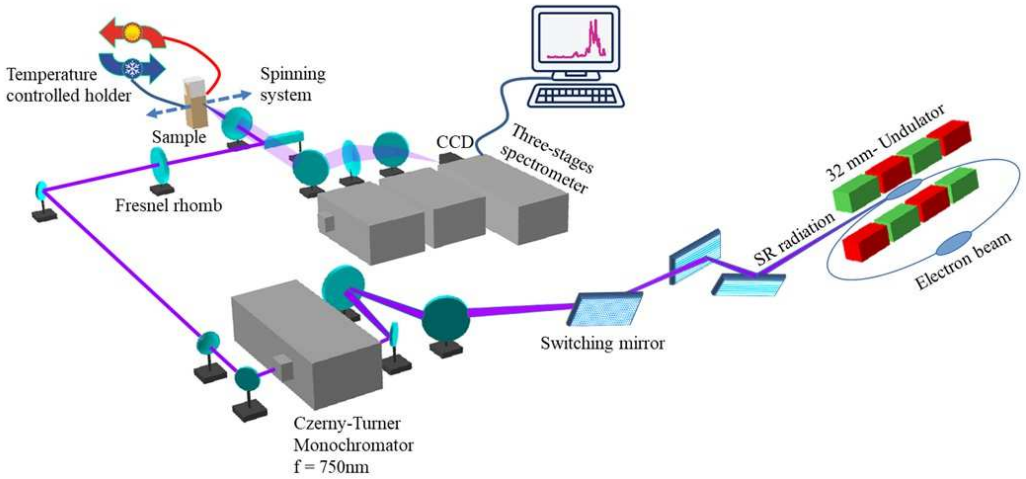

Figure 2.1: Technical layout of the SR-based setup for UVRR spectroscopy measurements at BL10.2-IUVS beamline (Ellettra synchrotron facility, Trieste, Italy).

condition of specific chromophores. This procedure allows to perform accurate UVRR spectroscopy measurements not affected by self-absorption effects.

The BL10.2-IUVS beamline at Elettra synchrotron facility in Trieste has developed an optical setup that exploits a tunable UV synchrotron radiation (SR) source for exciting and collecting UVRR spectra from different kinds of samples (i.e. solid, liquids and gels) [3]. In Fig.2.1 is shown the technical layout of the instrument. The Figure-8 32 mm undulator inserted in the radiation source of the beamline generates linear polarized SR with an energy range from 4.4 to 11 eV (corresponding to wavelengths between 113 and 280 nm) [4, 5]. This specific desing has the advantage to have a strong reduction of the total on-axis power density that is achieved with no penalty on the useful photon flux in the first harmonic of the emission spectrum. A set of two mirrors cleans the higher order harmonics components of the undulator of the beam coming from the source. This set is composed by a first coated GLIDCOP (internally water-cooled) that deviates the photons of 60° in the vertical plane and a second silicon mirror (externally water-cooled) that is used to bring back the beam parallel to the floor. In the end, a silicon switching mirror is used to guide the SR to the UVRR stage instead of the conventional high resolution

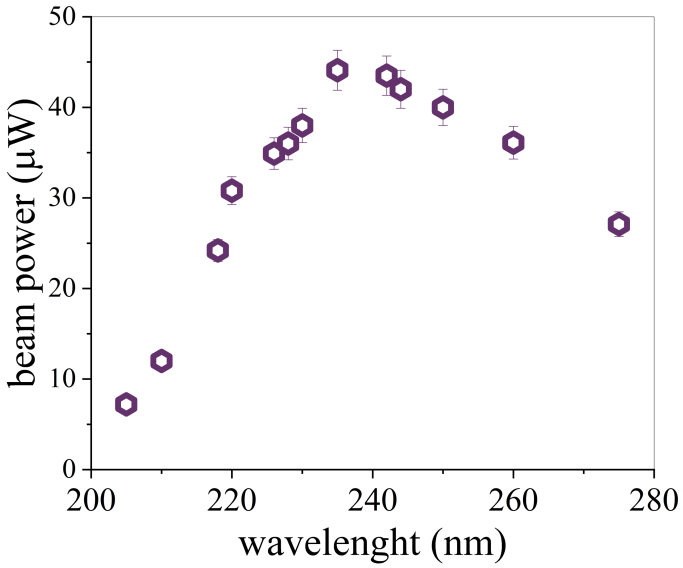

Figure 2.2: Incident radiation beam power after the monochromator (see Fig.2.1) as a function of the selected wavelength.

inelastic UV scattering (Brillouin) spectrometer [6]. To drive and focus the SR into the entrance slits of the monochromator are used specifically suited UV-enhanced coating mirrors, with a reflectivity of 90-92 % in the whole 250-285 nm range (Fig.2.1). The transport system delivers to the monochromator UV radiation with a power of $\sim$ 10 mW (at $\lambda = 270$ nm) with a typical bandwidth of $\Delta\lambda/\lambda \cong 0.01$, corresponding to $\sim$ 350 cm^{-1}. The SR is monochromatized through a Czerny-Turner monochromator (Acton SP2570 produced by Princeton instruments) operating with three exchangeable flat holographic gratings with 1800, 2400 and 3600 grooves/mm. The monochromator provides a maximum wavelenght resolution at 270 nm of $\sim$ 0.012 nm which corresponds to a half-width of $\sim$ 1.6 cm^{-1}. In Fig.2.2 is shown the beam-power of the radiation after the monochromator as a function of the selected wavelength.

It is a very important advantage to have the possibility to obtain UVRR spectra, even at these relatively low power, since it allows to measure organic samples, dye or chromophores, which are often subject to photodegradation when irradiated by UV light. After the monochromatization, there is a collimation stage through a lens and then the beam is transported to the Raman

analyzer system (Fig.2.1). There are two options for the sampling method:

1. the incident beam is focused on the sample and collected in back-scattering configuration through plano-convex lenses and mirrors; the typical size of the beam spot impinging the sample is of few mm^2;

2. the incident light is focused on the sample through the UV lens of a microscope objective (with a magnification factor typically of 2, 20 or 40 X) and the scattered radiation is collected in backscattering geometry.

Option 1 is mainly used for macro-Raman spectroscopic measurements carried out on bulk samples, such as solids, powders, liquids and gels placed in suitable optical quartz cuvettes. This kind of configuration together with the geometrical characteristics of the Raman spectroscopic setup allows the use of a large variety of sample environments. Liquids, aqueous solutions and gels can be measured in specific sample-holders which are able to thermalize the sample in a temperature range from 5° to 120°. To prevent any possible photodecomposition of the samples due to the prolonged exposure to the UV radiation, the cuvettes are subjected to a continuous spinning during the measurements in order to vary the sample volume illuminated by the radiation beam. There are other methods that can be used to prevent radiation damage such as:

- flow systems; very useful for liquid samples [7];

- rotating sample holders; used for measurements with higly absorbing materials [8].

The second sampling method is used for micro-Raman spectroscopy experiments carried out on inhomogeneous samples, surfaces or films. In the latter case, a further CCD microscope camera is employed for visualizing the position of the beam on the sample during the measurements. The three stages spectrometer (TriVista 557, Princeton Instruments) is used to analyze the Raman signal. Each stage is equipped with a selection of flat holographic gratings (1800 and 3600 grooves/mm) optimized for both UV and visible radiation. The highest wavelength that can be obtained depends on the CT mechanical rotation capability and results to be 417 nm (2.98 eV) for the 3600 lines/mm

grating and 833 nm (1.49 eV) for the 1800 lines/grating. Finally, the scattered photons are detected by a peltier-cooled UV-enhanced CCD camera. To calibrate the spectrometer is used a standard method involving cyclohexane. Polarized parallel (VV) and depolarized orthogonal (HV) UV Raman spectra can be collected by inserting in the optical path a Fresnel Rhomb Retarders (Half-Wave Retardance with broader wavelength range) and polarizers (see Fig.2.2).

Chapter 3

The peculiar effect of water in Ionic Liquids

3.1 State of art: what are Ionic Liquids?

As breafly descripted in the Introduction, ionic liquids (ILs) are a class of ionic compounds characterized by vanishing vapour pressure, good thermal stability, high ion density and ionic conductivity [9, 10]. Several applications of ILs have been explored, including their use in organic synthesis [11], electrochemical devices [12], photochemical cells [13, 14] and catalysis [15]. On the basis of their ionic nature, ILs can be divided into two broad categories: protic ILs (PILs) and aprotic ILs (AILs) (see 3.1). The former are composed by proton transfer from a Brönsted acid, AH, to a Brönsted base, B to yield, strictly speaking, a $[BH^+][A^-]$ species [16]:

$$AH + B = [BH^+][A^-]. \tag{3.1}$$

AILs contain substituents other than a proton (typically an alkyl group) at the site occupied by the labile proton in an analogous protic ionic liquid. They also require synthetic strategies which are different from the simple acid-base reactions used to obtain most PILs [17].
Thanks to the large variety of available ions, the physico-chemical properties of ILs can be modulated by careful selection of both cation and anion with specific characteristics for tailored applications [18]. A more convenient strat-

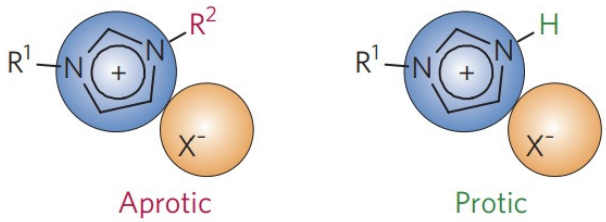

Figure 3.1: Basic types of ILs: aprotic and protic types [17].

egy for an efficient tuning of the performances of ILs consists in mixing ILs with other ionic or molecular liquids, such as e.g. water [19]. Due to the strong hygroscopic nature of most ILs, the presence of trace amounts of water was originally considered problematic for maintaining the peculiar properties of ILs, such as their characteristic nano-structured arrangment. Nowadays, it is observed that addition of water to ILs allows to improve some of their properties and performances towards specific applications. For instance, water incorporation in ILs implies an increase of the self-diffusion coefficient of cations and anions due to a general decrease in the viscosity [20], leading, to a certain extent, to larger ionic conductivity [21]. In the biological field, water represents an ideal partner for ILs and several recent studies reported on the capability of IL/water solutions to increase enzymes activity [22] and improve the stabilization of proteins [23–25]. Since water has such a high impact on the chemical-physical characteristics of ILs, both as a contaminant or as co-solvent, a detailed knowledge of the intermolecular interactions taking place in IL-water solutions is a crucial step for understanding and predicting the range of properties of ILs [26]. This appears particularly challenging in the case of ILs, where the scenario is complicated by the fact that intermolecular interactions can be strongly affected by several possible cation-anion combinations.

3.2 Hydrogen bond dynamics in IL/water mixtures

Several methods have been used to get insights into the molecular dynamics of pure ILs and mixed with water, including vibrational spectroscopy [27]. Such

techniques give the opportunity to investigate the extension and the strength of inter- and intra-molecular interactions in molecular liquids by probing to the vibrational motions of the system. For instance, collective vibrations of pure liquid water have been successfully investigated by using low-frequency Raman spectroscopy through the comparison between experimental data and molecular dynamics simulations [28]. Apart from the nice applications of low frequency Raman spectroscopy, the usual spectral range between 400-3800 cm^{-1} can be exploited to monitor the variation of the chemical environment around the oscillators. Cammarata et al. [29] used IR spectroscopy to correlate the blue-shift of the asymmetric stretching band of water with the relative strength of the interaction of H-bonding between water molecules and different anions species. Moreover, such H-bond strength has been correlated to the degree of hydrophobicity [30] and the polarity [31] of ILs. In another paper, Andanson et al. [32] used IR spectroscopy for understanding, at a nanoscopic scale, the mixing behaviour of ILs. The work demonstrated that vibrational techniques are suitable for the detection and quantification of the coexistence of different species of water clusters into domains of ILs. The local organization of water molecules in IL-water solutions has been investigated by using both Raman and IR spectroscopies [33, 34]. The conformational stability of imidazolium-based ILs in the presence of water has been discussed by Hatano et al. [35] by exploiting the information extracted from the Raman spectra of these solutions. Finally, Raman and IR spectroscopies were successfully employed for investigating the effect of water on the local structure and the phase behavior of protic ILs [36], giving evidence of the strong complementarity of the two techniques in describing different water-IL interactions. Herein, we provide the experimental evidence of the potentiality of synchrotron based-UV Resonance Raman (SR-UVRR) technique to probe the structural organization and the intermolecular interactions in imidazolium-based ILs as pure liquids and in water solution. UVRR spectroscopy exhibits several advantages with respect to conventional spontaneous Raman technique for the study of imidazolium-based IL/water solutions: i) a significant increment of the detection limit that allows to investigate the vibrational modes of ILs also in very high diluted conditions and ii) a selective strong enhancement in the UVRR spectra of ILs of the Raman cross section of the vibrations involving the imidazolium ring. This

latter condition occurs in particular when the excitation wavelength of UVRR spectra approaches the π-π^* transitions in the deep UV range [37–40]. In this sense, the availability of a tunable UV synchrotron radiation (SR) source allows to finely choose the resonance energy of excitation wavelength in order to maximize the intensity of the Raman peaks associated to the cations of ILs. These signals are sensitive spectroscopic markers of local rearrangements occurring in ILs and of the interactions between molecular domains of ILs and water molecules.

3.2.1 Experimental methods

Sample prepatation

1-methylimidazolium hydrogen sulfate ([MIM]HSO_4) was purchased from Sigma Aldrich with a purity of 95%. 1-methylimidazolium chloride ([MIM]Cl), 1-ethyl-3-methylimidazolium chloride ([EMIM]Cl), 1-decyl-3-methylimidazolium chloride ([C_{10}MIM]Cl), 1-dodecyl-3-methylimidazolium chloride ([C_{12}MIM]Cl) and 1-butyl-3-methylimidazolium hydrogen sulfate ([BMIM]HSO_4) were purchased from IoLiTec with a purity of 99%. All the ILs were dried under vacuum (10^{-3} bar) with phosphorus pentoxide for 72h in order to remove any possible water contamination before their use. Such procedure has been used for all ILs measured and reported in this thesis. High-purity water, deionized through a MilliQ^{TM} water system (>18 MΩ cm resistivity), was used for all the experiments. IL/H_2O solutions were prepared in a dry glove box at different molar fraction of IL, $x = n_{IL}/(n_{IL} + n_{H_2O})$, where n_{IL} and n_{H_2O} represent the mole number of IL and water, respectively. The molecular structures of ILs used in this study are reported in Fig.3.2 together with the atom labeling.

Raman spectroscopy measurements

UVRR spectroscopy experiments were carried out by using the setup descripted in Chapter 2. The exciting wavelengths used for collecting Raman spectra were fixed at 235 and 250 nm. The spectral resolution was set to about 6 cm^{-1} in order to have a satisfactorily high signal to noise ratio. The calibration of the spectrometer was standardized using cyclohexane (spectro-

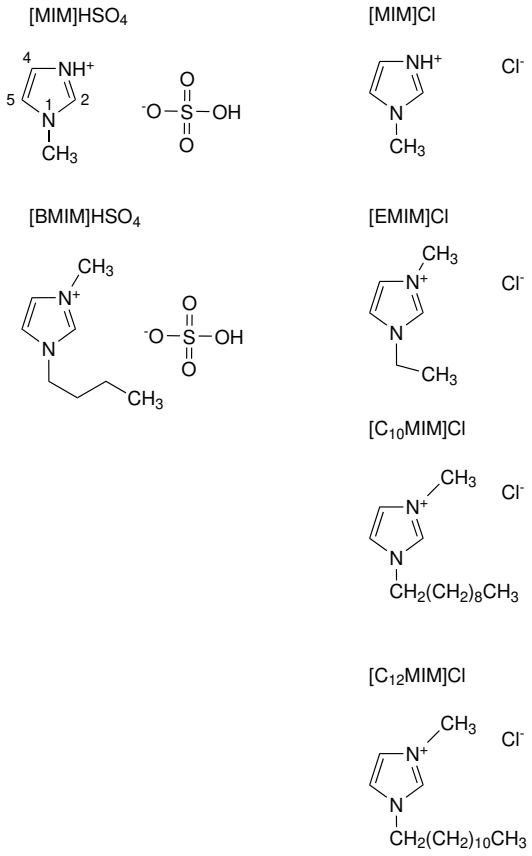

Figure 3.2: Chemical structure of ILs investigated in this work.

scopic grade, Sigma Aldrich). The power of the beam on the sample was kept sufficiently low (a few μW) in order to avoid photo-damage effects and heating of the sample.

Spontaneous Raman spectra were recorded at 785 nm laser excitation wavelength with a spectral resolution of 3 cm^{-1}. Raman spectra were collected using the spectrometer MonoVista CRS+ from the company S&I (Acton spectrometer SP2750 with Princeton Instruments PyLoN CCD camera) operating in a backscattering geometry. All UVRR and spontaneous Raman spectroscopy measurements have been collected at room temperature (298 K).

3.2.2 Results and discussion

The UV-Vis absorption spectrum of [MIM]HSO_4 in water is presented in Fig.3.3. The curve displays a strong absorption band at about 235 nm and a shoulder at 250 nm going to zero from ∼300 nm onwards. Based on the absorption features, Raman spectra of neat [MIM]HSO_4 have been collected with excitation wavelenghts at 785, 250 and 235 nm in order to approach spontaneous, pre-resonance and resonance conditions, respectively. Attention has been focused on the spectral range 1000 to 1600 cm^{-1}, although this frequency window is not extensively investigated in literature. The comparison between UV and visible Raman profiles points out the increasing Raman cross section of the vibrational modes between 1250 and 1600 cm^{-1} at low excitation wavelengths. These bands have been assigned to vibrations involving the imidazolium ring [37–40] in the molecular structure of [MIM]HSO_4 (Fig.3.3(a) and (b)). The enhancement of these peaks in the UVRR spectra was expected due to the π-π^* transition of imidazole ring electrons occurring below 300 nm. Conversely, the Raman peak at 1030 cm^{-1} is associated to the HSO_4^- symmetric stretching mode of the anion [41] and it appears particularly prominent in spontaneous Raman scattering (Fig.3.3(a)). These experimental findings suggest that UVRR spectroscopy allows us to probe also slight modifications occurring in the spectral parameters of the Raman vibrations associated to the cations in imidazolium-based ILs, due to the signal enhancement observed in the spectra excited with UV light compared to those obtained with the visible radiation. The comparison between UVRR spectra of [MIM]HSO_4 excited at 235 and 250 nm (Fig.3.3(a) and (b), respectively) shows similar experimental profiles, although the spectrum in Fig.3.3(a) has been collected with a worst resolution with respect to the corresponding one excited at 250 nm. This is due to the self-absorption phenomenon [42, 43] that is particularly strong in correspondence of the absorption maximum of the sample at 235 nm. In this condition, although Resonance Raman cross sections are generally larger than those of the pre-resonance Raman one, the intensity of the Raman signal is dramatically reduced, leading to a significant decrement of the signal-to-noise ratio. The continuous tunability of the SR source in the UV range offers the unique opportunity to finely approach such pre-resonance condition that

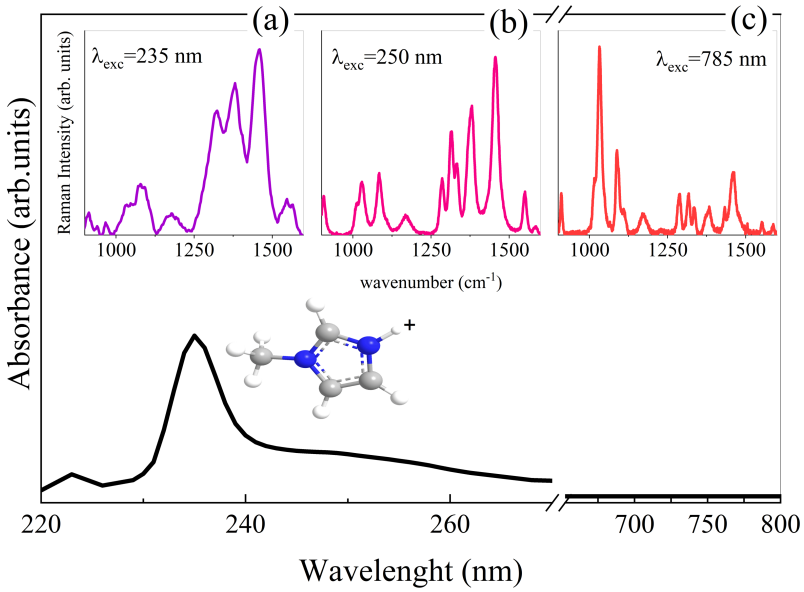

Figure 3.3: UV-VIS Absorption spectrum of [MIM]HSO_4 in water and Raman spectra collected on pure IL at 235 (a), 250 (b) and 785 nm (c) of excitation wavelength in the spectral range 900-1600 cm^{-1}.

ensure a satisfactory enhancement of the Raman modes associated with the imidazolium ring. However, at the same time it hampers the self-absorption, as observed in the UVRR spectra excited at 250 nm.

The selected frequency region wasn't typically investigated in literature for the proposed IL. In order to support the vibrational spectroscopy experiments, the structure of some ILs have been characterized by performing x-ray diffraction measurement at the XRD1 beamline@Elettra-Sincrotrone. The chosen ILs, indeed, appear in crystalline form at room temperature and such characteristic allows to resolve their structure. In particular, our attention was focused on the case of [MIM]Cl in order to minimize the presence of hydrogen atom in the anion counterpart, not well detectable by x-ray diffraction. The IL x-ray structure has been used for quantum chemical computation permitting to calculate the theoretical Raman intensity of the proposed IL with the use of *Crystal 17* software [44, 45]. Fig.3.4 shows a comparison between theoretical and experimental Raman signals for pristine [MIM]Cl. A good accordance between the reported Raman spectra has led to a correct assignment of the

experimental Raman vibrational features, that are reported in Tab.3.1.

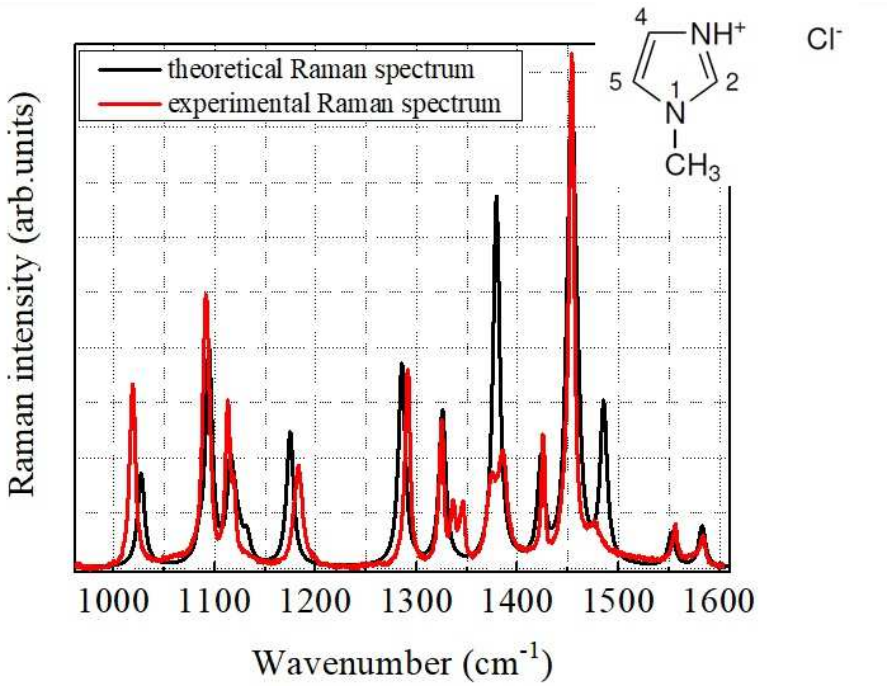

Figure 3.4: Comparison between theoretical (black) and experimental (red) Raman spectra collected at 785 nm for [MIM]Cl.

Fig.3.5 reports the comparison between UVRR and IR spectra of neat [MIM]HSO_4 and [MIM]Cl in the spectral region between 1080 and 1600 cm^{-1}, where only the vibrational modes associated to the imidazolium ring can be recognized. The spectra have been collected at room temperature where both ILs are in their crystalline phase. The IR profiles of both [MIM]-based ILs appear to be very similar to each other except for small differences observed for the relative intensities of some IR bands, as highlighted in Fig.3.5 by the arrows in the bottom right panel. Conversely, substitution of the anion species in the IL strongly affects the Raman spectra between 1080 and 1600cm^{-1} (see Fig.3.5, left panel). In the case of [MIM]Cl with respect to [MIM]HSO_4, we observe in the Raman spectrum the increment of a Raman peak at 1111 cm^{-1} (combination of bending modes involving C(4)H and C(5)H groups on imidazole ring) and the raising of an additional feature at 1345 cm^{-1}, probably related to changes in the molecular organization or in the strength of the in-

$x_{exp}(cm^{-1})$	x_{theor} (cm^{-1})	Assigned vibrational modes
1019	1027	δ(C2-N1-C5) + δ(H-N3-C4) + δ(H-C4-N3)
1091	1094	δ(C2-H) + δ(C5-H) + $\delta(CH_3)$ +ν(N3-C4)
1113	1116	δ(C4-H) δ(C5-H)
1183	1175	δ(C2-H) δ(N3-H)
1291	1285	δ(C4-H) + ν(N1-C + N1-C5 + N3-C4)+ + δ(C5-H) + δ(C2-H) + $\delta(CH_3)$
1345	1325	ν_a(N1-C5) + ν_a(N1-C1) + ν(N3-C2) + + δ(C2-H) + δ(N3-H) δ(C4-H) + δ(C5-H)
1374	1379	ν_s(C4-C5) + ν_s(C2-N1) + $\delta(CH_3)$ + δ(C2-H) + δ(C5-H)
1425	1423	$\delta(CH_3)$
1453	1453	ν_s(C4-C5 + C2-N3) + ν(N3-C4) + δ(N3-H) + $\delta(CH_3)$
1476	1485	$\delta(CH_3)$
1556	1552	ν_a(C2-N1) + ν_a(C2-N3) + δ(C2-H) + δ(C3-H)
1583	1583	ν_a(C4-C5) + ν_a(C2-N1) + δ(N3-H)

Table 3.1: Experimental and calculated Raman frequencies and assigned Raman vibrational modes for [MIM]Cl.

teractions involving the imidazolium ring due to the different anion type. The Raman peak centred at 1454 cm^{-1} in the spectrum of [MIM]Cl, assigned to the antisymmetric bending mode of the N-methyl group in accordance with literature [46, 47], appears blue-shifted by about 5 cm^{-1} and significantly broader in the experimental profile of [MIM]HSO_4. Similarly, also the peaks at 1180 and 1291 cm^{-1} in the spectrum of [MIM]Cl, associated to bending motions of the CH and NH groups located on the imidazole ring, are found red-shifted by about 5 cm^{-1} and broader in the spectrum of [MIM]HSO_4. This probably reflects the change in the interaction strength between the anion (Cl^- or HSO_4^-) and the cation in the two different ILs. Finally, also the Raman peaks at 1556 and 1580 cm^{-1} that are associated mainly to vibrations involving the imidazolium ring and the bending modes of the NH groups undergo slight frequency shifts and intensity variation, as can be observed by comparing the UVRR spectrum of [MIM]Cl to the corresponding one of [MIM]HSO_4. All these findings suggest that UVRR spectra are rich of vibrational signatures of the interactions established between cation and anion that drive the molecular

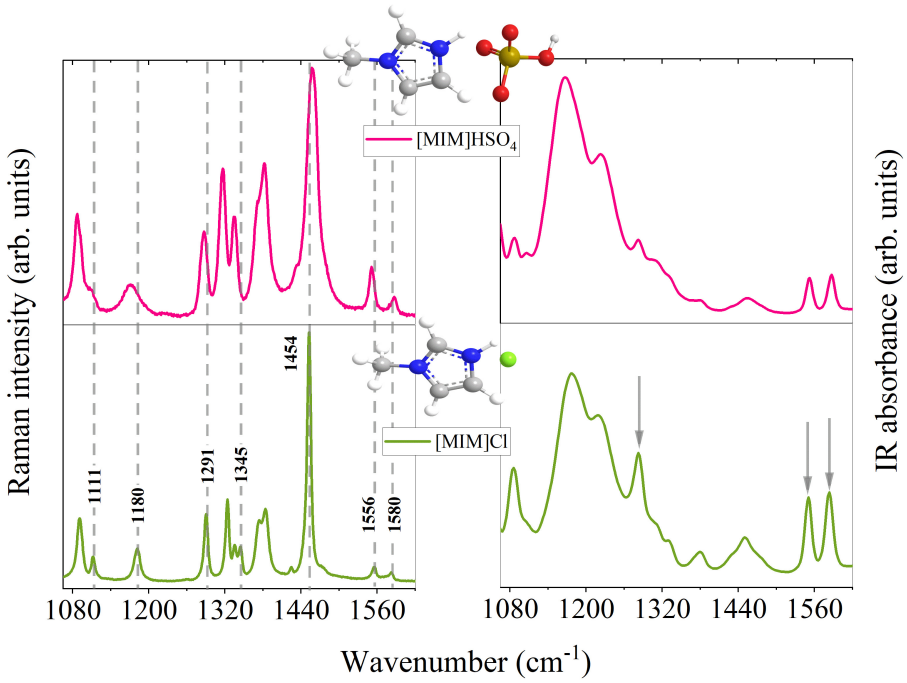

Figure 3.5: Comparison between UVRR spectra excited at 250 nm (panel on the left) and IR absorption spectra (panel on the right) of neat [MIM]HSO_4 and neat [MIM]Cl.

organization of IL domains. A further support to this hypothesis can be found by inspection of Fig.3.6. The figure shows UVRR spectra collected on a set of imidazolium-based ILs with N-alkyl chains of different length in the spectral region mainly dominated by the imidazolium ring vibrations. Significant modifications of the spectral profiles associated to the imidazolium vibrational modes seem to be induced by the replacement of the hydrogen atom attached to the imidazolium N with an alkyl chain (compare the UVRR spectrum of [MIM]HSO_4 to that of [BMIM]HSO_4 in Fig.3.6(a)). The UVRR spectrum of [BMIM]HSO_4 is characterized by three strong bands at about 1335, 1386 and 1415 cm^{-1}, assigned to combined vibrational modes mainly involving the imidazolium ring and the CH and NH groups located on the ring [48]. In the same spectral region, the experimental profile of [MIM]HSO_4 appears quite different from that of its analogue [BMIM], confirming that the UVRR modes of imidazolium are strongly sensitive to the chemical structure of the substituent on the ring.

Fig.3.6(b) further supports this outcome, giving evidence that the Raman

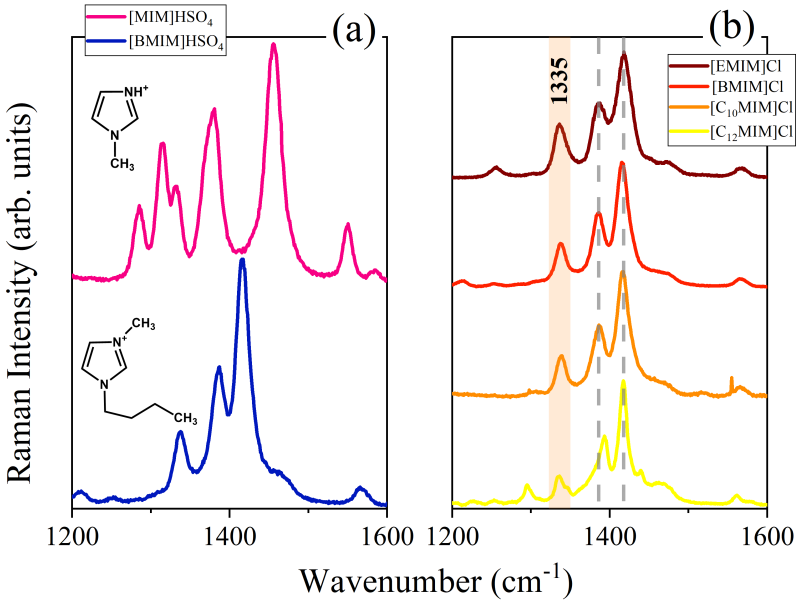

Figure 3.6: Comparison between the UVRR spectra (excited at 250 nm) of (a) $[MIM]HSO_4$ and $[BMIM]HSO_4$ and of (b) [EMIM]Cl, [BMIM]Cl, $[C_{10}MIM]Cl$ and $[C_{12}MIM]Cl$.

peaks mentioned above can be specifically associated to the change of substituents on the imidazolium ring in this type of ILs. Although the mode at 1415 cm^{-1} does not exhibit any significant modification in frequency position or intensity when the alkyl-chain is extended from [EMIM] to $[C_{12}MIM]$, conversely, the peak at 1386 cm^{-1} undergoes a blue-shift of about 5 cm^{-1}. At the same time, a progressive reduction of the intensity of the Raman peak at 1335 cm^{-1} can be observed as the length of the alkyl chain on the ring increases. Since this mode corresponds to a combination of ring breathing and stretching motions of N(1)-CH_2 and N(3)-CH_2 for [EMIM]-based ILs [49], we can propose that the increasing length of the alkyl chain on the imidazolium ring is reflected in a progressive hindering of the stretching vibrations involving N(1)-CH_2, as shown by the decreasing intensity in Fig.3.6(b). This suggests that the Raman peak at 1335 cm^{-1} in the UVRR spectra of imidazolium-based ILs could be used as a sensitive spectroscopic marker of the molecular reorganization of cationic domains induced by the progressive elongation of the alkyl substituents at the imidazolium ring.

Finally, Fig.3.7 points out the greater sensitivity of UVRR technique with

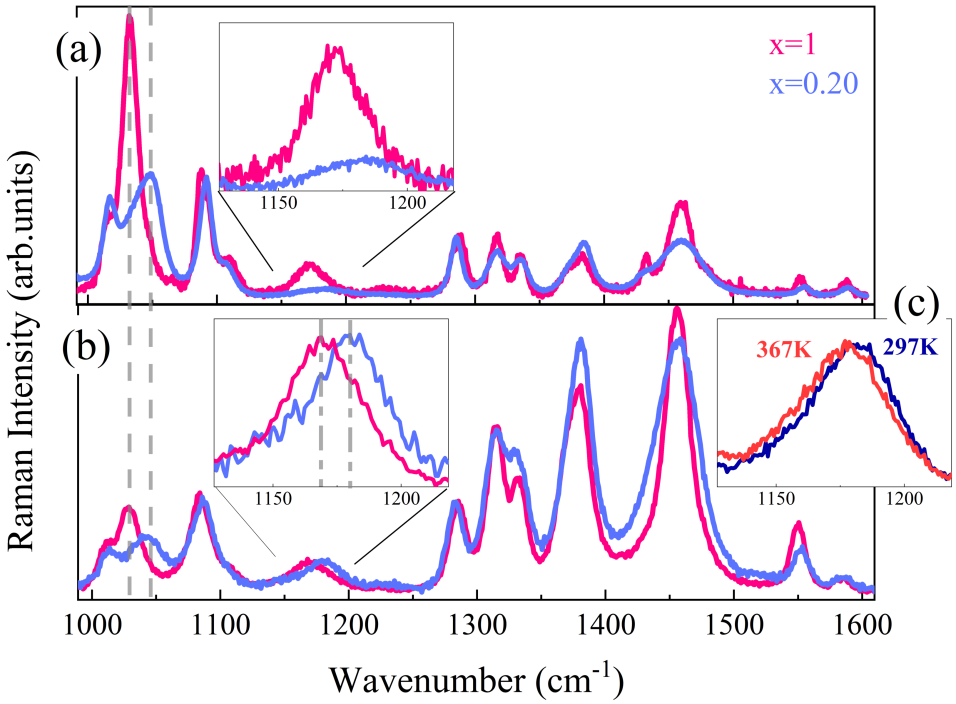

Figure 3.7: Comparison between the Raman spectra of pure (pink) and hydrated (blue) [MIM]HSO_4 collected at an excitation wavelength of a) 785 nm and b) 250 nm. c) UVRR spectra of hydrated MIM]HSO_4 (x=0.30) recorded at two different temperatures, i.e. 297 and 367 K collected at 250 nm.

respect to conventional spontaneous Raman scattering in probing the effect of water on the strength of H-bonds involving cation domains in imidazolium-based ILs. Fig.3.7 shows the comparison between the Raman spectra of pure and water-added [MIM]HSO_4 collected at an excitation wavelength of 785 nm (panel a) and 250 nm (panel b). We remark that the analysis of the spectral range considered in Fig.3.7 is usually very difficult to be analyzed by using IR spectroscopy, due to the strong signal of water dominating the spectra in this region also at low water content [36,50]. Raman spectroscopy offers the advantage to explore also the spectral region between 1000 and 1600 cm^{-1} by looking at the modifications occurring to the Raman signals arising exclusively from ILs also in very high-diluted conditions. Both the UVRR and spontaneous Raman profiles of Fig.3.7 point out that also at this relative low-dilution condition (IL/water molar fraction = 0.2) the Raman peak centred at 1032 cm^{-1} in the neat IL, assigned to the stretching vibration of the anion HSO_4, shifts toward higher wavenumbers when the water is added to the system. This ef-

fect can be explained by considering the solvation effect of water on the anions competing with the electrostatic interactions between cation and anions in the hydrated ILs. As concerning the Raman vibrational modes associated only to the molecular motions involving the imidazolium ring, the vibrational spectra appear quite sensitive to the addition of water, especially for the UVRR profiles (Fig.3.7(b)). This is reflected mainly by the slight shift in frequency position, changes in intensity and broadening of some Raman modes observed in the spectrum of [MIM]HSO_4 as a consequence of hydration. Remarkably, the UVRR spectra of hydrated [MIM]HSO_4 evidence a significant blue-shift of about 10 cm^{-1} of the Raman peak centred in the neat IL at about 1170 cm^{-1} (inset of Fig.3.7(b)). This effect is not so clearly detected in the spontaneous Raman spectra of [MIM]HSO_4 (Fig.3.7(a), inset), probably due to a stronger reduction of the Raman cross section of the modes arising from IL when it is dissolved in water . The main vibrational contribution to the Raman mode at 1170 cm^{-1} has been assigned to a combination of bending modes of the C(2)-H and N(3)-H groups on the imidazolium ring of [MIM]HSO_4 (see Tab.3.1). On the other hand, these two sites have been demonstrated to be responsible of the formation of H-bonds between the cation and anion [52] in the IL. This interpretation is supported by the experimental evidence that the same Raman peak moves to lower frequencies upon the increasing of thermal motion (Fig.3.7(c)) that usually leads to a weakening of the H-bonds interactions. The experimental findings described in Fig.3.7(b) suggest that for high dilution of [MIM]HSO_4 in water a complete exchange of water molecules with anions in the formation of hydrogen bonds with cations can be expected and that the strength of this cation-water interaction is probably stronger than the cation-anion one.

3.3 Water nano-domains in AILs: imidazolium versus pyridinium precursors

Previous studies have demonstrated that AILs can organize in nano-sized domains characterized by a polar domain consisting of the imidazolium ring and the anion and a non-polar domain composed of the alkyl chains. The

resulting stucture can be pictured as an inhomogeneous nano-domain arrangement [53–56]. The nano-domain structure of pure IL has been observed to be maintained even in mixed solutions in which the water molecules are found to be situated near the boundaries between the polar and nonpolar domains leading to the formation of nano-confined water structures [57]. For low concentrations of water, the structure of ILs is only slightly disrupted leading to and adjustment in the relative positions and orientations of cations and anions. However, the formation of this water-rich nano-domains has a dramatic impact in the physico-chemical properties of both IL and of nano-confined water [58]. Aqueous solutions of [BMIM][BF_4] have been widealy investigated in literature by using Small Angles Neutron Scattering (SANS) technique with the aim to elucidating the nano-scale structure of these mixtures [59, 60]. The work of Almasy et al. [60] showed that specific features appear in the SANS profile of the IL/water solutions at a concentration of about $x_{IL} = 0.75$. This experimental finding has been interpreted as a signature of the heterogeneous mixing in this system. Such kind of heterogenity in IL/water binary mixtures has been observed also in organic solvents/water systems [61–66]. In addition, it has been noted that parameters such as the alkyl chain lenght of the cation and the cation-anion interactions tend to influence the nano-structure of IL/water mixtures and their hydrophobic/hydrophilic properties. For instance, it has been found that ILs with alkyl chain length $n \geq 6$ exhibit a characteristic self-organization behaviour that leads to the formation of micelle in aqueous solutons [67–69]. This is probably due to the fact that cations with relatively long alkyl chain, as the C_nMIM cations with $n \geq C_6$, act as cationic surfactants. A recent study [70] reported on the dependance of the alkyl-chain length n of the the $[C_n MIM]^+$ cation and the halide anion species (Cl^-, Br^- and I^-) on their aggregation behavior in aqueous solutions. It has to be noteworthy that the water confined in the nano-domains formed by IL/water mixtures exhibits a peculiar behaviour, very different from that of bulk or hydration water. Although in literature it is present a wide study on the so called water pockets in imidazolium-based ILs, any evidence has not yet been found of formation of these peculiar nano-domains in ILs with pyridinium as precursor. Here we report on the investigation of the nano-water domains in a series of ILs with imidazolium- and pyridinium-based cation with the aim to

correlate the different behaviour exhbited by these systems as a function of the nature of their cation. SANS measurements give information on the structural organization of the water pokets and on the characteristic correlation lenghts of these nano-domains. At the same time, UVRR technique can provide insights on the hydrogen-bond interactions between the water molecules confined in the spaces of nano-domains trough the analysis of the high-wavenumber range of vibrational spectra.

3.3.1 Experimental methods

Sample preparation

1-butyl-3-methylimidazolium tetrafluoroborate ([BMIM]BF_4), 1-butyl-3-methylimidazolium triflate ([BMIM]TfO), 1-butylpyridinium tetrafluoroborate ([BPy]BF_4) and 1-butylpyridinium triflate ([BPy]TfO) were purchased from IoLiTec with a purity of 99%. High-purity water, deionized through a MilliQ^{TM} water system (>18 M cm resistivity), was used for Raman spectroscopy experiments. At the contrary, heavy water with 99.3% of deuterium content was used as solvent for SANS experiments in order to increase the isotopic contrast in the scattering length densities between IL and water, thus improving the precision of the experiment.

SANS measurements

SANS experiments were carried out using the *Yellow Submarine* diffractometer operating at the Budapest Neutron Center [71]. Samples were placed in 1 mm-thick quartz cells. Temperature was controlled within 0.1 K using a Julabo FP50 water circulation thermostate.The range of scattering vectors q was set to 0.038-0.38 $\mathring{A}^{-1}$. The q value is defined as $q = 4\pi/\lambda \sin\theta$ where 2θ is the scattering angle. In order to have access to the whole range of q, we used two different configurations. In particular, the sample-detector distance was set to 5.125m and the incident neutron wavelengths were $\sim 4.4\mathring{A}$ and $\sim 10.23\mathring{A}$ for medium and low q range, respectively. The raw data have been corrected for sample transmission, scattering from empty cell, and room background. Correction to the detector efficiency and conversion of the measured

scattering to absolute scale was performed by normalizing the spectra to the scattering from a light water sample. A basic description of SANS theory is reported in Appendix A.

Raman spectroscopy measurements

UVRR experiments were carried out by using the setup descripted in detail in Chapter 2. The exciting wavelength used for collecting Raman spectra was set at 248 nm. The spectral resolution was set to about 10 cm^{-1} in order to have a satisfactorily high signal to noise ratio. The calibration of the spectrometer was standardized using cyclohexane (spectroscopic grade, Sigma Aldrich). The power of the beam on the sample was kept sufficiently low (a few μW) in order to avoid photo-damage effects and heating of the sample.

3.3.2 Results and discussion

SANS profiles of [BPy]TfO_4/D_2O and [BPy]BF_4/D_2O solutions in the x_{IL} range from 0.02÷ 0.12 and collected at 298 K are shown, as an example, in Fig.3.8. The scattering curves were analyzed by using the Ornstein-Zernike form for statistical concentration fluctuations given by the equation:

$$I(q) = \frac{I_0}{1 + q^2\xi^2} + Bg \tag{3.2}$$

where Iθ represents the coherent forward scattering intensity, ξ is the short-range correlation length, which is the measure of the decay of density-density correlations and Bg is the constant background term. This last term accounts for the contribution of the incoherent scattering from the hydrogen and deuterium atoms in the mixture and it can be expressed as:

$$Bg = a \cdot v_f + b(1 - v_f) \tag{3.3}$$

where a and b are two constant parameters and v_f represents the IL volume fraction taking into account the number of hydrogen and deuterium atoms. The Bg contribution is constant as function of temperature because v_f remain invariable at a fixed molar fraction. The measurements were collected as function of in order to execute a global fit with Bg as a common parameter. This

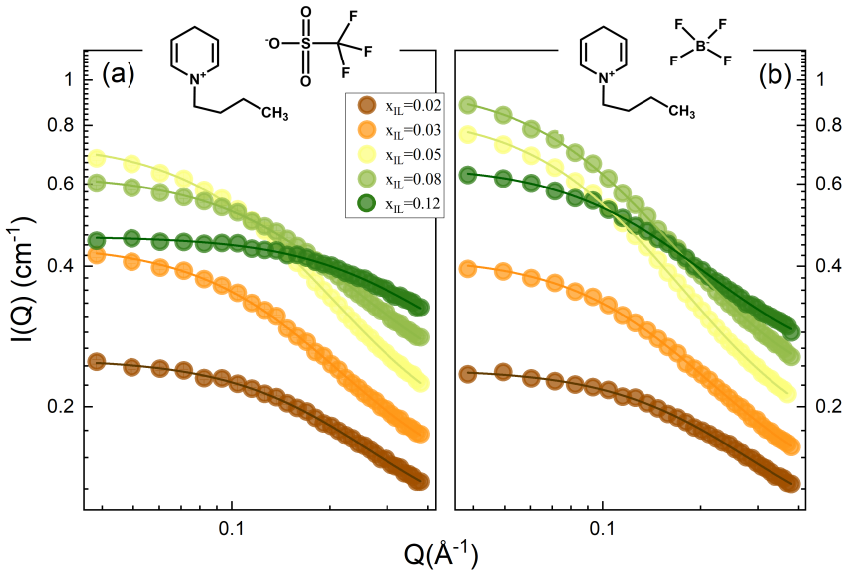

Figure 3.8: Comparison among SANS curves of [BPy]TfO/D_2O (a) and [BPy]BF_4/D_2O (b) solutions as function of IL molar fraction and at 298 K. The continuous lines are fitting of the experimental data obtained by using Eq.3.2.

procedure allowed us to reduce the total number of free parameters in Eq.3.2 during the fitting of experimental data. Fig.3.8 clearly points out that the experimental data are well reproduced by the Ornstein-Zernike function for all the examined concentrations. This result suggests that the distribution of the molecular species in the system is similar to the case of strong concentration fluctuations.

Fig.3.9 shows the Ornstein-Zernike correlation lengths estimated for the four selected ILs as function of x_{IL}. In all of the cases, the curves show a maximum at a characteristic IL molar fraction. In particular, the trend observed for [BMIM]BF_4-D_2O mixtures is consistent with that reported by Almàsy et al. [60] in previous SANS experiments. As seen in this figure, the correlation length for [BMIM]BF_4-D_2O mixtures increases with increasing x_{IL} from 0.2 to 0.6, then decrease with the further increase in x_{IL}, resulting in a maximum between x_{IL}=0.6 and 0.8. Such result confirms that [BMIM]BF_4 and water molecules show the maximum inhomogeneity at x_{IL} ≈0.07 in the investigated molar fraction range. This finding is an important validation for the whole

data set, as it reproduces quantitatively the inhomogeneity trend previously reported [60]. Interestingly, Fig.3.9 shows that a similar molar fraction dependence can be observed for the case of [BPy]BF_4-D_2O solutions, again with a maximum ξ value at around x_{IL}=0.07. It is interesting to compare the Ornstein-Zernike correlation lenghts of [BPy]BF_4-D_2O and [BMIM]BF_4-D_2O mixture at the same x_{IL}=0.07. The maximum ξ value for the former mixture is $\sim 4\mathring{A}$ smaller smaller than the corresponding for [BMIM]BF_4-D_2O mixtures. At this stage, it is tempting to postulate that the common anion is dictating the trend in density fluctuations, leading to the value of x_{IL}=0.07 as a descriptor of the maximum inhomogeneity. Conversely, the chemical structure of the cation seems to affect the value of the correlation length. The behavior observed for the other two systems, [BPy]TfO-D_2O and [BMIM]TfO-D_2O mixtures, is indeed consistent with such an assumption. The curves related to the systems sharing the TfO^- anion and shown in Fig.3.9 point out that both mixtures have the maximum inhomogeneity at the sam value of IL molar fraction x_{IL} $\approx$0.05. In turn, the maximum correlation lengths for the two systems are $7\mathring{A}$ and $9\mathring{A}$ respectively, thus showing the decrease of ξ observed before, although attenuated ($4\mathring{A}$ vs $2\mathring{A}$ difference on passing from the BF_4^- to the TfO^- solutions). These results suggest a scenario where the inhomogeneous distribution of IL and water molecules is maily driven by by the nature of the anion species. The strongest effect is associated to the small, conformationally rigid, symmetric and charge localized BF_4^- ion, while the larger, more flexible, polarizable and charge delocalized TfO^- induces a smaller effect. From this standpoint, the x_{IL}(maximum) from SANS experiment is a direct fingerprint of the solvation features of the anion. The correlation lengths are more related to the cation structure, and probably affected by a complex balance of hydrophilic/hydrophobic contributions of the alkylpyridinium vs alkylimidazolium ions. This interpretation seems to be consistent with the temperature response of the four examined systems as shown in Fig.3.10. The curves compare the Ornstein-Zernike correlation lengths estimated at two different temperatures for the four selected ILs as function of x_{IL}. In all of the cases, the values of xIL(maximum) are temperature independent, thus confirming this parameter as a descriptor of the solvation features. For all systems, the ξ magnitudes gradually decrease with increasing temperature decreases, thus

suggesting that ξ can be correlated to the extension of the solvation shell of the IL.

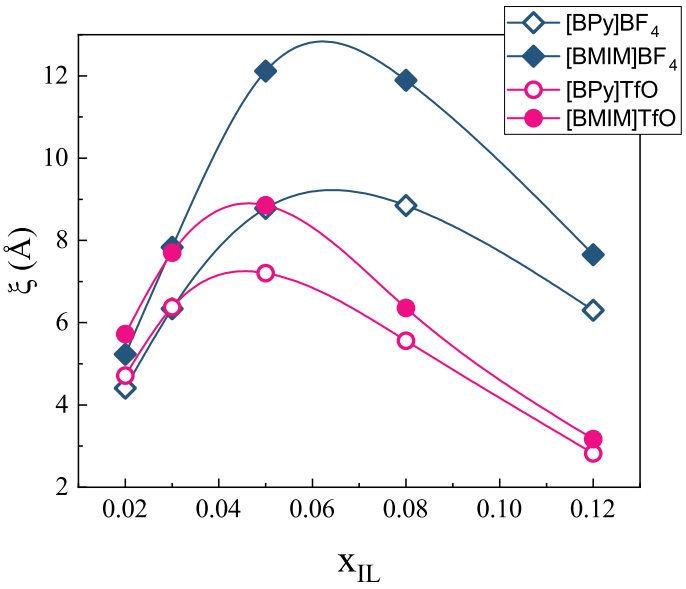

Figure 3.9: Correlation lengths ξ extracted for [BPy]BF_4 (open blue rhombs), [BMIM]BF_4 (full blue rhombs), [BPy]TfO (open pink circles and [BMIM]TfO (full pink circles) water mixtures as function of molar fraction at 298 K. The solid lines are guides for eyes.

Fig.3.9 shows the Ornstein-Zernike correlation lengths estimated for the four selected ILs as function of x_{IL}. The trend obtained for [BMIM]BF_4/D_2O mixtures is consistent with that found in previous SANS experiments by Almàsy et al. [60]. As seen in this figure, the correlation length for [BMIM]BF_4-D_2O mixtures increases with increasing x_{IL} from 0.2 to 0.6 and decrease again with the further increase in x_{IL}, resulting in a maximum between x_{IL}=0.6 and 0.8. Such result suggests that [BMIM]BF_4 and water molecules are most heterogeneously mixed with each other in the mixtures at x_{IL} ≈0.07 in the investigated molar fraction range. Interestingly, a similar molar fraction dependence it is observed for the case of [BPy]BF_4-D_2O solutions with a maximum ξ value at around x_{IL}= 0.07. Moreover, the Ornestein-Zernike correlation lengths of [BPy]BF_4-D_2O mixture is ∼3 $\mathring{A}$ smaller than for the [BMIM]BF_4-D_2O ones in the region of its maximum. Looking at the behaviour exhibited by TfO^- cases shown in Fig.3.9, it is possible to observe a decrement of x_{IL} value corre-

spondence to the maximum ξ value both for the case of $[BMIM]^+$ and $[BPy]^+$ cations. These results suggest a scenario that the molar fraction range with the strongest inhomogeneities (or: inhomogeneous distribution of IL and water molecules) is influenced rather by the nature of the anion species and not by the cation ones. Moreover, both for the case of BF_4^- and TfO^- anions, a smaller correlation length is obtained for $[BPy]^+$ with respect to $[BMIM]^+$. The latter result gives evidence that the system composed by imidazolium-based IL exhibits a stronger inhomogeneity when mixed with water molecules.

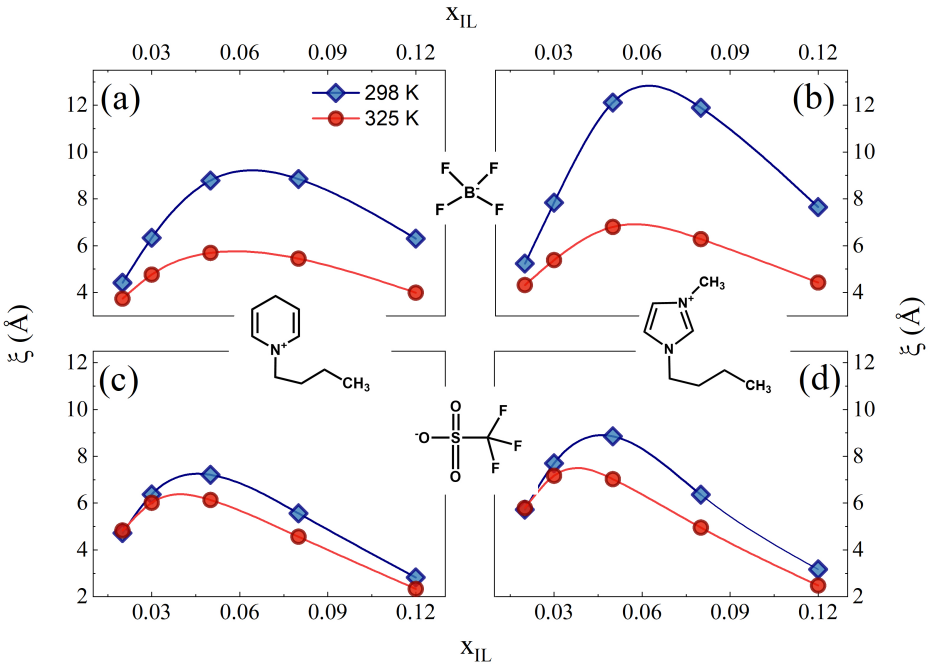

Figure 3.10: Comparison between the correlation lengths ξ collected at 298 and 325 K for a) $[BPy]BF_4$, b) $[BMIM]BF_4$, c) [BPy]TfO and d) [BMIM]TfO - water mixtures as function of molar fraction. The solid lines are guide for eyes.

Fig.3.10 compares the Ornstein-Zernike correlation lengths estimated at two different temperatures for the four selected ILs as function of x_{IL}. For all systems, the ξ magnitudes gradually increase when the temperature decreases. This result reflects that the heterogeneity of IL-D_2O mixture is gradually enhanced with decreasing temperature. As first remark, it is possible to notice that this behaviour is more evident for the case of BF_4 (see Fig.3.10 (a)-(b)),

while the ILs composed by TfO show a slight temperature dependence (see Fig.3.10 (c)-(d)). By the inspection fo Fig.3.10, it is possible to notice that at the concentration in correspond to the maximum inhomogeneity, the correlation length is strongly affected by the temperature. It is thus shown that the heterogeneity of the IL–D_2O is most drastically evolved in the mole fraction range investigated when the temperature decreases at x_{IL} 0.07 and 0.05 for BF_4^- and TfO^--based ILs, respectively. A second aspect, Fig.3.10 points out that the molar fraction value where we observe the maximum ξ value is independent by the temperature for all selected ILs.

For the case of imidazolium-based ILs, the description of water behaviour has been enriched by UVRR scattering with the aim to define its local rearrangement from a molecular point of view. In fact, UVRR spectroscopy represents a valid method able to probe the molecular state of water in the presence of co-solvent or solute [72–74]. In particular, the OH stretching mode is very sensitive to water environment and intermolecular interactions and the corresponding Raman signal can be used to gain specific information on the H-bonding state of water molecules in the pure liquid state or in aqueous mixtures of different chemical substances. In this work UVRR analysis has given the possibility to study the different molecular state of water in imidazolium-based ILs function anion species, revealing structural changes in the local H-bonding network of water. The same procedure was not performed for pyridium-based ILs, due to the great UV absorbance of cation species that does not permit to detect the Raman vibrational feature associated to water molecules. At the same time, the use of visible excitation wavelength for these selected ILs is hampered by the presence of a strong fluorescence signal.

Fig.3.11(a-b) shows the evolution of UVRR spectra in the case of [BMIM]BF_4 and [BMIM]TfO upon the addition of water in the mole fraction range of $0.2 < x_{IL} < 0.02$. The spectra of pure ILs and H_2O are reported in the graphs for the sake of comparison. The hydration water features can be better visualized by the difference spectra shown Fig.3.11(c-d) and calculated by subtracting the rescaled spectrum of neat water from the spectra of IL/water mixtures [75]. This procedure allows to isolate the spectral distribution associated to those water molecules which are structurally affected by the interaction with the IL, especially with the anion moieties. In fact, it is well known that the changes of

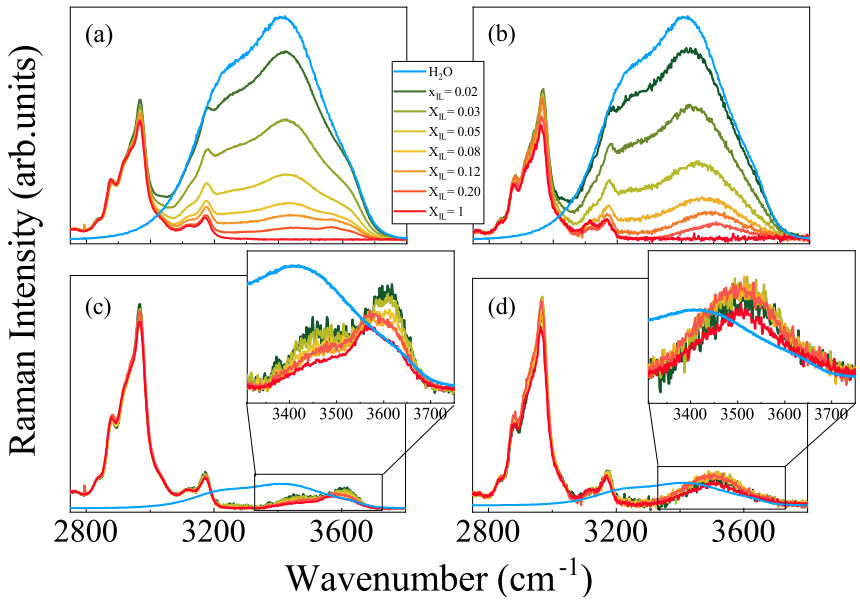

Figure 3.11: TOP: Concentration-evolution of UVRR spectra for a) [BMIM]BF_4 and b) [BMIM]TfO aqueous solution collected at 248 nm. BOTTOM: Difference spectra obtained by subtracting the spectrum of pure water from that of the c) [BMIM]BF_4 and d) [BMIM]TfO aqueous solutions.

the OH stretching band mainly depend on variations of the state of water acting as H-bond donor in the H-bond reorganization, which would be essentially related to the intervention of new O-H$\cdots$X interactions with the anion species. Conversely the cation-water H-bond interactions, which are expected to play a role in the investigated systems, do not affect OH stretching features. For both ILs, the difference spectra are localized at higher frequency with respect to the OH stretching band of pure water (see Inset of Fig.3.11(c-d)). Such blue shift points out the formation of weaker H-bond interactions between water and anion species than water-water ones.

In Fig.3.12 it is possible to observe the difference spectrum obtained for the [BMIM]BF_4 solutions at at x_{IL}=0.20. Such Raman profile is composed by three components centered at $\sim$ 3475, 3565 and 3625 cm^{-1} and labeled as band I, band II and band III, respectively. The last two features are sometimes called *nearly-free hydrogen bands* (NFHB) [76, 77]. Band II and III can be associated, respectively, to the symmetric and antisymmetric stretching of

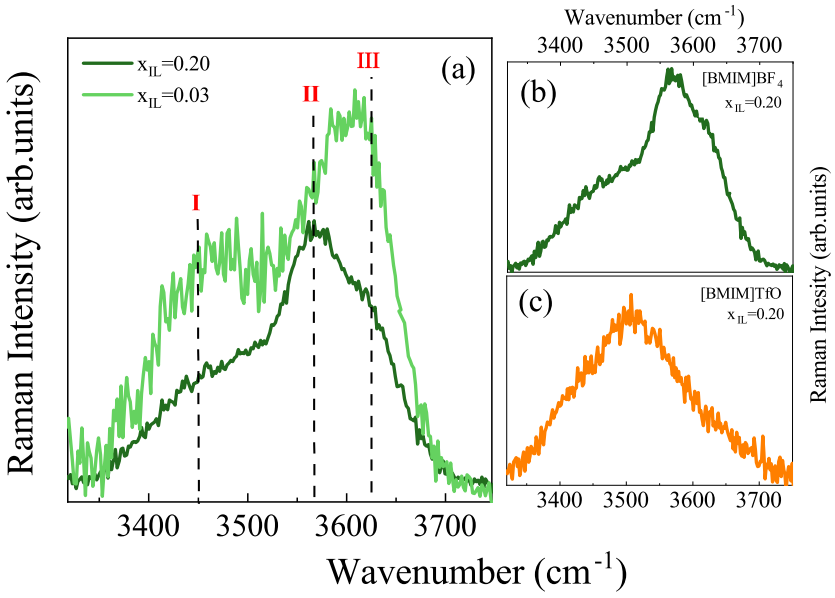

Figure 3.12: LEFT: Comparison between the difference spectra of $[BMIM]BF_4/H_2O$ mixture at x_{IL}=0.20 (dark green) and 0.03 (light green). RIGHT: Comparison between the difference spectra of b) $[BMIM]BF_4$ and c) [BMIM]TfO aqueous solutions at x_{IL}=0.20.

water molecules having both OH groups involved in the formation of weak H-bonding interactions with two different anions: $F^- \cdots$H-O-H$\cdots F^-$. A similar description was reported by Cammarata et al. [29], who investigated the OH stretching mode of $[BMIM]BF_4/H_2O$ mixtures at very low water concentration ($0.96 < x_{IL} < 0.81$) by ATR-FTIR spectroscopy. It is interesting to note that the presence of similar components is detected even when a large fraction of bulk water is present within the system (x_{IL}=0.20). Fig.3.12(a) compares the difference spectra of $[BMIM]BF_4/H_2O$ at 0.20 and 0.03 of molar fraction. It is possible to observe a clear change on the shape of the band upon water addition, with a relative enhancement of the high frequency component of the profile. Possibly this variation can be associate to the changes of hydration water properties related to the dissociation of IL aggregates with dilution. In fact the probability of formation of water adducts with two anions will reduce with the increase of water fraction. Thus, it is possible to suppose that with the increase of number of H_2O molecules in solution, water-water interaction will tend to substitute water-anion ones and at higher dilution hydrating water

will be bonded with only one OH group to an anion while the second OH group will be bonded to water (F^--$\cdots$H-O-H$\cdots$O). Likely the spectral contribution of the OH group singly bonded to the anion resonates at around 3620 cm^{-1}, close to the III component. The proposed picture can be correlated with inhomogeneity variations detected by SANS: $x_{IL} > 0.12$ extended IL aggregates exist that favor the formation of BF_4-$\cdots$H-O-H$\cdots BF_4$ adducts at the IL/water interface; for $x_{IL} < 0.12$ the reduction of IL aggregation occurs bringing to a decrease of spatial heterogeneity in the sample. Band I labeled in Fig.3.12(a) appears at low frequency with respect to the two components described above. This signal is indicative of stronger H-bond interaction formed by the corresponding OH oscillators in comparison to component II and III. This band is can be attributed to water-water H-bonds partially affected by the presence of the anions, which might cause the partial destructuring of the ordered network typical of bulk water. Fig.3.12(c-d) show a comparison between the difference Raman spectra of the two selected ILs at x_{IL}=0.20. While difference spectra of [BMIM]BF_4 are characterized by manifold components, the profiles for [BMIM]TfO appear composed by only one broad component. Such a band appears at lower frequency with respect to band II and band III, and can be tentatively attributed to the formation of water-TfO^- H-bonds stronger for when compared to the BF_4^- case, in agreement with results reported in literature [29]. There is not a significant evolution of difference Raman spectra in the case of [BMIM]TfO solutions as a function of water concentration (see Inset of Fig.3.12(d)). This suggests that the state of hydration water is not affected within the explored range. Such behaviour is in line with SANS results which indicate weaker inhomogeity extent in [BMIM]TfO aqueous solutions with respect to the case of [BMIM]BF_4. The former system appears less structured and the IL cluster formations are not extended. For this reason, the addition of water does not induce a strong structural reorganization.

Chapter 4

Stability of model peptides in ionic liquid/water solutions

4.1 Aqueous solvation of peptides probed by UVRR spectroscopy

In this section we will present some results aimed to show the potentiality of SR-based UVRR technique for investigating the solvation dynamics of peptides. These organic molecules, consisting of short chains of amino acids, are widely investigated for their biomedical relevance. When they are dissolved in aqueous solution, the characteristic structure, dynamics and functions of peptides are strongly affected by water due to the unique H-bonding capability of this solvent [78]. Considering that water plays a fundamental role in many biological process involving proteins [79–82], aqueous solutions of simple peptides are usually chosen as model systems to tackle the investigation of water-protein interactions at the atomic scale [83]. UVRR spectroscopy is a powerful tool for studying the conformational rearrangements occurring in peptides [84–88] and proteins [89, 90] and the role played by the water solvent in driving these structural changes. The higher sensitivity of UVRR technique respect to spontaneous Raman scattering is crucial for allowing to investigate peptides in very diluted conditions while maintaining a satisfactory quality of the spectra. Moreover, UVRR spectra excited at energy within the

amide π-$\pi^\star$ transition are dominated by the Raman modes arising from the backbone of peptides These amide vibrations are characterized by frequency position, intensity and bandwidth that depend sensitively on structural conformation of peptides [85, 91]. In an effort to provide insights on the solvation dynamics on simple model peptides, we chose to investigate the pair of dipeptides N-acetylglycine- methylamide (NAGMA) and N-acetyl-leucine-methylamide (NALMA). Fig.4.1 shows the chemical structure of these two molecules that are quite similar, except than for the hydrophobic leucine side chain bound to the hydrophilic backbone of NALMA. This confers it a more hydrophobic character with respect to the hydrophilic nature of NAGMA. The pair of these peptides has been especially studied by experimental and simulation techniques since NALMA and NAGMA have been demonstrated to mimic important characteristics of proteins [92–99]. However, few studies were performed in a very wide concentration regime of NALMA/NAGMA in aqueous solution [96, 97, 100–102], probably due to the need of using experimental techniques able to distinguish the contribution of peptides from that of solvent water also in very diluted conditions. Here we report an SR-based UVRR spectroscopic investigation on solutions of NAGMA and NALMA in a wide range of concentration ranging from very concentrated to diluted conditions and as a function of temperature. By opportunely choosing the excitation wavelength, the primary amide vibrations of peptides can be strongly enhanced in the UVRR spectra. These signals are used as sensitive spectroscopic markers of the hydrogen-bonding environment of backbone of NALMA and NAGMA at different experimental conditions [129].

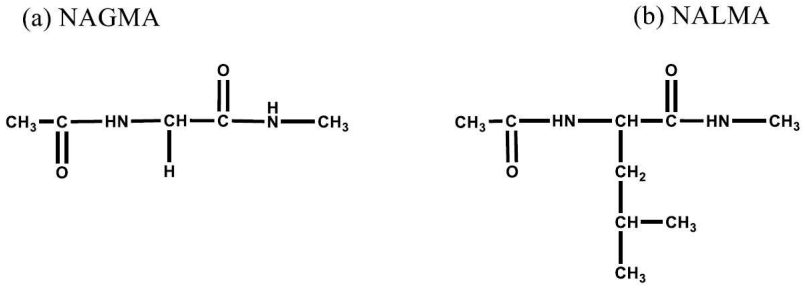

Figure 4.1: Chemical structure of the two dipeptides N-acetyl-glycine-methylamide (NAGMA) (a) and N-acetyl-leucinemethylamide (NALMA) (b)

4.1.1 Experimetal methods

Sample preparation

N-acetyl-leucine-methylamide (NALMA) and N-acetyl-glycine-methylamide (NAGMA) were purchased from Bachem and used without further purification. The aqueous solutions of peptides were prepared by dissolving NAGMA or NALMA in doubly distilled deionized water at different concentrations, ranging from about 300 to 2 mg/ml. At these values of concentration, the solutes are totally dissolved and the solutions appear limpid. The UVRR spectra were acquired at different values of temperature ranging from 293 to 368 K.

UV Raman scattering measurement

UVRR spectroscopy experiments were carried out using the setup descripted in detail in Chapter 2. The Raman spectra were collected at 228 and 266 nm of excitation wavelenght. Visible Raman spectra were collected on dry peptide powders by means of a micro-Raman spectroscopic setup (Horiba-JobinYvon, LabRam Aramis) with a spectral resolution of about 1 cm^{-1}. The exciting radiations at 633 nm and 532 nm were provided by a He-Ne and a Nd-Yag laser, respectively. The fitting procedure of the UVRR spectra of NAGMA and NALMA solutions in the amide region was implemented by using a sum of a minimum number of Pseudo-Voigt functions. All the parameters were initialized with reasonable values and then they were gradually released up to the convergence of the fit.

4.1.2 Results and discussion

Fig.4.2 shows the Raman spectra of dry peptides NAGMA and NALMA (panels at the left and at the right, respectively) collected by using different exciting radiations, ranging from 633 to 228 nm. As first remark, it has to be noted the variations in the relative intensity of the Raman peaks of both the peptides depending on the exciting wavelength, especially in the spectral region between 1200 and 1800 cm^{-1} . As common vibrational feature to all the spectra of Fig.4.2, it can be recognized the Raman signal at $\approx$1650 cm^{-1} that is assigned to the Amide I (AI) band. This mode is mostly due to the

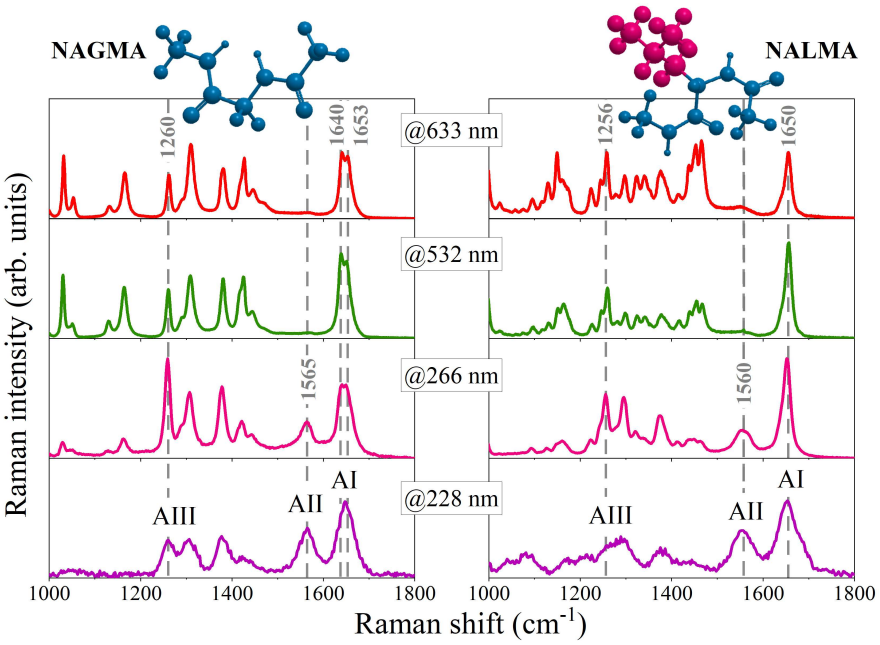

Figure 4.2: Raman spectra of dry NAGMA (panels at the left) and NALMA (panel at the right) excited at wavelengths of 633, 532, 266 and 228 nm and collected in the 1000-1800 cm^{-1} wavenumber region. The sketches at the top of the panels highlight the hydrophilic (atoms colored in blue) and hydrophobic (atoms colored in magenta) portions of the two peptides.

stretching vibration of the C=O of the amide linkage in the peptide backbone [89, 103–107]. Interestingly, AI mode appears splitted in two subcomponents at ≈1640 and 1653 cm^{-1} in the Raman profiles of NAGMA while the spectra of NALMA exhibit one single vibrational mode at ≈1650 cm^{-1} . This difference can be ascribed to fact that, in crystalline form, the amidic C=O groups of NAGMA peptide are differently involved in intermolecular H-bonds with respect to the interactions occurring in NALMA [108]. The presence of two components for AI in the spectra of NAGMA is consistent with the coexistence of C=O oscillators with a slight different strength. This suggests that the C=O groups of the NAGMA backbone can be engaged in more than one H-bond with the neighboring molecules. Conversely, the occurrence of one single peak for AI in the spectra of NALMA support the hypothesis that the C=O groups of the amide linkage in this peptide are mainly involved in only one H-bond or that both C=O interact with more or less the same strength.

This difference in the crystal arrangement of the two peptides could be ascribed to steric hindrance reasons. The UV-excited Raman spectra in Fig.4.2 show the progressive increasing at lowest excitation wavelengths of the Raman cross section of the amide II (AII) signal that is found at ≈1565 and 1560 cm^{-1} for NAGMA and NALMA, respectively. This vibrational mode results by the out-of-phase combination of N-H bending and C-H stretching movements of the groups in the amide linkage [89, 103–107] and it is usually completely absent in the spontaneous Raman spectra of peptides and proteins, as evident by inspection of Raman spectra excited at 633 and 532 nm in Fig.4.2. The strong enhancement of AII band both in the spectra of NAGMA and NALMA takes place at excitation wavelength of 266 and further increases at 228 nm. This trend is consistent with the increment of the molar absorptivity that occurs by approaching to the amide $\pi^* - \pi^*$ electronic transition at ≈190 nm and it has been previously observed also on other peptide systems [103, 104, 109]. The selective enhancement of AII band observed in Fig.4.2 for NAGMA and NALMA can be explained with the formation of H-bond involving the peptide amide sites that tend to stabilize the ground state dipolar resonance structure $^{-}$O-C=NH_2^+ that becomes more favored with respect to the neutral resonance structure O-C=NH_2[12]. The contraction of the C-N bond length results in turn in an enhancement of the Raman cross section of the AII vibrational mode. Interestingly, the UVRR spectra of Fig.4.2 evidence that the excitation wavelength at 266 nm gives rise to the highest enhancement for amide III band (AIII), especially for NAGMA peptide. This band is a very complex mode arising from the in-phase combination of N-H bending and C-H stretching [91, 105–107, 110, 111] and it is found at ≈1260 and 1256 cm^{-1} for NAGMA and NALMA, respectively, Since all the amide signals are very sensitive to the hydrogen bonds involving the peptide amide sites, these Raman bands can be used as marker of the local interaction between peptides and water at different experimental conditions. In particular, due to the different normal modes composition of these bands, AI band exhibits a major sensitivity to the H-bond engaging the C=O groups whereas the AII band is mainly affected by the interactions at the N-H site [112].

Fig.4.3 points out the concentration-dependence of UVRR spectra collected for aqueous solutions of NAGMA in the spectral region between 1000-1800

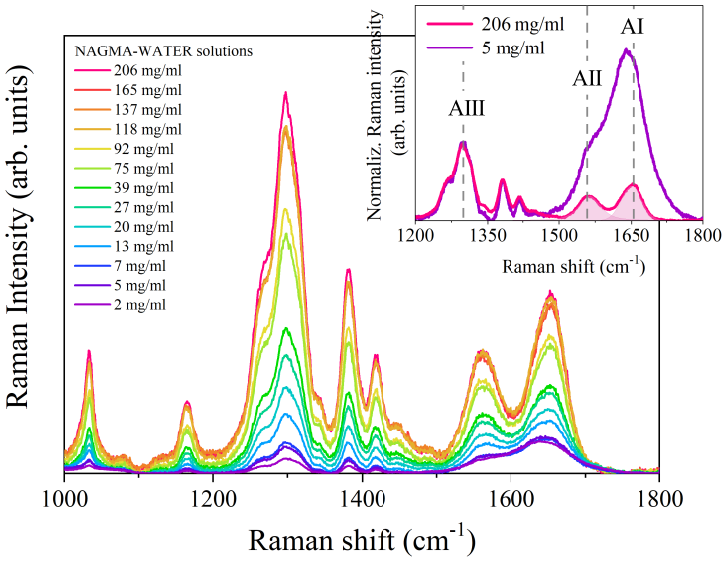

Figure 4.3: UVRR spectra of NAGMA aqueous solutions as a function of concentration collected between 1000 and 1800 cm^{-1} at 303 K. Inset: comparison between the UVRR spectra of the most concentrated (206 mg/ml) and most diluted (5 mg/ml) solution of NAGMA; the profiles have been normalized on the intensity of AIII band. An example of the spectral decomposition of the Raman profile into AI and AII bands is shown for the solution at 206 mg/ml.

cm^{-1} . It has been chosen to use 266 nm of wavelength for exciting the Raman profiles since in this resonance conditions all the three amide bands arise in the spectra with a relative comparable intensity. The collection of experimental profiles in Fig.4.3 displays significant spectral changes that occur varying the concentration of peptide NAGMA in water. A similar behavior is observed for the solutions of NALMA peptide (data here not reported). The most significant concentration-dependent modifications are observed for the shape and wavenumber position of AI and AII band whereas AIII signal remains substantially unchanged, as clearly evident by the comparison reported in the inset of Fig.4.3. It is to noteworthy that the improved sensitivity of UVRR spectroscopy respect to non-resonance technique allows to probe concentration-dependent modifications on AI band that are not detectable by using standard visible Raman scattering on similar solutions of NALMA in water [100]. This is probably related to the fact that the OH bending signal of water strongly dom-

inates the Raman spectra of solution of peptide around 1650 cm^{-1} , especially in very high diluted conditions [100].

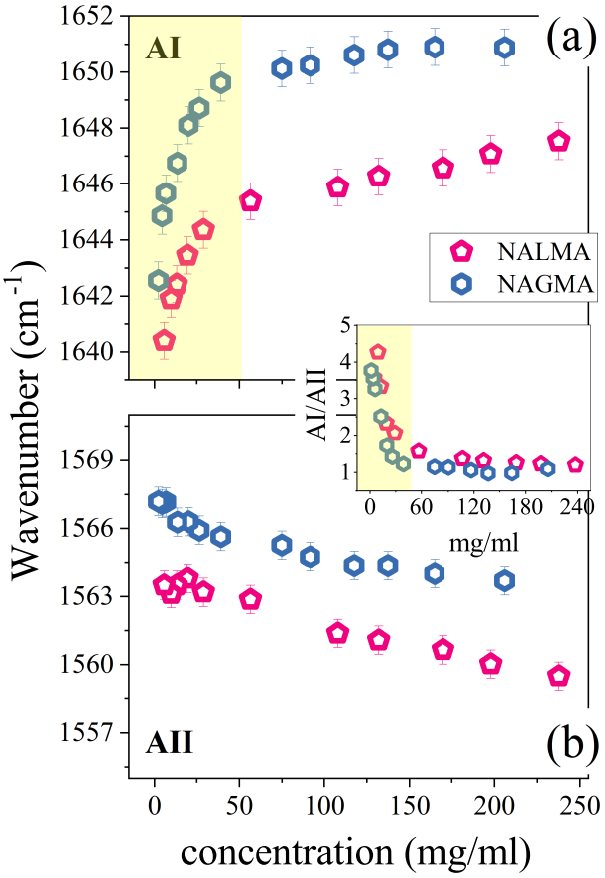

Figure 4.4: Concentration-dependence of wavenumber position observed for Amide I (a) and Amide II (b) bands of NAGMA and NALMA at 303 K. Inset: ratio between the intensity of AI and AII band for NAGMA and NALMA as a function of concentration of peptide in water.

Fig.4.4 shows the concentration-dependence of wavenumber position observed for AI and AII bands for the solutions of NAGMA and NALMA. The frequency positions of the two bands have been estimated by the spectral decomposition of the experimental profiles, performed by implementing the fitting procedure described in the section of experimental methods. An example of the spectral decomposition of the Raman profile into AI and AII bands is shown in the inset of Fig.4.3 for a solution of NAGMA. By looking to the trends in Fig.4.4, it can be clearly observed both for NAGMA and NALMA

that the increment of water molecules available per peptide in the more diluted solutions induces an opposite behavior for the two amide modes, i.e. a red-shift of AI band and a blue-shift for the AII signal. This finding suggests that at high dilution of peptide in water the solute-solute interactions become gradually more and more negligible and the amide C=O groups are more strongly involved in H-bond with the surrounding solvent molecules. Then, the corresponding CO oscillators are expected to vibrate at lower frequency. In line with this picture, the blue-shift observed for AII band in the plots of Fig.4.4 can likewise be explained by the contraction of the C-N bond length in the amide groups upon the increment of the number of water molecules bonded on C=O site [91, 109, 111–113]. More interestingly, while AII band shifts progressively to higher wavenumbers by increasing of dilution, AI signal exhibits a sharp decrement in the frequency position for concentrations of peptide in water lower than 50-60 mg/ml. A similar trend is also recalled by the severe increment observed for the ratio between the intensity of AI and AII band below the same concentration of ≈50 mg/ml and reported in the inset of Fig.4.4. It has to be noted that the behaviour is found common for the two peptides NAGMA and NALMA. This suggests a drastic change of the solvation properties occurring at concentration of 50-60 mg/ml for the peptide solute molecules that is more strongly reflected on the HB strength formed on the amide C=O groups of the peptide backbone. This is consistent with Optical Kerr Effect (OKE) measurements performed on aqueous solutions of NAGMA and NALMA [101] that identify a change in the water dynamics in correspondence of a concentration of peptide in water of about c=0.4 M (corresponding to ≈50 mg/ml for both the two peptides). The occurrence of these two concentration regimes is explained with a picture where at c<0.4 M the peptides molecules are homogenously distributed without significantly affecting the H-bond water arrangement, whereas for c>0.4 M the ice-like tetrahedral water network is strongly perturbed by the presence of the solutes. This explanation could be in line with the severe H-bond restructuring around the C=O peptide sites observed in the corresponding low concentration regime of NAGMA and NALMA in water. Moreover, the same behaviour exhibited by NAGMA and NALMA in Fig4.4 suggests a similar solvation dynamic for the pair of peptides in the explored regime of concentration. Fig4.5 display the

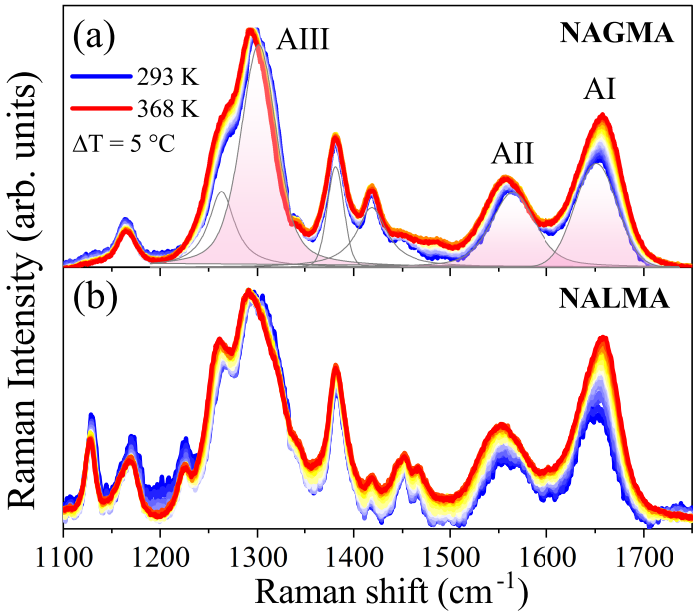

Figure 4.5: Temperature-evolution of UVRR spectra collected from 293 to 368 k for aqueous solutions of NAGMA (a) and NALMA (b) at concentration of ≈200 mg/ml. An example of spectral decomposition for the profile of NAGMA at 293 K is shown in the panel (a).

temperature-evolution of 266 nm-excited Raman spectra collected for concentrated aqueous solutions of NAGMA and NALMA. By inspection of Fig.4.5 (a) and (b), it appears evident that the increasing of temperature induces in both the solutions of peptides a slight upshift of the AI band while a more pronounced downshift of the AII and AIII signals is found. This trend, already observed on other peptide-water systems [109,114] reflects the effect of thermal motion on the oscillator strength of Amide modes [112] that is mediated by the changes induced on the H-bond interactions involving the amide peptide sites. In order to extract more quantitative information on the temperature dependence of the amide bands, the collections of UVRR profiles in Fig.4.4 have been fitted as described above. An example of spectral decomposition for the profile of NAGMA is shown in Fig.4.4(a).

Fig.4.6 displays the temperature-dependent evolution of the wavenumber position for AI, II and III bands for both the peptides NAGMA and NALMA. The trends observed for the wavenumber positions of all the Amide bands upon the increasing of temperature, i.e. blue-shift for AI and red-shift for AII and

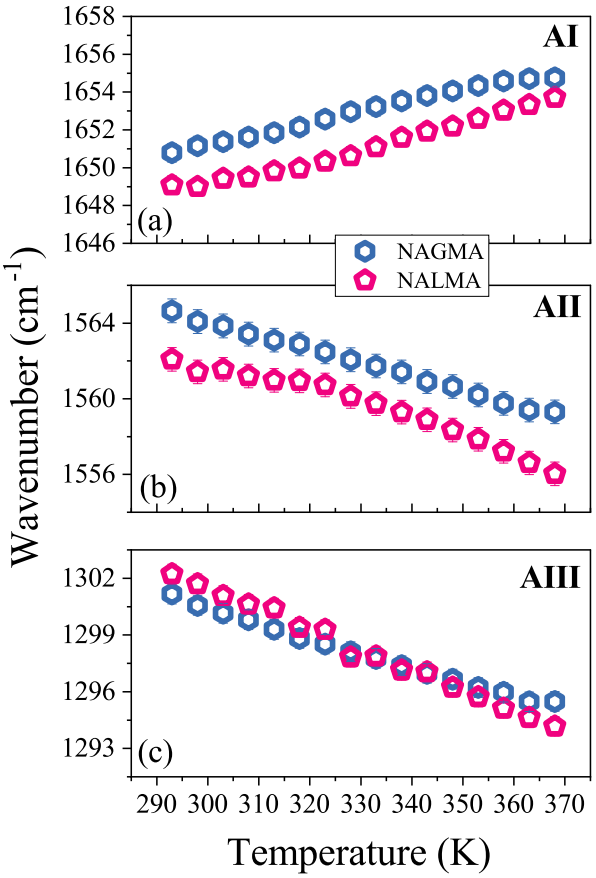

Figure 4.6: Temperature-dependence of wavenumber position observed for Amide I (a), II (b) and III (c) bands for aqueous solutions of NAGMA and NALMA (c≈200 mg/ml).

AIII, suggest a progressive weakening of the HB between water molecules and the amide C=O and N-H groups of the backbone of the two peptides, due to the increasing of thermal motion. The opposite temperature-behaviour found for the amide bands was expected on the basis of the different normal mode composition of these bands [112], as discussed above. Fig.4.6(a) and (b) point out also a redshift of some cm^{-1} observed for the wavenumber position of AI and AII band of NALMA with respect to NAGMA. The difference persists over the whole investigated temperature and concentration ranges (see trends reported in Fig.4.4). This finding can be related to the presence of the hydrophobic portion in the structure of NALMA that tends to affect the distribution of the water molecules around peptide backbone. Molecular dynamics simula-

tions [115] suggest that the solvent molecules are quite uniformly distributed around hydrophilic peptide NAGMA while they prefer to orient around the hydrophilic portion of NALMA instead than around its hydrophobic side chain. This is consistent with a general major strength observed for the water-solute interactions that involve both the C=O and the NH groups of the backbone of NALMA with respect to NAGMA.

4.2 Solvation of glutathione in presence of ionic liquids

The unique physical-chemical properties of IL have motivated a growing interest in their use as solvents in a broad variety of technical applications ranging from chemistry over physics to biological sciences. For all these applications, the unique architecture of IL, consisting of a large variety of combinable anions and cations, allows for an enormous number of possibilities for a fine tuning of properties such as viscosity, polarity or miscibility with other molecul ar liquids and solvents. More recently, the studies on the toxicity of IL toward living organisms has stimulated several chemical-physical investigation on the interaction between IL and basic biological systems, such as saccharides, membranes, peptides/proteins and nucleic acid [116–118]. In particular, it has been found that certain IL exhibit several positive effects on proteins, including an increased thermal stability, the suppression of aggregation and an enhanced refolding ability [119]. In this context, IL can act both as solvents replacing water and volatile organic compounds and as additives able to affect the properties of proteins in water solution [119, 120]. Despite the large efforts devoted to the study of the behavior of proteins in ILs or their aqueous solutions, much less is known about the IL interactions with peptides and oligopeptides, although this would certainly help to clarify the complex phenomena occurring between proteins and IL. The fundamental investigation of the effect of IL on small peptide systems is a prerequisite step in order to better understand and predict the composite effect felt by more complex proteins [121]. Some experimental results have reported on the effect of addition of imidazolium-based IL to water solutions of short linear and cyclic

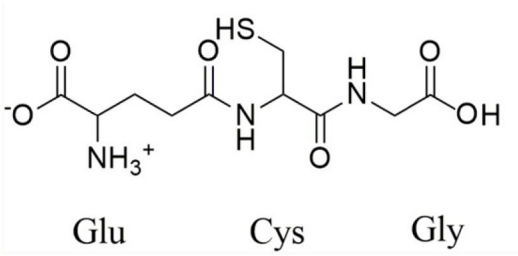

Figure 4.7: Structure of GSH in its protonated form.

glycine peptides [122, 123]. The studies, performed by using NMR, suggest that the choice of anion of IL and the IL concentrations strongly affect the solubility and stability of peptides in solution [123]. However, a comprehensive overview, at molecular level, of the fundamental aspects of the interactions between peptides/oligopeptides and imidazolium-based IL is still lacking. The present study aims to provide new insights on the mechanism of interactions between imidazolium-based IL and a model peptide, i.e. reduced glutathione (GSH). It is a tripeptide, present as a sub-major constituent in the intracellular space of plants, animals andmicroorganisms, composed by three amino acid residues, i.e. glutamic acid (Glu), cysteine (Cys) and glycine (Gly). Its chemical structure is shown in Fig.4.7. The major role of GSH is in the enzymatic reduction of hydrogen peroxide and other peroxides and in general in the protection of cell components against oxidation for maintaining a reducing cellular environment. Indeed, the thiol group of GSH is a powerful reducing agent that has, as a target, the Reactive Oxygen Species (ROS). The tripeptide exists in the organisms in its reduced (GSH) and oxidized (GSSG) states, and maintaining an appropriate ratio between these two forms is fundamental to prevent cellular oxidative stress. If there is a deficiency of GSH in the cell environment, there is the risk of membrane oxidation, which is related with the onset of a great amount of pathologies [124–126].

The systematic investigation of the effect of IL on the solvation properties of GSH should lay the foundation for a broader understanding of the IL–peptide and IL–protein interactions, also in view of the development of peptide chemistry and biochemistry applications. In this sense, experimental methods of molecular resolution would certainly represent a useful tool for clarifying the basic principles of the underlying unique peptide/IL interactions. In light of

the great potentiality of UVRR spectroscopy shown in the previuos session, UVRR experiments have been carried out in order to elucidate the solvation properties of GSH in pure water and in a binary mixture water/ILs. In particular, we have selected imidazolium-based ILs with different anions choosing from those of the halogen group (Cl^-,Br^- and I^-), in order to focus the attention on the effect of these anions on the solvation dynamics of GSH. It has been observed in previous works that usually the variation of the anion tends to exhibit higher effects on proteins stability compared to change of the cation [127]. This has been explained by invoking the fact that anions are more polarizable compared to cations [128].

4.2.1 Experimental method

Sample preparation

GSH ($C_{10}H_{17}N_3O_6S$, γ-L-Glutamyl-L-cysteinyl-glycine) was purchased from Sigma Aldrich ($\leq$ 98.0%) and used without further purification. 1-butyl-3-methylimidazolium chloride ([BMIM]Cl), 1-butyl-3-methylimidazolium bromide ([BMIM]Br) and 1-butyl-3-methylimidazolium iodide ([BMIM]I) were purchased from IoLiTec with a purity of 99%. GSH peptide was dissolved in IL/water solution obtaining a final concentration of 20mg/mL with a molar ratio 1:1 for GSH and IL.

UV Raman spectroscopy measurements

UVRR spectroscopy experiments were carried out using the setup descripted in detail in Chapter 2. The Raman spectra were collected at 266 nm. The spectral resolution was set to about 6 cm^{-1} in order to have a satisfactorily high signal to noise ratio. The calibration of the spectrometer was standardized using cyclohexane (spectroscopic grade, Sigma Aldrich). The power of the beam on the sample was kept sufficiently low (a few μW) in order to avoid photo-damage effects and heating of the sample.

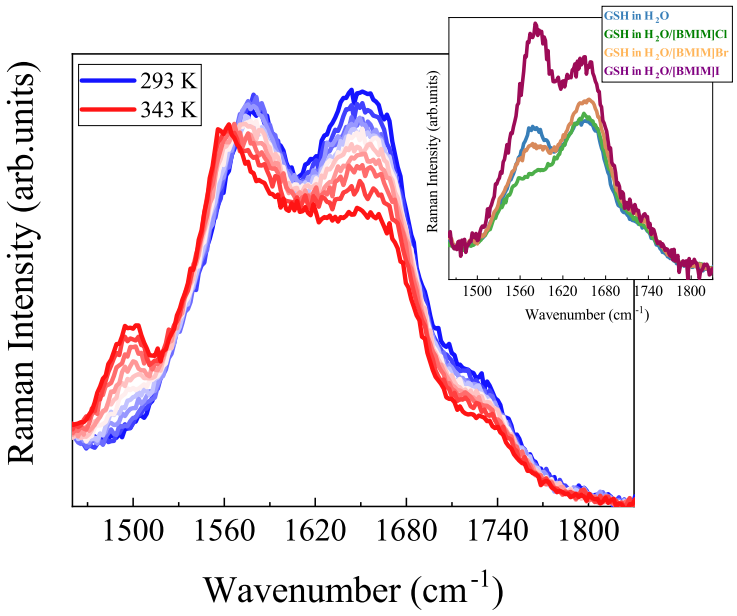

Figure 4.8: Temperature-evolution of UVRR spectra collected at 266 nm from 293 to 343 K (ΔT= 5 K) for aqueous solution of GSH. Inset: Comparison among UVRR spectra of GSH in pure H_2O (blue curve), [BMIM]Cl/H_2O (green curve), [BMIM]Br/H_2O (orange curve) and [BMIM]I/H_2O (violet curve) solutions at 293 K.

4.2.2 Results and discussion

Fig.4.8 shows the temperature-evolution of the UVRR spectra collected for GSH in aqueous solution. Similarly to the case of NAGMA and NALMA, the increasing of the temperature from 293 to 343K induces a slight upshift of the AI band and a more pronunciated downshift of AII. The opposite temperature behavior, down- and up-shift found for AI and AII respectively, can be rationalized by considering the different normal mode composition of these modes. In particular, the sensitivity to H-bonds strength of the AI mode mainly derives from the C=O group of the peptide while the frequency dependence of the AII vibration primarily is due to the H-bond involving the N-H groups of the peptide linkage. With increasing temperature, it clearly appears a signal at 1500 cm^{-1} that is assigned to the cis-amide bands (cis-AII). This band is a marker of the conformational change from trans to cis isomer of GSH promoted by the thermal motion. The intensity of the cis-AII band increases with the

increasing of temperature but without any frequency shift, differently to the trans-AII temperature behavior. This suggests that cis–AII signal is mainly due to C-N stretching [109]. The experimental UVRR profiles of GSH have been analyzed in the spectral region between 1500 and 1800 cm^{-1} in order to extract more quantitative information and to better compare the effect induced by the different ILs. To this purpose, a fitting procedure of the experimental data has been implemented in order to extract the most significant parameters of Amide bands, i.e. the frequency position and intensity of AI and AII.

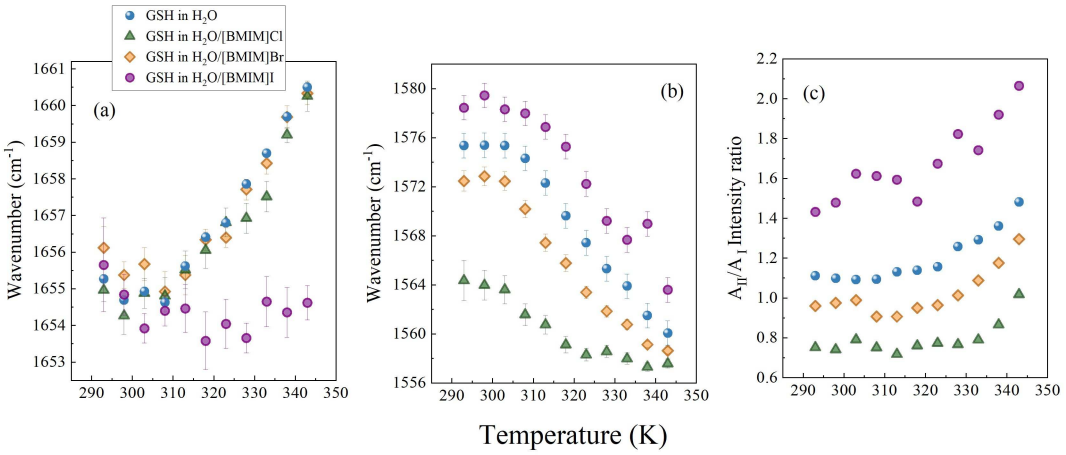

Figure 4.9: Temperature-dependence of wavenumber position observed for Amide I (a) and II (b) and intensity ratio of AII/AI (c) for GSH dissolved in pure H_2O (blue circles), [BMIM]Cl/H_2O (green triangles), [BMIM]Br/H_2O (yellow rhombs) and [BMIM]I/H_2O (violet circles) solutions.

Fig.4.9(a-b-c) display the temperature-dependence evolution of the wavenumber position for AI and AII bands and the intensity ratio between AII and AI band for GSH in the different solvents. By inspection of Fig.4.9(a) it appears that the thermal dependance exhibited by the frequency of AI is practically the same for GSH in aqueous solution and in presence of [BMIM]Cl and [BMIM]Br. For all these systems, a blue shift of about 5 cm^{-1} is observed as a consequence of the increment of temperature from 293 to 343 K. As discussed also for NAGMA and NALMA, this behaviour is consistent with a weakening of H-bonds established between amide carbonyl groups and the surrounding molecules inside the hydration shell of peptide. A different behaviour is observed for the case of GSH dissolved in [BMIM]I/H_2O solution, where the AI

band remains at the same frequency position in all the explored temperature range. This result suggests a strong capability of [BMIM]I to form H-bonds with the carbonyl groups of peptide backbone on GSH whose strength is only slightly affected by the temperature changes. Panel (b) of Fig.4.9 displays the comparison between the temperature-dependance of frequency position of AII for GSH dissolved in the pure water and IL/water solutions. Considering the normal mode composition of AII, the observed red-shift as a function of temperature is consistent with the weakening of H-bonds involving N-H groups of the peptide linkage. With respect to GSH dissolved in pure water, it is possible to notice that the AII band is red-shifted in presence of [BMIM]Cl and [BMIM]Br, especially at low temperature. The highest downshift is found in presence of the chloride anion. At the contrary, in the presence of [BMIM]I the AII frequency is blue-shifted compared to the position observed for GSH in pure water in all the temperature range explored. This means that Cl and Br anions are able to decrease the oscillation vibrational frequency at the NH site of the peptide link, consistently with the anion electronegativity strength. Conversely, the presence of iodide anion affects the NH site by inducing an increasing of the oscillation frequency of AII vibration. Both the red-shift than the decreasing of AI intensity (see Fig.4.9c) suggest that Cl anion mooves the equilibrium of GSH structure towards the non-zwitterion form of peptide link. The same role is also played by Br anion but in less evident matter. Conversely, I^- favours the zwitterion form of peptide GSH that is reflected both in a blue-shift and in an enhancement of AII band intensity. Other experimental investigations are currently underway in our group in order to better explain the IL-GSH interaction with the aim to support the vibrational spectroscopy results with molecular dynamic simulation. This will permit to identify the site of interaction of GSH with anion species.

Chapter 5

Conformational stability of DNA in ionic liquid-water solutions

Deoxyribonucleic acid (DNA) is a macromolecule of pivotal biological role thanks to its ability to store the genetic instructions for the growth, functioning and development in the cell. It plays key role in many biological processes, i.e. gene expression transcription and carcinogenesis [130]. Due to its properties together with its chiral structure [131], DNA represents a key component in pharmaceutical and biomedical studies and a crucial material in the development of advanced molecular device [132, 133]. From a structural point of view, DNA is composed of two linear strands of nucleotides that coil around each other to fomr the characteristic double helix structure. Each nucleotides is composed by a phosphste group, a deoxyribose monosaccharidic unit and one of the four nucleobases (adenine, cytosine, thymine and guanine). The nucleobases of the two chains interact by H-bond, according to the base-pairing rules, connecting the two sugar-phosphate backbones. More precisely, purines form H-bonds to pyrimidines, with adenine bonding only to thymine in two hydrogen bonds, and cytosine bonding only to guanine in three H-bonds. This arrangement of two nucleotides binding together across the double helix is called a Watson-Crick base pair.

Fig.5.1 reports a representative chemical structure of DNA for two Watson-

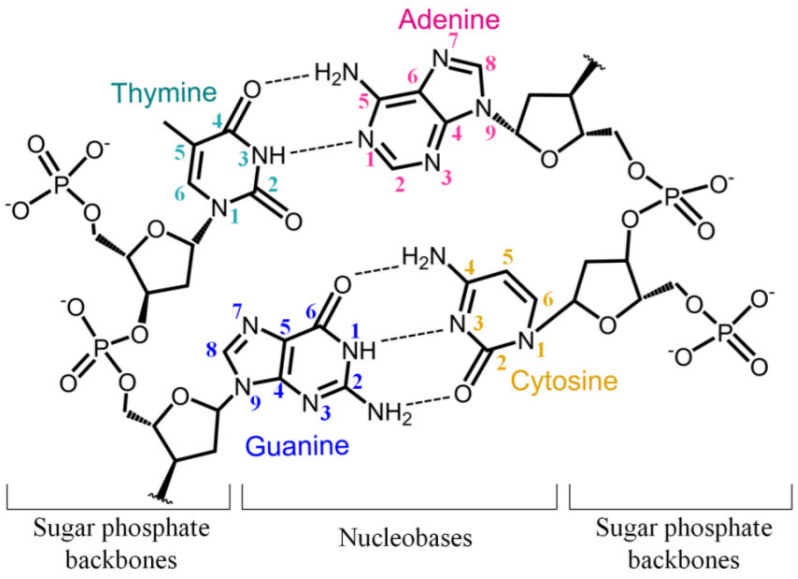

Figure 5.1: Chemical structure of DNA for adenine-thymine and guanine-cytosine base pairs. Dashed lines represents Watson-Crick H-bonds.

Crick base-pairs with the conventions adopted for the numbering of atoms. The asymmetrical spacing of the sugar-phosphate backbones generates major grooves (where the backbone is far apart) and minor grooves (where the backbone is close together). Certain proteins bind to DNA to alter its structure or to regulate transcription (copying DNA to RNA) or replication (copying DNA to DNA) (see Fig.5.2).

The use of Raman spectroscopy for investigating the structure and dynamics of DNA started in the late of 1960s and thereafter Raman-based methods have been continuously implemented to probe nucleic acids and their biological complexes [134–138]. The complex chemical composition of DNA and the fact that usually the reproducing of physiological conditions requires to investigate DNA in high diluted conditions (< 1 mg/mL) are the main limitations to the application of conventional Raman spectroscopy to the study of this biological macromolecule. Off-Resonance Raman spectra of DNA are characterized by a strong overlapping of spectral contributions arising from different nucleobases that can not be easily disentangled each other. UVRR spectroscopy takes the advantage to selectively enhance the Raman bands that are mainly localized

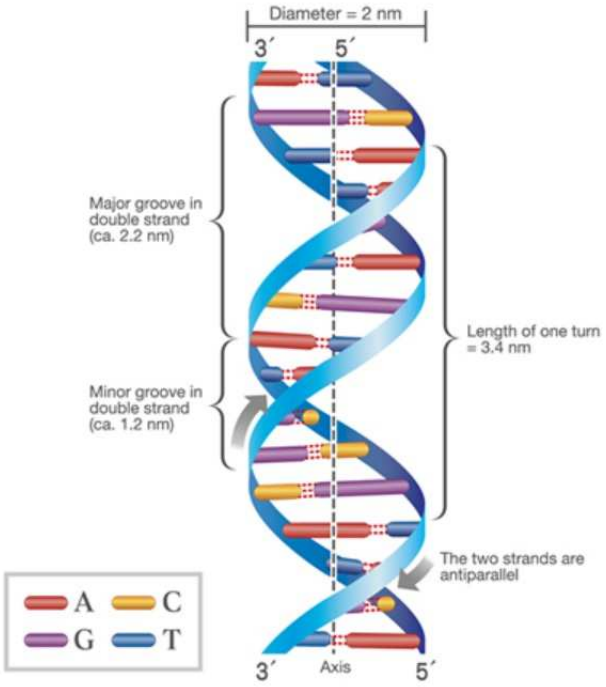

Figure 5.2: Structure of double-stranded DNA (type B).

on nucleotides rings. Then, the UVRR spectra of DNA are dominated by the vibrational peaks associated to the four bases cytosine, guanine, adenine and thymine while the Raman signals associated with the phosphate and sugar backbones, as well as those arising from buffer and solvent are practically negligible [139, 140].

5.1 Selectivity of UVRR spectroscopy on nucleobases

Fig.5.3 shows the comparison between the UV absorption spectra of 2'-deoxycytidine 5'- triphosphate (dCTP), 2'-Deoxyguanosine 5'- triphosphate trisodium (dGTP), 2'-deoxyadenosine 5'- triphosphate (dATP), thymidine 5'-triphosphate (dTTP) and salmon DNA in the region between 210 and 300 nm. The structures of nucleobases with the conventional atom numbering are displayed on the top panel of Fig.5.3. The absorbance spectrum of cytosine

(dC) shows a band at $\sim$ 275 nm and a shoulder at $\sim$ 230 nm. The absorbance spectrum of guanine (dG) presents two electronic transitions. The first one, centered at $\sim$ 255nm and labeled as transition I, is localized on the N7=C8 site, while the second transition, centered at $\sim$ 275 nm and designated as transition II, involves the triene fragment (C2=N3-C4=C5-N7=C8). Adenine (dA) absorption spectrum displays the transition I localized on the N7=C8 double bond at $\sim$ 260 nm. Finally, the absorption spectrum of thymine (dT) exhibits a single transition at $\sim$ 265 nm associated with the enone fragment (C5=C6-C4=O) [141].

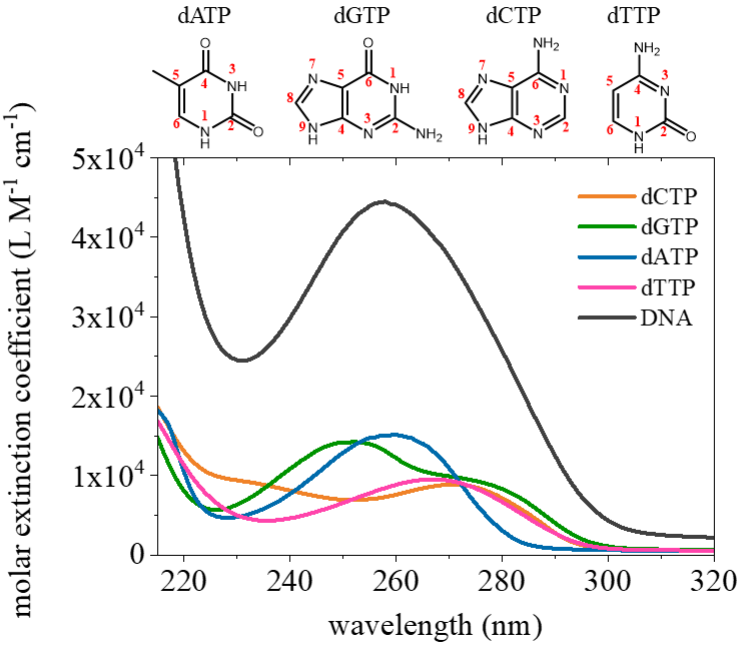

Figure 5.3: UV absorption spectra of aqueous solution of deoxynucleotides dATP, dCTP, dGTP, dTTP and salmon sperm DNA. Top panel: scheme of the structure of nucleotides and numbering adopted for atoms.

Thanks to the quite different UV absorbance pattern exhibited by nucleotides, a careful choice of the excitation wavelength in correspondence of the electronic transitions of specific nucleobases allows to emphasize in the UVRR spectra of DNA the contributions arising from individual bases [142]. This clearly appears by inspection of Fig.5.4 that displays the comparison

among the UVRR spectra of salmon DNA excited at 228, 250, 260 and 272 nm.

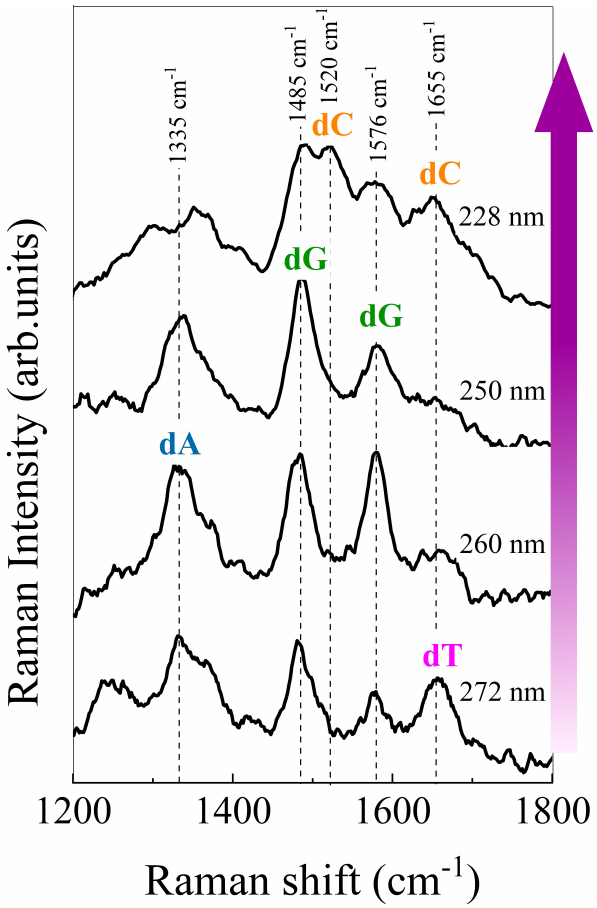

Figure 5.4: UVRR spectra of aqueous solution of salmon sperm DNA collected at 228 nm, 250 nm, 260 nm and 272 nm of excitation wavelength. Capital letters indicate the vibrational features assigned to vibrations localized on different nucleobases.

The main spectral features observed in the UVRR profiles of DNA in Fig.5.4 have been assigned to specific vibrations of purine and pyrimidine bases, as reported in Tab.5.1.

The greater molar absorptivity of dC compared to the other bases dA, dG and dT at about 228 nm (see Fig.5.3) results in a selective enhancement of the vibrational signal associated to dC in the UVRR spectra excited with this wavelength (Fig.5.4) [143]. In particular, it is possible to recognize the vibrational peaks centered at about 1520 and 1650 cm^{-1} that are assigned to a

Exp. Freq.	228nm [145]	250nm [144]	260 nm [139, 141]	272nm
1335 cm^{-1}	**dG** δ(C8H)+ν(C8N7) **dA** ν(C8N7)+ν(C5N7)	**dA** ν(C8N7)+ν(C5N7) **dG** δ(C8H)+ν(C8N7)	**dA** ν(C8N7)+ν(C5N7)	**dA** ν(C8N7)+ν(C5N7)
1485 cm^{-1}	**dG** ν(C8N7)+ν(N9C8)+ +δ(C8H) **dT** ν(N1C2)+ν(C2N3)	**dG** ν(C8N7)+ν(N9C8)+ +δ(C8H)	**dG** ν(C8N7)+ν(N9C8)+ +δ(C8H) **dA** ν(N9C8)+δ(C2H)+ +δ(C8H9)	**dA** ν(N9C8)+δ(C2H)+ +δ(C8H9) **dG** ν(C8N7)+ν(N9C8)+ +δ(C8H)
1520 cm^{-1}	**dC** ν(N3C4)+ν(N1C2)			
1576 cm^{-1}	**dA** ν(C5C4)+ν(C4N3) **dG** ν(C5C4)+ν(C4N3)+ +ν(N7C5)	**dG** ν(C5C4)+ν(C4N3)+ +ν(N7C5)	**dG** ν(C5C4)+ν(C4N3)+ν(N7C5) +ν(N7C5) **dA** ν(C5C4)+ν(C4N3)	**dA** ν(C5C4)+ν(C4N3) **dG** ν(C5C4)+ν(C4N3)+ +ν(N7C5)
1650 cm^{-1}	**dC** ν(C2O)+ν(C2N3)	**dT** ν(C4O)+ν(C5C4) **dC** ν(C2O)+ν(C2N3)	**dT** ν(C4O)+ν(C5C4) **dC** ν(C2O)+ν(C2N3)	**dT** ν(C4O)+ν(C5C4)

Table 5.1: Assignment of main vibrational features in the UVRR spectra of DNA excited at 250 nm and 266 nm

coupled stretching of N3-C4 and N1-C2 and to a coupled stretching of C2=O and C2-N3 of dC, respectively [144]. Fig.5.4 evidences significant changes in the UV resonance Raman enhancement pattern of DNA by shifting the excitation wavelength from 228 to 250 nm. The 250-excited UVRR spectrum is dominated by the vibrational mode at $\sim$ 1485 associated to dG residue and assigned to a combination of bending motion of C8-H and stretching movement of C8=N7 and N9-C8. Similarly, the Raman band at $\sim$ 1576 cm^{-1} is associated to a stretching mode of bonds C4-N3, C5-C4 and N7-C5 of triene moiety [145]. The UVRR spectrum of DNA excited at 260 nm allows to better enhance the signals arising from dA residue, as expected by the high molar absorptivity of this nucleobase at this wavelength (see Fig.5.3) [140]. In particular, the band at $\sim$ 1335 cm^{-1} is mainly due to the stretching of C5-N7 and N7-C8 bonds of the purine ring of dA [143]. Moving to 272 nm of excitation wavelength, it is possible to observe in the corresponding UVRR spectrum of DNA (see Fig.5.4) a significant enhancement of the vibrational mode centered at about 1655 cm^{-1}. This Raman peak is probably to be assign to a coupled stretching of C4=O and C5=C6 bonds of dT [144], consistenlty with the electonic transition observed for dT at $\sim$265 nm.

5.2 Conformational stability of DNA in aqueous solution

The conformational stability of DNA is strongly influenced by the interaction between the backbone of DNA and the surrounding solvent molecules [146, 147]. In particular, different buffer conditions i.e. pH, type and concentration of salts, may affect the thermal stability of DNA [148]. UVRR spectroscopy has been implemented by different authors for probing at molecular level the changes induced on DNA by the increasing of thermal motion, by exploiting the selectivity of the technique [149–153]. As example, we report here the investigation of the thermal stability of DNA in two different buffers, i.e. i) Phosphate buffered saline (PBS) 10 mM, pH 7.4 and ii) Tris-HCl buffer (TRIS) 10 mM, pH 7.4. Fig.5.5 shows the temperature-evolution of UVRR spectra collected for DNA in PBS in the wavenumber range 1270-1760 cm^{-1}. The profiles have been excited at 250 nm in order to selectively enhance the vibrational contributions mainly arising from dG nucleobase. This is justified by the sensitivity shown by several dG Raman peaks that can be used as molecular markers of the DNA unfolding process.

As first remark, it is possible to note that the band centered at 1612 cm^{-1} downshifts to 1602 cm^{-1} upon the increasing of temperature. This vibrational feature is attributable to the scissor vibrations of the NH_2 group of dG that is involved in H-bond with the C2=O moiety of dC. The observed red shift of the band at 1612 cm^{-1} can be correlated to a reduction of the Watson-Crick H-bonding strength between G-C base pairs, promoted by the increasing of thermal motion [153]. The spectra in Fig.5.5 point out a significant increase in the intensity of the peak centered at $\sim$ 1485 cm^{-1} as a function of temperature. This behavior, analogous to the observed UV absorbance hyperchromism of DNA, has been associated to the DNA thermal denaturation [151] (the so-called Raman hyperchromic effect) and it reflects the interdependence between the Raman scattering cross-section and the electronic absorption intensity. The increment of the resonance of aromatic ring of nucleotides upon thermal denaturation has been ascribed to two effects: i) the disruption of vertical base-base stacking interactions and ii) the breakage of

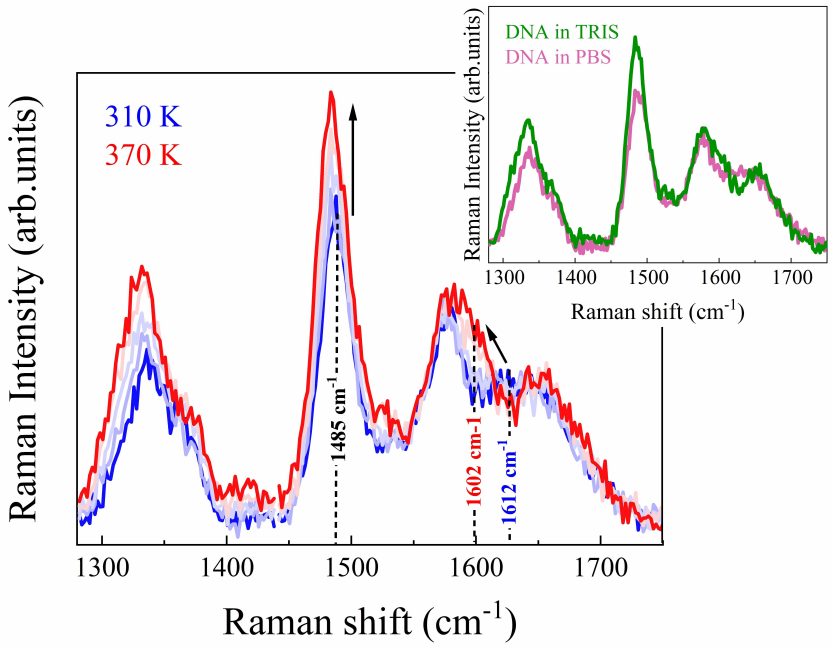

Figure 5.5: Temperature-evolution of UVRR spectra of DNA in PBS excited at 250 nm. Inset: Comparison between UVRR spectra of DNA in PBS and TRIS buffers at 345 K, the two spectra were normalized via the intensity of the OH stretching band of water at 3400 cm^{-1}.

H-bond between complementary bases in the double strand of DNA [149,154]. The inset of Fig.5.5 shows the comparison between the UVRR spectra of DNA in PBS and TRIS at 345 K normalized via the intensity of the OH stretching band of water at 3400 cm^{-1}. Interestingly, at this temperature, the red-shift of the band at $\sim$ 1612 cm^{-1} and the increment in the intensity of the peak at $\sim$ 1485 cm^{-1} are further enhanced in the sample of DNA in TRIS compared to that in PBS. This finding suggests that the melting transition occurs at lower temperature for DNA in TRIS, as it appears evident by inspection of Fig.5.6. Here, the temperature dependence of the UVRR intensity for the dG band at $\sim$ 1485 cm^{-1} is reported for DNA in TRIS and in PBS.

Both the trends exhibit a sharp increasing in correspondence of $\sim$ 343 and $\sim$ 352 K for DNA in TRIS and in PBS, respectively. This characteristic behavior, already observed for similar DNA systems [151–153], has been associated to the melting transition of DNA that involves the full denaturation of the

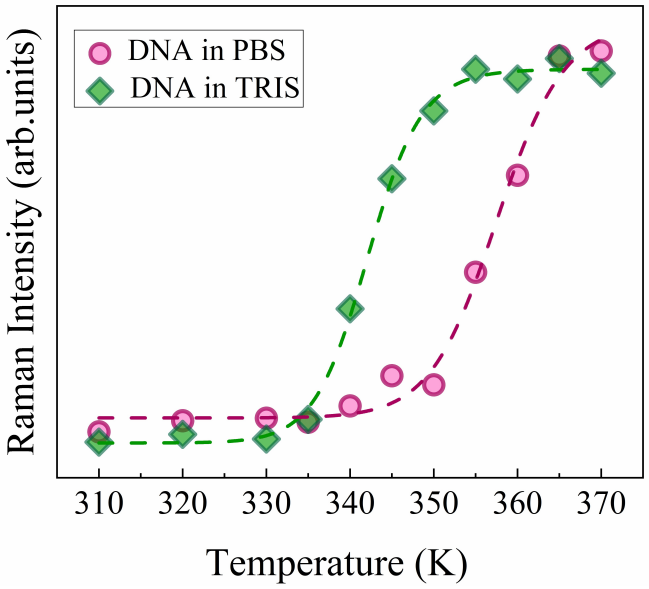

Figure 5.6: Temperature-dependence of the intensity of the vibrational mode at $\sim$ 1485 cm^{-1} assigned to ν(C8=N7) + ν(N9-C8) + δ(C8H) of dG for DNA in TRIS and in PBS.

double-stranded structure, in turn related to un-stacking interactions involving dG residues. The plots in Fig.5.6 suggest that DNA conformation is more stabilized in PBS than in TRIS buffer solvent.

5.3 Complementarity of UVRR and IR spectroscopies for investigation of DNA

UVRR spectroscopy can be implemented for the investigation of DNA also in combination with Fourier transform infrared (FTIR) spectroscopy, due to the strong complementarities of these two techniques [155–157]. While UVRR spectroscopy is particularly sensitive to the vibrational modes arising from the nucleobases, FTIR spectroscopy can efficiently probe the phosphodiester back-bond of DNA [156, 158]. Fig.5.7 displays the comparison between the attenuated total reflectance Infrared (ATR-IR) spectra and the UVRR profile of salmon DNA in the wavenumber region between 800 and 1800 cm^{-1}.

The FTIR spectrum is dominated by the vibrational features falling between 900 cm^{-1} and 1300 cm^{-1} that are associated to vibrations of phosphate

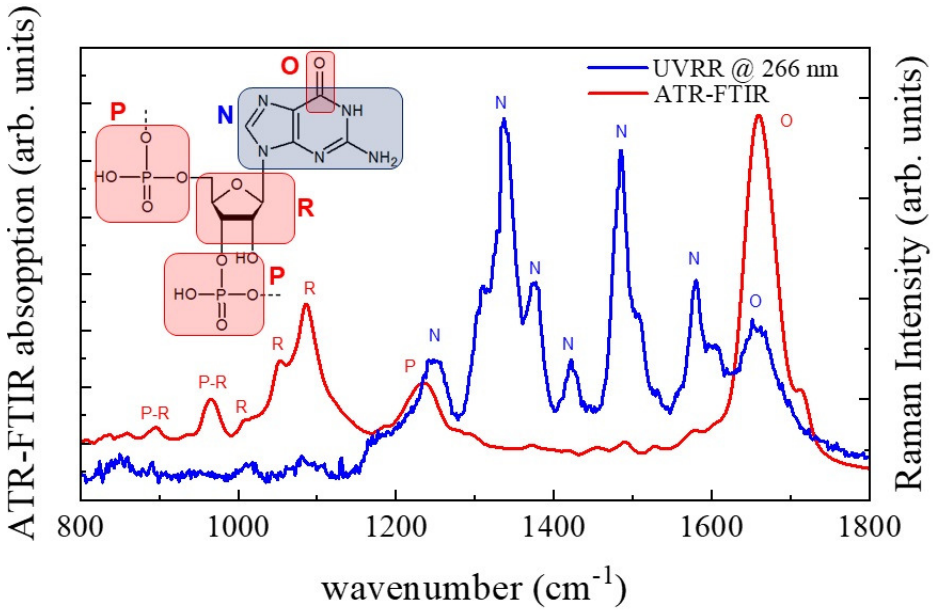

Figure 5.7: Comparison between ATR-FTIR and UVRR spectra of salmon DNA in the wavenumber region between 800 and 1800 cm^{-1}.

and ribose functional groups of DNA [157]. As evident by the comparison with UVRR spectrum, these modes are practically not detected by UVRR spectroscopy. The IR bands assigned to phosphate and ribose moieties are specifically informative on the folding state of DNA. Conversely, the region between 1300 to 1600 cm^{-1} shows the presence of the Raman peaks due to the ring vibrations of nucleobases that are not active in the IR spectrum. As expected, the intense IR band centred at 1680 cm^{-1} is associated to the C=O stretching mode of the carbonyl groups in dG, dT and dC.

5.4 Molecular mechanism of interaction between DNA and hydrated ILs

Although DNA is considered stable in aqueous solution, slow hydrolytic reactions such as deamination and depurination may denature the double helical DNA conformation [159]. For this reason, a growing interest has been devoted to the development of suitable aqueos solvents to improve the stabilization of

DNA [148, 160]. This could open the possibility to maintain the native DNA structure for a long period and in critical conditions, such as high temperature and pressure [161].

ILs have proven to be the preferred solvents to replace the traditional organic solvents and/or aqueous solutions in many types of reactions [162, 163]. During the last years, the application of ILs to DNA technology has received particularly attention. For instance, in literature is reported the use of ILs for the extraction of trace amount of DNA from the aqueos solution [163], for slowing DNA translocation through nanopores [164] and for the DNA storage [165]. All such application are strongly dependent on the interaction at molecular level between ILs and DNA. A basic understanding of IL-DNA interaction could drive to a tailored use if ILs in various fields of life science. Several theoretical studies investigate the interaction of DNA with pure ILs and/or with IL-water solutions. Molecular dynamics simulation results suggest that both the groove binding mechanisms of IL cations and their electrostatic association with DNA backbone contribute significantly to DNA stability [166, 167]. However, no experimental findings are present in the literature in support of this hypothesis. DNA/IL systems are widely investigated by circular dichroism, fluorescence and UV/Vis spectroscopies [165, 168–170]. However, these techniques provide information on the stabilizing or destabilizing effect of ILs on the DNA natural conformation, but do not give detailed information on the molecular interactions causing such effects. A comprehensive experimental picture in terms of molecular interactions involved in DNA/ILs and the thermodynamics of the interaction is still missing.

In this work, it is explored the thermal stability of DNA in water in presence of imidazolium-based ILs by synchrotron-based UVRR scattering. This technique represents a powerful tool for investigating the nature of inter-molecular interactions established between the IL cations and DNA bases. This is due to the selectively enhancement, in resonance condition, of the vibrations mainly localized on nucleotides ring. This allows to minimize the Raman signal associated with the phosphate and sugar backbones, as well as those arising from buffer and solvent [139, 140], thus simplyfing the complex Raman spectra of DNA. Moreover, the tunability of UV synchrotron radiation source permits a careful choice of the excitation wavelength in correspondence of the elec-

tronic transitions of specific nucleobases. Such approach allows to disentangle in a very efficient way the contributions arising from individual bases in the spectra of DNA [142]. In particular, the choice of 250 nm as excitation wavelength gives the opportunity to enhance and isolate the ring in-plane vibration associated to the guanine residues [145]. This Raman feature is highly sensitive to the un-staking interactions between bases induced by the increment of thermal motion and it can be used as molecular marker of thermal denaturation of DNA. Circular dicroism (CD) and UV-absorption measurements have been performed to complement the molecular description obtained by UVRR spectroscopy results.

5.4.1 Experimental methods

Sample preparation

1-butyl-3-methylimidazolium methylsulfate, [BMIM]$MeSO_4$, was purchased by IoLiTec with a purity of 99%. Deoxynucleodite (dNTP) set composed by: 2'-deoxyadenosine 5'- triphosphate sodium salt solution (dATP), 2'-deoxycytidine 5'- triphosphate disodium salt (dCTP), 2'-Deoxyguanosine 5'- triphosphate trisodium salt solution (dGTP) and thymidine 5'- triphosphate sodium salt solution (dTTP) at 100 mM was purchased by Sigma-Aldrich. Each dNTP was diluted in 10 mM of PBS pH 7.4 in order to reach the final concentration of 5 mM. DNA sodium salt from salmon testes (2000 base-pairs, CAS number 438545-06-3) was purchased by Sigma-Aldrich and used without further purification. The absence of proteins as contaminants [185] was checked by measuring the absorbance ratio of a DNA solution at 260 and 280 nm that was found to be equal to 1.9. A DNA stock solution of 1 mg/mL was prepared by dissolving an appropriate amount of dry DNA in PBS and gently stirring for 24 h to achieve a limpid solution. A detailed description of DNA/IL samples preparation for Raman spectroscopy measurements is reported in Tab.5.2. For CD and UV-vis measurements the sample was diluted 1:8 with respect to samples used for Raman analysis due to the great absorbance.

DNA in PBS	DNA in PBS & IL
250μL of DNA stock sol. (1mg/mL)+ 750μL of PBS	250μL of DNA stock sol. (1mg/mL)+ 740μL of PBS + 10μL of IL

Table 5.2: Description of DNA/IL samples preparation.

Raman spectroscopy measurements

UVRR spectroscopy experiments were carried out by using the setup descripted in detail in Chapter 2. The exciting wavelengths used for collecting Raman spectra were set at 250 and 266 nm with a spectral resolution of 15 and 5 cm^{-1}, respectively. For each sample, UVRR spectra were recorded in the temperature range from 305 to 370 K. In order to compare the DNA spectra in presence and absence of [BMIM]$MeSO_4$ at a given temperature, the experimental profiles were normalized via the intensity of the OH stretching band of water at 3400 cm^{-1} [144]. In the spectra of DNA dissolved in PBS and IL, the vibrational contribution of IL was subtracted from the total spectrum, after appropriate normalization to the intensity of the Raman signals at 1021, 1060 and 1211 cm^{-1} and assigned to the vibrational modes of [BMIM]$MeSO_4$. The choice of the intensity of these three peaks as internal standards for the normalization procedure was justified by the absence of Raman vibrational features associated with DNA in this spectral region.

Circular dichroism Spectroscopy

Circular dichroism (CD) spectra were recorded using Jasco J-710 polarimeter equipped with a thermal bath. All samples were measured from 305 to 368 K in a temperature-controlled quartz cell of 1 mm path-length. Each CD spectrum was averaged over 10 scans recorded in the range from 220 to 320 nm, at a scanning speed of 100 nm/min and 1nm of bandwidth. Measurements were performed under a constant nitrogen flow, which was used to purge the ozone generated by the light source of the instrument.

UV/Vis Spectroscopy

UV absorption measurements were recorded with a PerkinElmer, model Lambda 25 UV/Vis spectrometer at double beam equipped with a Peltier

thermostattable. All samples were measured from 305 to 370 K in a rectangular quartz cell of 10mm path-length. The spectra were recorded in the range from 190 to 600 nm at a scanning speed of 120 nm/min and 1 nm of bandwidth.

5.4.2 Results and discussion

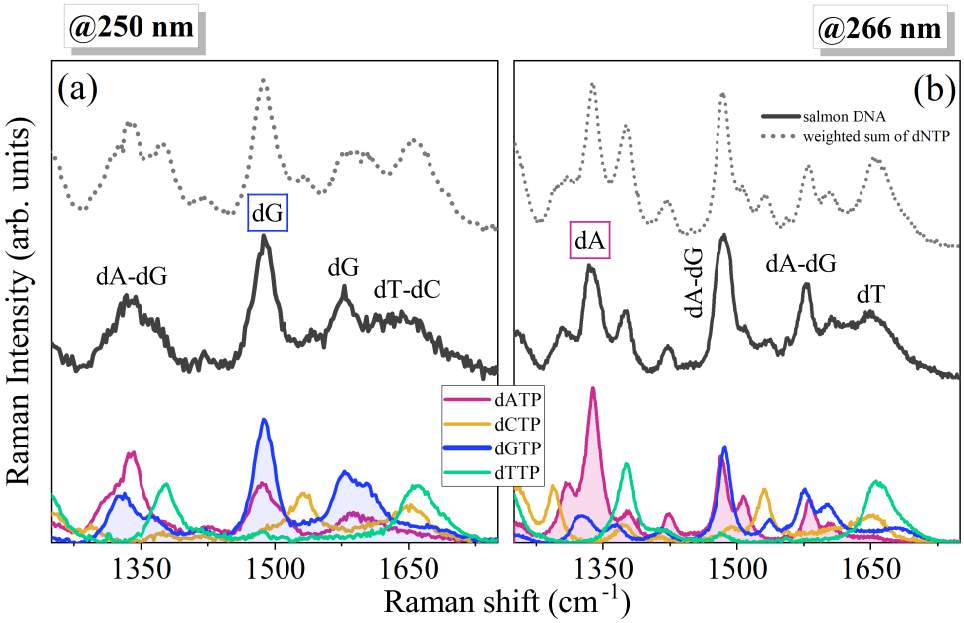

Figure 5.8: UVRR spectra of deoxynucleotides dNTP and salmon DNA excited at (a) 250 nm and (b) 266 nm. The profiles obtained as linear combination of the individual experimental spectra of dNTP are reported in the same graphs for comparison with experimental spectra of DNA.

In Fig.5.8 is shown the UVRR spectra of deoxynucleotides dNTP and DNA excited at 250 and 266 nm. The profile of dNTP were arbitrarily normalized on the total intensity of the spectra. The comparison between the experimental profile of DNA and different nucleotides allows to attribute very in detail the main vibrational features in the spectra of DNA to single dNTP at the two selected exciting wavelenghts. In the same graphs of Fig.5.8 (a) and (b) are reported also the profiles obtained as the weighted sum of normalized spectra of dNTP (41.2% G-C + 58.8% A-T). The good accordance found between the ex-

perimental UVRR spectra of DNA and the weighted sum of dNTP confirms the reliability of the normalization procedure. The slight differences between the two curves can be probably attributed to the different conformation assumed by sugar-phosphate skeleton in DNA strand with respect to pure dNTP and to the stacking interactions among bases in the duplex helix structure [171],

Fig.5.8(a) shows that in the UVRR spectrum of DNA excited at 250 nm the band at $\sim 1335\ cm^{-1}$ (labeled as band I-dA) contains contributions arising both from dG and dA. Conversely, in the spectrum excited at 266 nm (Fig.5.8 2(b)) the same spectral feature at $\sim 1335\ cm^{-1}$ is mainly attributable to vibration mode localized on dA residue, namely the coupled stretching vibrations N7=C8 and C5-N7 [144] as reported in Tab.5.1. Looking at the peak centered at $\sim 1485\ cm^{-1}$ in Fig.5.8 and labeled as band II-dG, it is noteworthy that for this band the contribution arising from dA and dG are comparable in the UVRR profile of DNA excited at 266 nm. On the contrary, the excitation wavelength at 250 nm emphasizes the contribution of dG residue to the vibrational peak centered at $\sim 1485\ cm^{-1}$, and due to a combination of the bending motion of C8-H and the stretching movement of C8=N7 and N9-C8. The mode has been assigned to a combination of bending motion of C8-H and stretching movement of C8=N7 and N9-C8 [144] (see Tab.5.1). This can be explained with the proximity of the excitation energy to the 255-nm transition of dG that largely involves the N7=C8 double bond of the imidazole ring [141]. The choice of 250 nm as excitation wavelength gives the opportunity to be more sensitive for the band at $\sim 1485\ cm^{-1}$ to the dG contribution with respect to dA one.

Fig.5.9 shows the temperature-evolution of Raman profiles collected for DNA and DNA+[BMIM]$MeSO_4$ in the wavenumber range 1300-1800 cm^{-1} at 250 and 266 nm as excitation wavelengths. In order to extract quantitative information on the temperature behaviour of the two selected vibrational bands I-dA and II-dG, a spectral decomposition of the experimental UVRR profiles has been implemented. An example of best-fitting procedure for the spectra collected at 305 K is reported in Fig.5.9 for the wavenumber range of interest.

Fig.5.10 (a) and (b) show the temperature-dependence of the UVRR intensity for the bands II-dG and I-dA, respectively. As concerning the first band (Fig.5.10(a)), the trend exhibits a sharp increasing in the correspondence to

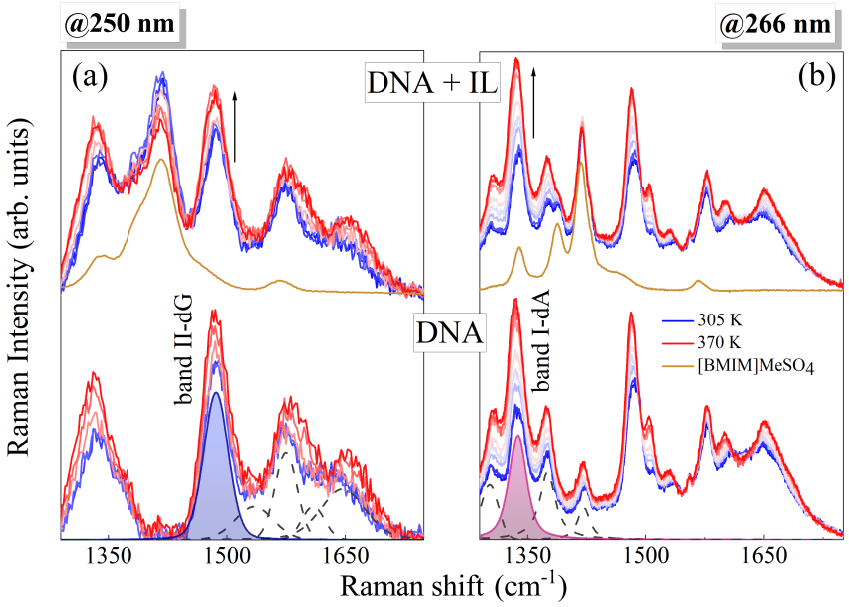

Figure 5.9: Temperature-evolution of UVRR spectra of DNA in the absence (bottom) and the presence (top) of [BMIM]$MeSO_4$ excited at (a) 250 nm and (b) 266 nm from 305 to 370 K. The brown lines represent the UVRR spectra of IL. Representative partial fitting procedures are required on the bottom.

about 355 K. As explained in the previous section, such characteristic behaviour has been associated to the melting transition of DNA that involves the full denaturation of the double-stranded structure. Therefore, the plot in Fig.5.10(a) suggests that the band II-dG is mainly sensitive to the stacking interactions involving dG residues. In particular, the finding of a sharp transition near the melting temperature of DNA is consistent with the cooperative character of the unstaking of guanines, promoted by the increasing of thermal motions, that mainly contributes to the temperature-dependence of band II-dG. Interestingly, the inspection of Fig.5.10 (b) points out a smoother increasing as a function of temperature for the intensity of band I-dA. This suggests that this mode detects also pre-melting processes in which the double-stranded structure of DNA is perturbed but not completely disrupted as occurs during the thermal denaturation. Since the band I-dA is mainly localized on C5-N7=C8 bond of adenine where N7 atom is able to form H-bond with the solvent molecules [149], it is reasonably to suppose that the intensity of this

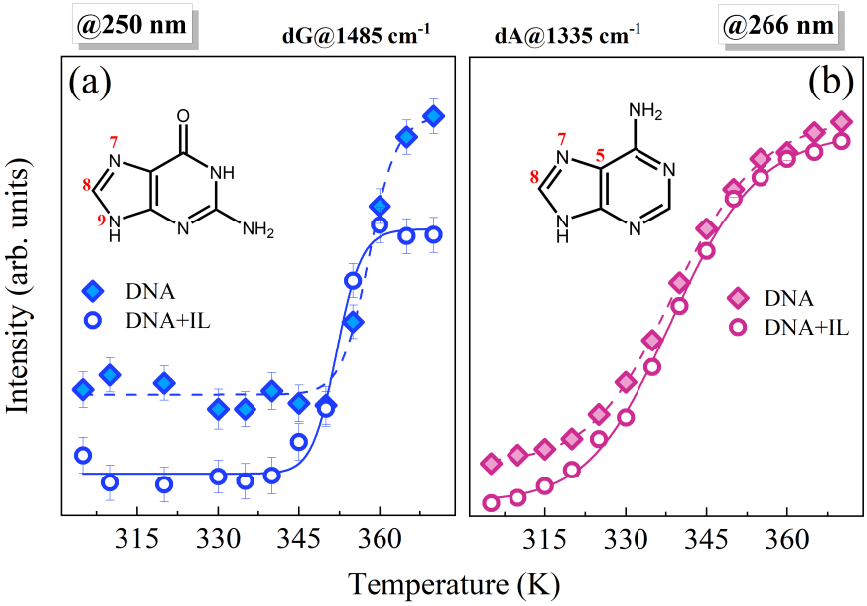

Figure 5.10: Temperature-dependence of the intensity of the vibrational modes assigned to (a) ν(C8=N7) + ν(N9-C8) + δ(C8H) of guanine at 250 nm and (b) ν(C8=N7) + ν(C5-N7) of adenine at 266 nm for DNA in absence (full rhombs) and presence of [BMIM]$MeSO_4$(empty circles).

vibration is sensitive to localized non-cooperative processes that occur before the DNA melting. At variance with DNA melting, pre-melting transitions reflect temperature-dependent conformational changes of small regions of the DNA molecule. dA vibrational modes can sample these changes quite effectively, as A-T base-pair opening occurs much more frequently than in the case of C-G base-pair [177]. In fact, this is also consistent with theoretical calculations [178] that find an average value for H-bond lifetime on N7 site of dA that is shorter with respect to the H-bond involving N7 of dG. This result can explain the major sensitivity exhibited by the band I-dA (Fig.5.10 (b)) to molecular rearrangements of DNA structure occurring in the pre-melting region and associated with adenine-water H-bond breaking. All the findings corroborate the potentiality of synchrotron-based UVRR technique to provide molecular insights on the different cooperative and non-cooperative processes, involving dA and dG residues, that compete to lead to the complex phenomenon of thermal denaturation of DNA. Quite interestingly Fig.fg:4:draftBR (a) and (b)

shows that in the spectra of DNA+[BMIM]$MeSO_4$ the intensity of band II-dG and, to a less extent I-dA, are smaller than those measured in pure DNA. The effect persists over the entire temperature range that we have explored. This hypochromic effect suggests that the addition of [BMIM]$MeSO_4$ tends to favor the formation of a more compact structure in DNA double-stranded [145]. Moreover, the persistence of hypochromicity also after the unfolding of DNA, as particularly evident for band II-dG (Fig.5.10 (a)), gives indication that the base-stacking of guanines is quite effective for DNA in the presence of [BMIM]$MeSO_4$. More interestingly, the promotion by IL of hypochromic with respect to hyperchromic effect confirms that [BMIM]$MeSO_4$ tends to interact with DNA nucleotides through groove binding and not trough intercalation mechanism [145].

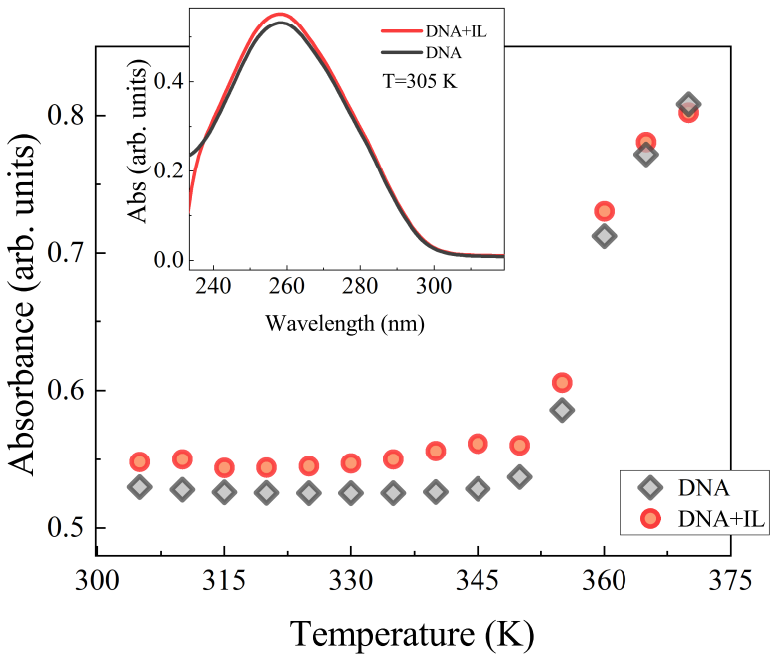

Figure 5.11: Trend of the absorption at 260 nm in absence (grey) and presence of [BMIM]$MeSO_4$ (red) as a function of the temperature. Inset: Comparison between UV-VIS absorption spectra of DNA and DNA+[BMIM]$MeSO_4$ recovered at 305 K.

In order to complete the UVRR data, UV absorption measurements on solution of DNA pure and in the presence of [BMIM]$MeSO_4$ have been per-

formed. Fig.5.11 shows the temperature evolution of the maximum of the intensity of absorption curve at $\sim$ 260 nm for DNA with and without the addition of IL. Since the absorption profile of pure [BMIM]$MeSO_4$ in practically negligible up to $\sim$ 240 nm, the data reported in Fig.5.11 take account only of the contribution arising from DNA. As first remark, a sharp transition in the absorption intensity can be detected in correspondence of 355-360 K for both the set of data, in the presence and absence of IL. This rapid increase of the UV absorption is a marker of the occurring of DNA melting, in agreement with what reported in literature [150] . The coincidence between the melting temperature detected by UVRR and UV absorption techniques further confirms the interpretation of Raman spectrocopic data discussed above.

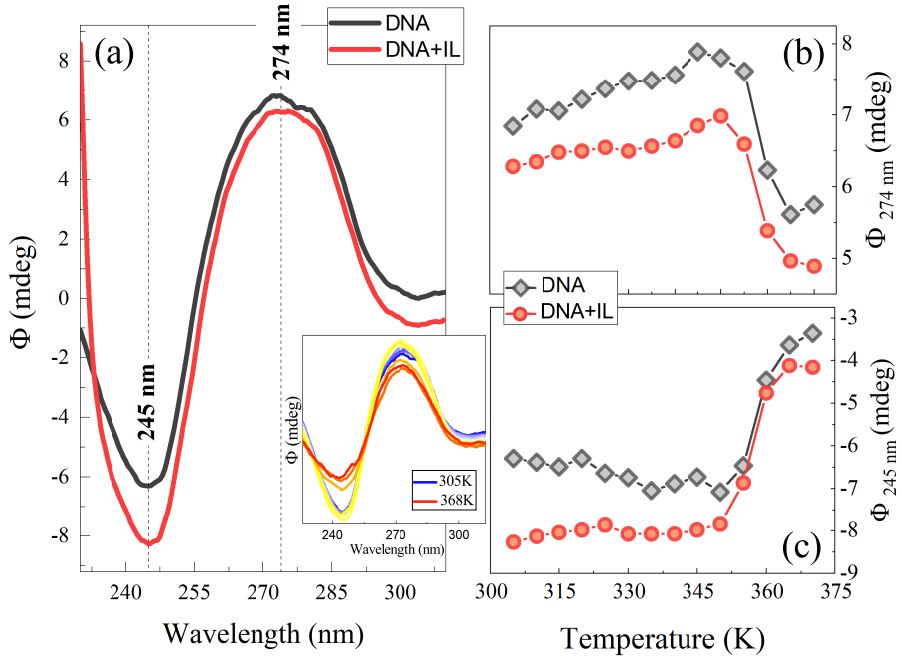

Figure 5.12: (a) Comparison between CD spectra of DNA in absence (grey) and presence of [BMIM]$MeSO_4$ (red) recovered at 305K. Temperature-dependence of ellipticity (b) at 274 nm and (c) at 245 nm for DNA in presence and absence of IL. Inset: Representative temperature-evolution of CD spectra of DNA in absence of IL.

By using CD technique, we can probe the temperature-dependent changes of geometry for DNA pure and in the presence of [BMIM]$MeSO_4$ trough the analysis of spectral modifications of CD spectra [179]. Fig.5.12 (a) shows a

comparison between the CD spectra of DNA in absence and presence of IL collected at 305 K. Since [BMIM]$MeSO_4$ is achiral molecule, it does not exhibit any interfering CD band in the spectra of DNA+IL. As shown in Fig.5.12(a), the CD signal of pure DNA exhibits the classical features of double-stranded B-form DNA consisting of a positive band β around 274 nm and a negative peak α at 245 nm with a crossover at the absorption maximum. The positive feature is due to π-π base stacking while the negative band corresponds to the polynucleotide helicity. The comparison between the two curves in Fig.5.12 (a) evidences that the CD spectra of DNA in presence and in absence of IL have a similar shape, thus suggesting that the native B-conformation of DNA is preserved also after the addition of [BMIM]$MeSO_4$. On the other hand, the presence of [BMIM]$MeSO_4$ induces a slight decrease in the positive band at about 274 nm of DNA that is consisten with an alteration in the base packing, probably due to the hydrophobic interaction between the hydrocarbon chains$[BMIM]^+$ and the bases of DNA [169]. It is also to noteworthy a significant decrease in the molar ellipticity that change from -6.3 to -8.3 where the IL is added to DNA. Such behavior reflects the distortion in the helical structure of B-DNA and could be related to a transition from an extended double helix to a more compact form, known as Ψ structure, which is due to the electrostatic interaction between the cationic groups of IL and the phosphate groups of DNA. The absence in the CD spectra of DNA+[BMIM]$MeSO_4$ of the typical signals associated to intercalation phenomena (magnitude of positive and negative bands) confirms the UVRR spectroscopy results indicating that IL does not act as an intercalator in DNA structure [180]. On the basis of the results reported in Fig.5.12 (a), we can speculate that [BMIM]$MeSO_4$ binds to DNA bases through groove binding and hydrophobic interactions, as found for the cases of [BMIM]Cl [166] and [BBIM]Br [167], while [BMIM]PF_6 [181] and guanidinium-IL [182] are able to intercalate with the bases of duplex DNA. The influence of temperature on CD spectra of pure DNA can be observed in the Inset of (a). In correspondence of the temperature of 360K, the CD spectrum clearly exhibits the characteristic shape associated to denatured DNA [183]. A decreasing in magnitudes of both the positive and negative bands is found in the CD spectra of pure DNA as the temperature increases. This is consistent with the occurrence of unstacking on the bases that leads to a general weaken-

	DNA in Tris		DNA in [BMIM]Cl	
DNA/IL	1/0 (w/w)	1/22 (w/w)	1/44(w/w)	1/87(w/w)
Preparation	250μL of DNA stock sol. 750μl of Tris	250μL of DNA stock sol. 745μl of Tris 5μL of [BMIM]Cl	250μL of DNA stock sol. 740μl of Tris 10μL of [BMIM]Cl	250μL of DNA stock sol. 730μl of Tris 20μL of [BMIM]Cl

Table 5.3: Description of DNA/IL samples preparation.

ing of the interaction between neighboring bases and a decrease in helicity of DNA. This finding further confirms the interpretation of UVRR data discussed above. The dependence on temperature of the β intensity for DNA in presence and absence of IL is illustrated in (b). At lower temperatures (305-350K), the ellipticity increases and this behavior suggests that B→C conformational changes of DNA take place in the premelting region [183]. For temperature values ≥350K, we observed an opposite trend in the ellipticity, probably due to the beginning of denaturation process. Fig.5.12 (c) shows the temperature evolution of α band. As mentioned above, modifications occurring in ellipticity in such wavelength region can be associated to changes in helicity, which are characteristic for the right-handed B form of DNA. The sigmoidal shape of (c) strictly resembles that obtained for the UV-Vis absorbance (see Fig.5.11).

5.4.3 Effect of IL concentration

With the aim to better characterize the groove binding mechanism of ILs with DNA, the thermal stability of DNA dissolved in [BMIM]Cl/water solutions has been investigated as a function of concentration of IL [184]. The choice to use as co-solvent of the ionic liquid [BMIM]Cl a TRIS buffer rather then PBS, is due to the purpuse to reduce the type of anion species present in solution. A detailed description of DNA/IL samples preparation is reported in Tab.5.3.

Fig.5.13 displays the variation in intensity undergone by band II-dG as a function of the increasing concentration of [BMIM]Cl at three representative temperature. In order to extract more quantitative parameters that account the effect of IL concentration on the intensity of band II-dG, a decomposition procedure of the spectra has been performed. An example of best-fitting procedure for the spectrum of DNA/IL = 1/87 (w/w) collected at 310 K is reported in Fig.5.13 for the wavenumber range of interest.

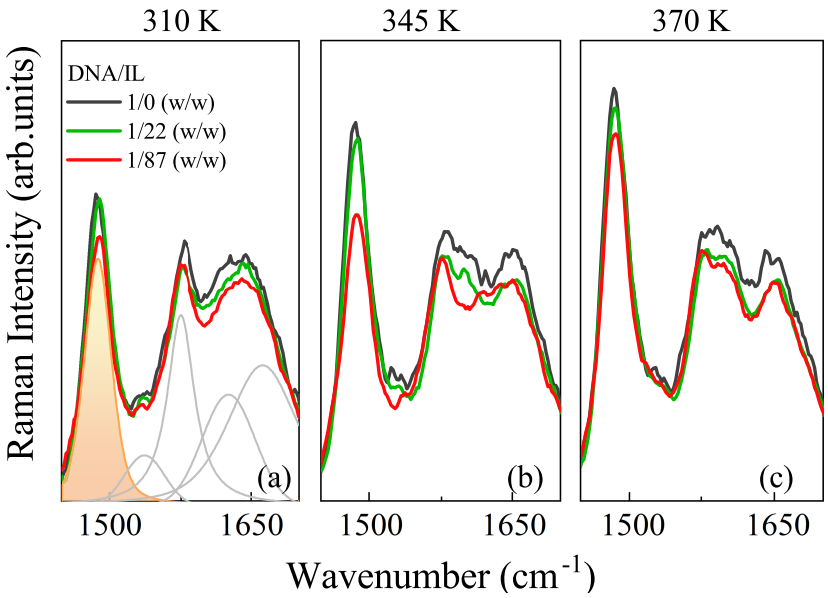

Figure 5.13: Comparison between the 250 nm-excited Raman spectra of DNA/IL as function of concentration of [BMIM]Cl at T=310 K (a), 345 (b) and 370 K (c), in the wavenumber range 1450-1700 cm^{-1}. Representative fitting procedure is reported.

Fig.5.14 shows the temperature-dependence of the UVRR intensity of the band II-dG for pristine DNA and at different percentages of [BMIM]Cl. As common feature to all the trends, it can be observed a sharp upturn for the intensity of the band II-dG in correspondence of $\approx$ 340-350 K, highlighting different melting temperatures for the proposed samples. By inspection of Fig.5.14, it is possible to observe that the intensities of band II-dG for the spectra of DNA in presence of IL are less intense with respect to those measured in pure DNA over the whole investigated temperature range. This hypochromic effect suggests that the addition of [BMIM]Cl tends to favor the formation of a more compact structure in DNA double-stranded [145]. Moreover, the persistence of hypochromicity also after the unfolding of DNA gives indication that the base-stacking of guanines is quite effective for DNA in the presence of [BMIM]Cl. The plots in Fig.5.14 point out also a slight increment of the melting temperature observed for DNA as a consequence of the progressive addition of IL. In order to extract quantitative information, the intensity $I(T)$ of the band II-dG can be properly described by a two state model [172] following the Eq:

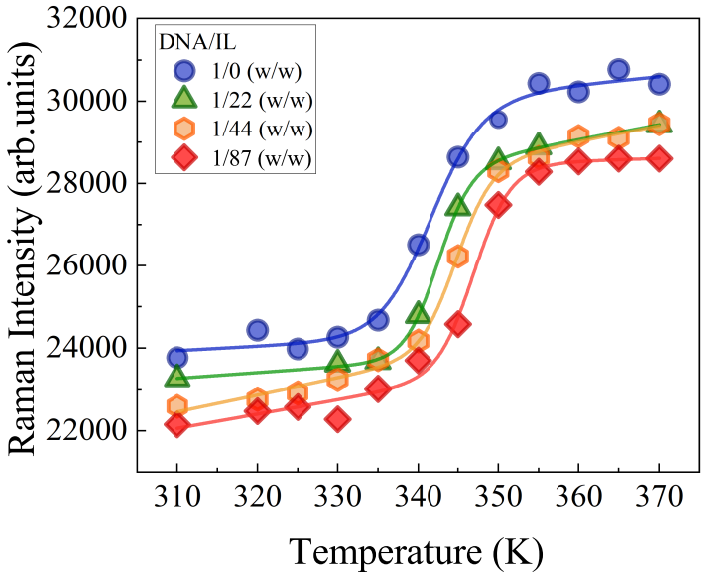

Figure 5.14: Temperature-dependence of the Raman intensity of the band II-dG for DNA/IL (w/w) = 1/0 (blue circles), 1/22 (green triangles), 1/44 (orange hexagons), 1/87 (red rhombs). Continuous lines are fitting of the experimental data by using Eq.5.1, see details in the text.

$$I(T) = \frac{I_N + m_n \cdot T + (I_D + m_D \cdot T)K_T}{1 + K_T} \tag{5.1}$$

where K_T signifies the equilibrium constant between native and denaturated states, I_N and I_D represent the intensities corresponding to the native and denaturated state of DNA, respectively. In the equation above, the parameters m_N and m_D describe the linear temperature-dependence of the band intensity in the pre and post-melting regions, respectively. Finally, the equilibrium constants in the native and denaturated states can be expressed as:

$$K_T = exp\left[\frac{\Delta H_m}{R}\left(\frac{1}{T_m} - \frac{1}{T}\right)\right] \tag{5.2}$$

where R is the gas constant and ΔH_m and T_m are the enthalpy variation and the temperature associated to the melting process. As visible in Fig.5.14, the temperature-dependence of the band II-dG is satisfactorily reproduced by using Eq.5.1. The fitting procedure of plots in Fig.5.14 provides the estimation

DNA/IL	**T_m (K)**	**ΔH_m (kJ/mol)**
1/0 w/w	341.6 ± 0.5	3025.1 ± 736.4
1/22 w/w	342.5 ± 0.5	4640.1 ± 288.7
1/44 w/w	344.8 ± 0.5	4380.6 ± 849.3
1/87 w/w	347.3 ± 0.5	5096.2 ± 673.6

Table 5.4: Thermodynamic parameters extracted by fitting the experimental data of Fig.5.14 with Eq.5.1 (see text for details) .

of the parameters ΔH_m and T_m , as summarized in Tab.5.4.

The values reported in Tab.5.4 confirm the slight increment of the melting temperature induced by the increasing concentration of [BMIM]Cl, as already discussed above. This may be consistent with the results of theoretical investigations [166, 167] suggesting that the cations of IL tend to majorly interact with the DNA backbone when the negative charges of phosphate groups are localized. This implies that the cations are able to stabilize the DNA structure by reducing charge repulsion between the phosphate groups on each of the DNA strands [173]. This stabilization effect is probably accompanied by the establishment of H-bond interactions between the CH groups of IL [166] and the acceptor/donor sites present on the major and minor grooves of DNA. Overall these effects result in an enhancement of the stability of DNA native conformation also at higher temperature, promoted by the presence of IL. The presence of IL induces an increase of ΔH_m value with respect to the case of DNA/IL = 1/0 (w/w). This result is in analogue with other investigation on melting parameter of DNA with divalent metal cations [173].

Beside the intensity change, Fig.5.14 points out also a slight red-shift for the band II-dG upon the increasing of thermal motion. Fig.5.15 reports the wavenumber positions of band II-dG found for pristine DNA and DNA+IL. Due to the normal composition of band II-dG, the frequency of this Raman peak is sensitive to the interactions between the solvent molecules and the N7 site of guanine that can act as acceptor of H-bond [174, 175] . The shift of the band II-dG to lower frequency with the thermal denaturation has been attributed to a reinforcement of H- bond formed by guanine with the solvent [149]. This phenomenon can be can be attributed to a major exposure of N7

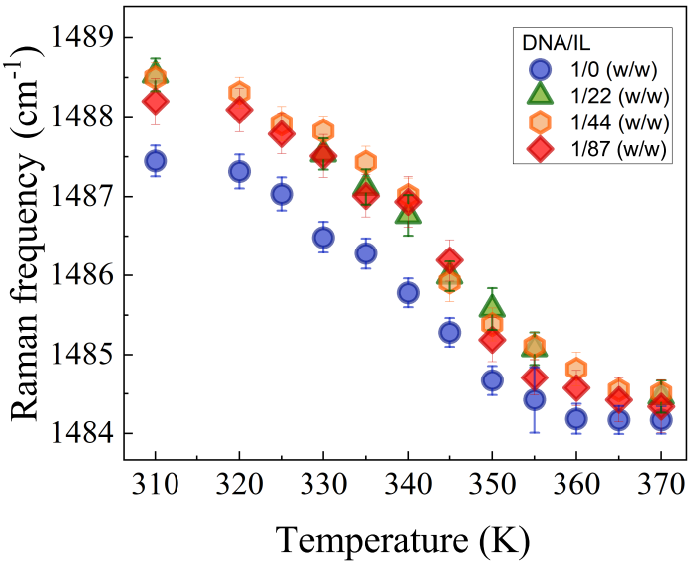

Figure 5.15: Temperature dependence of wavenumber position for the band II-dG for pristine DNA and DNA+IL DNA/IL (w/w) = 1/0 (blue circles), 1/22 (green triangles), 1/44 (orange hexagons), 1/87 (red rhombs).

site in denaturated DNA to solvent molecules. By the inspection of Fig.5.15, we note that before the DNA thermal denaturation the presence of IL induces a slight blue-shift in the position of band II-dG with respect to the case of pristine DNA. This result can be likewise explained by considering two effects: i) the formation of H-bond interaction on N7 atom with CH groups of [BMIM]Cl [166] and ii) the reduction of H-bond interaction between buffer solvent molecules and N7 site due to the presence of cations of IL [176] . Since it is well-known the capacity of cations of IL to penetrate the "cone of hydration" of water molecules around the charged phosphate groups of DNA [167] , the diffusion of water across the nucleobases in DNA is hampered by the presence of IL. This is consistent with the slight blue-shift of band II-dG observed in the samples of DNA+IL with respect to pure DNA before the melting temperature. The disappearing of this effect at high temperatures (see Fig.5.15) is probably due to the alteration of DNA structure caused by the melting process.

5.4.4 Effect of alkyl-chain length

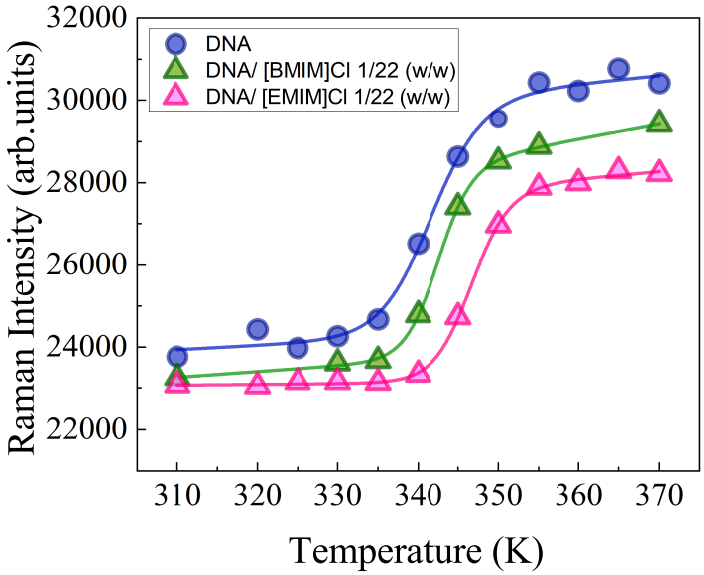

Figure 5.16: Temperature-dependence of the Raman intensity of the band II-dG for DNA/IL (w/w) = 1/0 (blue circles) and DNA in presence of [BMIM]Cl (green triangles) and [EMIM]Cl (pink triangles) at DNA/IL (w/w)=1/22. Continuous lines are fitting of the experimental data by using Eq.5.1.

Preliminary investigations have been conducted to identify the role played by alkyl-chain length of cation core on the thermal stability of DNA. Fig.5.16 dislays the temperature-dependence of the UVRR intensity of the band II-dG for pristine DNA and in presence of [BMIM]Cl and [EMIM]Cl at the same w/w. A slight increment of the melting temperature is observed for DNA in presence of the shorter alkyl-chain lenght. Also the hypochromic effect, already observed in presence of IL, is emphasized by 1-ethyl-3-methylimidazolium based-IL. Recent experimental and simulation results indicate that the lengthening of the alkyl chain induce a charge delocalization in the cation [188–191]. For our systems, such charge delocalization leads to a weaking of electrostatic interaction between DNA backbones – $[BMIM]^+$ with respect to the case of $[EMIM]^+$.

In summary, the choice of 250 nm as excitation wavelength gives the possibility to selectively enhance the vibrational signals associated to aromatic

ring of guanine residues, then simplifying the complex off-resonance Raman spectra of DNA. The experimental data suggest that the thermal stability of DNA in IL is related at molecular level by two mechanisms: i) the unstacking of guanine bases and ii) the intermolecular interactions involving the N7 site of guanine. As main result, the thermal stability of DNA is found to increase as function of concentration of [BMIM]Cl in the investigated DNA/IL ratio range and decrease as function of alkyl-chain length.

Chapter 6

Hydrophobic/hydrophilic effects in the dynamics of hydration water as probed of UV Raman scattering

In this chapter we report some results of complementary studies aimed to test the capability of UVRR spectroscopy to investigate the hydrogen-bond dynamics of hydration water in different environments. For this reason, we have considered two paradigmatic systems, i.e i) cyclodextrins that are hydrophilic sugare solutes that can be fully hydrated by water and ii) polysaccharide hydrogels that can retain large amount of water inside their network structure. The investigation of these systems has provided usefull suggestions for the development and implementation of SR-UVRR spectroscopy experiments performed on IL/water solutions and on the analysis of the solvation effects of these solvents on biological molecules.

6.1 Water structure in aqueous solutions of native and modified cyclodextrins

Hydration water plays an important role as driving mechanism of a wide variety of physical and biological processes in soft matter. A large variety of solutes, including sugars, amino acids, methylamines, and lyotropic salts, strongly influence the stability, dynamics and function of matter, such as protein folding mechanism and membrane stability. On the other hand, the influence of solute on water structure has been related to rearrangement of water molecules and there is particularly interest in understanding how different hydrated molecules perturb water dynamics [192]. Carbohydrates represent one of the most interesting type of sugars because of their capability to form H-bond. Their structure is formed by hydrophobic and hydrophilic groups also present in nucleic acids and proteins, so they are used as very simple model to investigate water properties surrounding biological macromolecules. The high concentration of hydroxyl groups allows to study the effects induced by a hydrophilic interface on the water behaviour [193, 194]. Moreover, the homogeneous distribution of OH groups in small sugars leads to the formation of HB solute-water comparable to HB between pure water molecules. Previous works demonstrate that sugars cause slight variations on the organization of HB network of bulk water [195, 196]. These results have stimulated a renewed interest in dynamics of water–sugar systems, as function of solute concentration. Walrafen [197] observed that sucrose in concentrated solutions exhibits a "structure marke" effect (solute inducing a change similar to a decrease of temperature). Conversely Neal and Goring noted for low sucrose concentration a "structure-breaker' effect (behaviour similar to an increase in temperature). Cyclodextrins (CDs) can be used as a model system to achieve a comprehensive view of the mechanism which drive the solvation dynamics in macromolecules, as suggested by different authors [198, 199]. They are natural cyclic oligosaccharides consisting of 6 (α-CD), 7 (β-CD), or 9 (γ-CD) glucopyra-nose units [200]. In water, CDs assume the characteristic shape of a truncated cone with a central cavity formed by the annular structure. Hydroxyl groups are located on the edge of both rims of the conical structure, giving a hydrophilic

character to the outer surface of the molecule and making CD soluble in water. The inside of the cavity, on the contrary, has a hydrophobic character, as it is formed by the skeletal carbons and ether-like oxygens of the glucose residues. Thanks to this structure, CD in water behaves as a molecular host able to form inclusion complexes with a large variety of poorly water-soluble guest compounds [201], significantly modifying and/or improving the physicochemical and biological properties of the encapsulated guest molecule. CDs find application in all the fields of industry [202], especially in the cosmetic, environmental science, food [203], and pharmaceutical sectors [204, 205]. Despite of a large number of studies devoted to explain the ability of CDs to form inclusion complexes, a detailed description of the complexation mechanism still needs to be achieved [202]. A general agreement is present in literature on the key role played by water in this process [201, 206, 207], yet a molecular level description of the interactions between the macrocycle and water remains incomplete [208]. A strong limitation in the use of β-CD is due to its low solubility in water compared with that of other native α-and γ-CDs, and many studies suggest the existence of correlations between this anomalous behavior and how these compounds affect the molecular organization of surrounding water molecules [209–214]. In particular, some molecular dynamics simulations point out a relatively larger increase of the local structure (i.e., higher density) and a corresponding slower mobility of water around β-CD [209,210,212–214,223]. A destructuring effect on the tetrahedral order of hydration water has also been evidenced, especially for those water molecules localized inside the hydrophobic cavity [211]. It is expected that the substitution of primary and secondary hydroxyls groups in the ring of native CDs with other desired functionalities [215] will affect their H-bonding capability, leading to modified CDs with increased solubility. The growing interest in the investigation of the molecular properties of chemically modified CDs in aqueous media lies in the wide commercial importance of some derivatives, such as hydroxypropyl-β-cyclodextrin (HP-β-CD) and sulfobutyl ether-β-cyclodextrin (SBE-β-CD), used in industrial applications, particularly in drug formulation, cosmetics, and toiletry industries. Besides a significant improvement in water solubility, several types of chemically modified β-CDs also exhibit a lower nephrotoxicity, thus allowing to overcome some restrictions on their pharma-

ceutical use [216]. Recent molecular dynamics simulations suggest that substitution in CDs of hydroxyl groups with hydroxylpropyl ones causes significant disruption of the water structure depending on both the number and type of substituted OH groups [217]. Dielectric relaxation measurements indicate an increase of the number of water molecules in the CD hydration shell (i.e., the average hydration number per glucopyranose ring) with the extent of substitution [218]. Recently, some of us have used depolarized light-scattering experiments to study the structural and dynamical properties of CD water solutions in the 50-150 mg/ml concentration range [219, 220]. The effect of CDs on the H-bond water structure has been investigated by analyzing the behavior of intermolecular modes of water, detected in the low-frequency Raman spectrum and sensitive to the local order of solvent molecules in the hydration shell. The data show a partial loss of tetrahedral order compared with bulk water, by increasing both temperature and CD concentration [220]. Concerning the dynamical properties, the analysis of frequency extended depolarized spectra has allowed to distinguish the relaxation process at the picosecond timescale associated to the rearrangement of the H-bond network of water in the CD hydration shell, which is found to be 7 to 8 times slower than the relaxation process of bulk water [219]. All these experimental findings are consistent with the results of molecular dynamics simulations on CD aqueous solutions reported in literature [221–224]. Very recently, strong effort has been employed in UV Raman and Fourie-transform infrared spectroscopies attenuated total reflection spectroscopy to provide an explanation at the molecular level of the improved performance as carrier agent of the popular modified cyclodextrin SBE-β-CD [225]. The analysis of the OH stretching region in the high-frequency Raman and IR spectra of aqueous solutions shows that the tetrahedral order of water is partially lost in the hydration shell of the macrocycle. Venuti et al. [225] also demonstrate that OH stretching signal can provide direct information on the structural changes induced by CDs on H-bond network of water, as already observed by other authors in sugar-water solutions [73, 226, 227]. Starting from these results, in the present work, we aim to extend our previous structural and dynamical investigations [219, 225], by performing a comparative study of the hydration properties of native and chemically modified CDs by using UV Raman spectroscopy experiments [74].

6.1.1 Experimental methods

Sample preparation

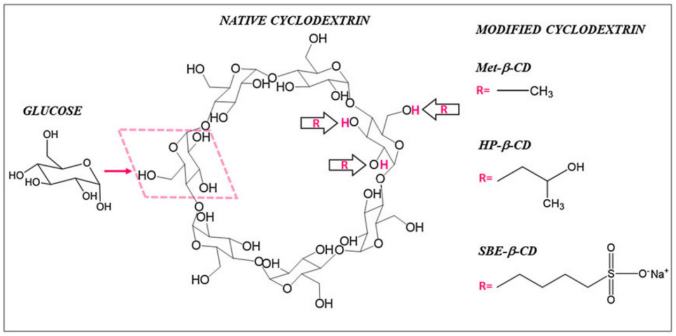

Figure 6.1: Schematic structure of glucose, native cyclodextrin (CD), and substituted chain of modified cyclodextrin.

α-CD, HP-β-CD, methyl-β-cyclodextrin (Met-β-CD), and glucose were purchased from Sigma-Aldrich and SBE-β-CD from CyDex Pharmaceutical. The chemical structures of glucose, native, and modified CDs are reported in Fig.6.1. All chemicals were used without any further purification. Aqueous solutions were prepared by dissolving the sugars in the right amount of double-distilled and deionized water to obtain the desired sugar concentration (hereinafter expressed in mg/ml, i.e., mg of solute per ml of water). All samples were freshly prepared into UV-grade quartz cells and daily used in UV Raman spectroscopy experiments. Tab.6.1 summarizes the main characteristics of the different types of CD used in this study. For the chemically modified forms of CD (HP-β-CD, Met-β-CD, and SBE-β-CD), the degree of substitution, that is, the average number per β-CD molecule of hydroxyl groups replaced by the substituent group R, is indicated. All the investigated samples have been prepared below the saturation threshold (see values reported in Tab.6.1) by checking that the solutions were limpid.

UV Raman spectroscopy measurements

UVRR spectroscopy experiments were carried out using the setup described in detail in Chapter 2. The Raman spectra were collected at 266nm. The use of UV wavelengths for exciting the Raman spectra strongly reduces

CD	M_W	R	Substition degree per β-CD molecule	Solubility (g/l) in water (25° C)
Glucose	180.16	//	//	909
α-CD	972.84	//	//	145
SBE-β-CD	2163	$(CH_2)_4SO_3Na$	6.6	>1000
Met-β-CD	1310	CH_3	11.2-12.6	>500
HP-β-CD	1375	$CH_2CHOHCH_3$	4.2	>600

Table 6.1: Molecular weight (M_W), type of substituent chemical group (R), degree of substitution per β-CD molecule, and solubility in water; // = it is used to indicate missing value.

the interfering fluorescence background typically affecting the visible Raman spectra of CD-water solutions. The samples were investigated at different temperatures, in the range from 280 to 370 K.

6.1.2 Results and Discussion

Concentration effects on the H-bond network of water

Fig.6.2a shows the Raman spectra collected at room temperature in the wavenumber range 2600-4200 cm^{-1} for aqueous solutions of SBE-β-CD at different concentrations, together with the spectrum of pure water, acquired in the same experimental conditions. To investigate the supramolecular organization of water, the attention is focused on the OH stretching band (3000-3800 cm^{-1}), which represents a good probe of the intermolecular structure of the H-bond network. The Raman profile of pure water clearly shows the presence of three distinct features at $\omega_1 \approx 3200$; $\omega_2 \approx 3450$; and $\omega_3 \approx 3600$ cm^{-1}. The first component is representative of the so-called "connective water" in which the OH oscillators are phase correlated with oscillators of nearest molecules. This vibration is originated by "ice-like" tetrahedral water arrangements [228, 229]. The intermediate contribution is assigned to "closed" water structures, where H-bonds are partially distorted and the phase correlation to vibrations of nearest OH groups is lost [230, 231]. The higher wavenumber shoulder is associated to OH groups weakly stabilized by H-bond interactions. These groups can be considered as transient species formed during the H-bond reorganization of the

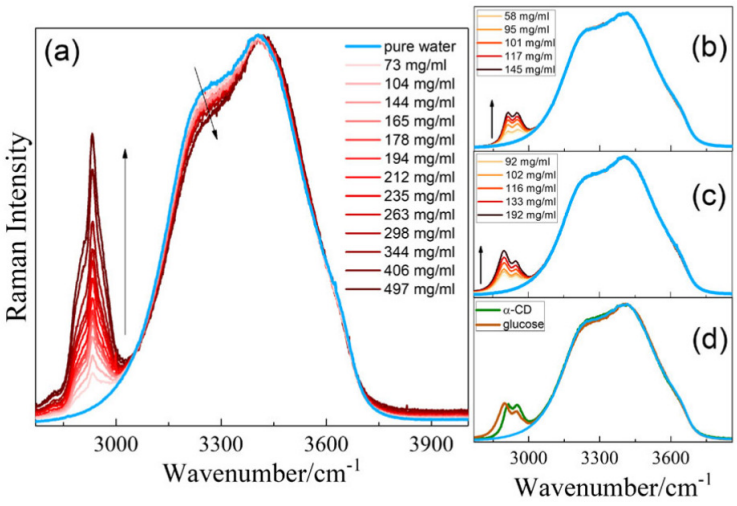

Figure 6.2: Concentration dependence of polarized Raman intensity I_{VV} for pure water (light blue line) and (a) sulfobutylether-β-cyclodextrin, (b) α-CD, and (c) glucose aqueous solutions at 298 K in the spectral range 2600-4200 cm^{-1}. The spectra are normalized to their maximum intensity. The arrows indicate increasing solute concentration. (d) Comparison between spectra of pure water and aqueous solutions of α-CD (145 mg/ml) and glucose (133 mg/ml).

network [232]. Fig.6.2a indicates that the increase of SBE-β-CD concentration causes a progressive decrease of the component at 3200 cm^{-1}, suggesting that solute leads to a reduction of the population of ordered tetrahedral structures, even at low concentration ("destructuring effect"). In contrast, the band profiles obtained for aqueous solutions of α-CD (Fig.6.2b) and glucose (Fig.6.2c) retrace very well the OH stretching band of pure water, indicating that in these cases, the distribution of water structures is not significantly perturbed upon addition of solute. In Fig.6.2d a comparison is shown between the spectra of α-CD and glucose solutions at similar concentrations. Only a minor reduction of the ice-like component can be observed in the case of glucose, in line with previous results [73], whereas the OH profile almost exactly coincides with that of pure water for the α-CD solution. This suggests that the effect induced on the water environment by α-CD is essentially related to the solvent-exposed hydrophilic surface, in which the distribution of OH groups is comparable to that of its monomeric constituent. To gain quantitative information on the H-bond molecular organization, a fit procedure based

on the use of three components has been carried out to reproduce the OH stretching band [233–235]. One mixed 50% Gaussian-50% Lorentzian and two Gaussian profiles have been used, respectively, for the lower wavenumber component (associated to tetrahedrally coordinated water molecules) and the two higher wavenumber components (associated to molecules involved in distorted H-bonds and to free OH oscillators). The width of the three components has been constrained to that obtained for pure water. An example of the fitting-curve results is shown in Fig.6.3 for SBE-β-CD (Fig.6.3a) and α-CD (Fig.6.3b) solutions. The CH-stretching band at around 2800 cm^{-1} is reproduced with three components for the SBE-β-CD solutions and with two components for the α-CD solutions. In both cases, the ratio between the intensity of the CH- and OH-stretching bands is found to be proportional to the solute concentration (inset of Fig.6.3a), supporting the idea that the OH contribution of solute molecules is negligible, in line with previous investigations on sugar solutions [73, 225–227]. In order to provide a quantitative description of the behavior of the different systems investigated, the following quantity has been defined:

$$C(c,T) = \frac{I_{w1}(c.T)}{I_{OHtot}(c,T)} \tag{6.1}$$

where I_{w1} is the area of the OH-stretching component at lower wavenumber and I_{OHtot} is the total area of the OH-stretching band. This quantity gives an estimate of the relative amount of OH groups involved in ordered tetrahedral structures; therefore, it can be used as a quantitative indicator of the structuring/destructuring effect on water induced by the solute. Fig.6.4 shows the concentration dependence at room temperature of C obtained for glucose, α-CD, SBE-β-CD, HP-β-CD, and Met-β-CD aqueous solutions, compared with that of pure water. In the figure, it is clearly seen a linear decrease of C with concentration of SBE-β-CD solutions, pointing out a progressive destructuring of the ice-like component of water induced by this substituted form of CD. These results are in qualitative agreement with those previously obtained [225], in a smaller concentration range, using the alternative Green, Lacey, and Sheats stripping procedure. This agreement validates the current method that, differently from the previous one, does not involve depolarized spectra, allowing for an easier and yet safe comparison among different systems. In the case of un-

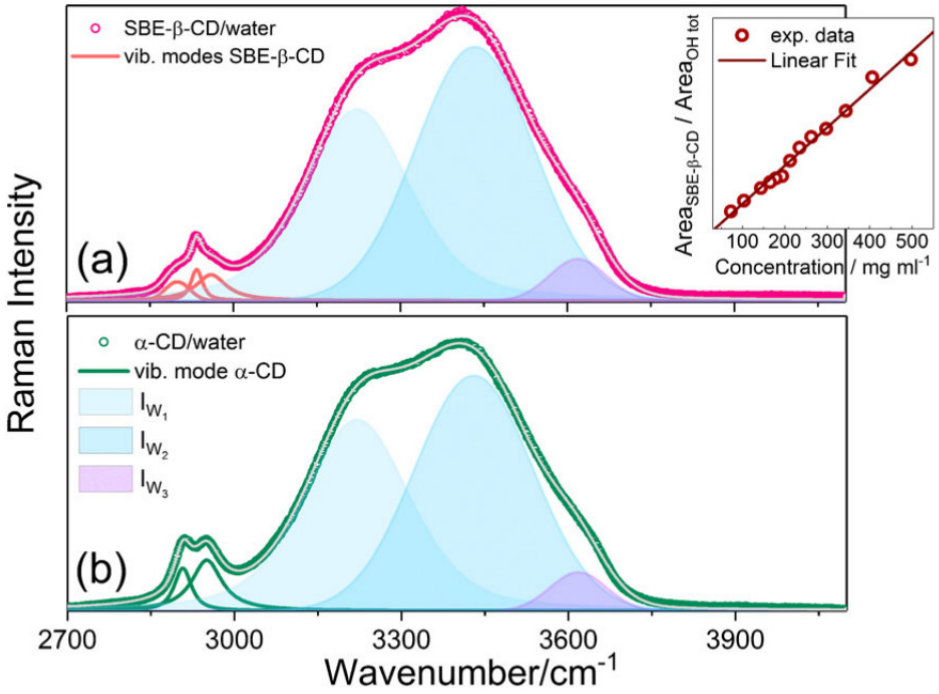

Figure 6.3: Results of the fitting procedure for (a) SBE-β-CD and (b) α-CD aqueous solutions at the same temperature (298 K) and solute concentration ($\approx$145 mg/ml). The total fit-curve and the single components assigned to CH stretching modes are indicated with lines, the OH stretching components of water are represented with shaded areas. Inset: ratio between the total area of the CH vibrational modes of SBE-β-CD and the total area of the OH stretching band, as a function of solute concentration.

substituted α-CD, C assumes values comparable to that of water, without any significant concentration dependence within experimental errors. The absence of destructuring effect persists up to relatively high concentrations, similarly to glucose, where only minor effects on the tetrahedral ordering of water are observed. Indeed, the solvent-exposed area of α-CD is characterized by a distribution of OH groups that, as in the case of glucose, induce the formation of H-bonds with water molecules similar to those formed in the solvent, leading to minor changes in their spectral distribution [211, 236]. Therefore, the destructuring effect of SBE-β-CD can be ascribed to the presence of the SBE substituent. Concerning the other chemically modified CDs, Fig.6.4 shows that HP-β-CD induces modifications of the tetrahedral water arrangement that are comparable to SBE-β-CD, whereas a remarkably stronger destructuring ef-

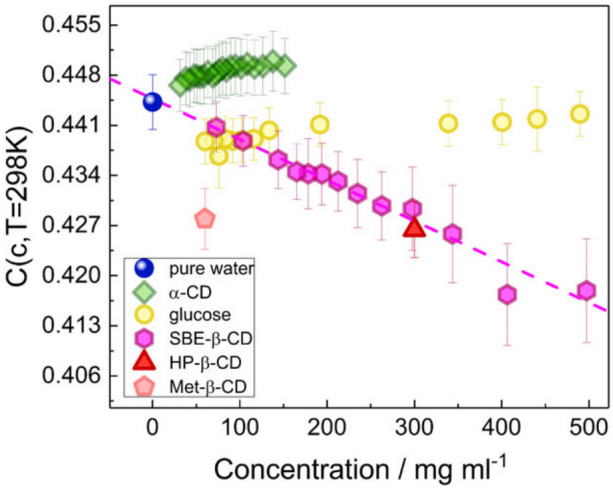

Figure 6.4: Concentration dependence of the quantity C(c,T) given by Eq.6.1, for pure water (blue circles), α-cyclodextrin (CD; green rhombs), glucose (yellow circles), sulfobutyl ether-β-cyclodextrin (SBE-β-CD; magenta exagons), hydroxypropyl-β- cyclodextrin (HP-β-CD; red triangle), and Met-β-CD (pink pentagon) aqueous solutions at temperature T=298 K.

fect is produced by Met-β-CD at the same concentration. Because HP-β-CD has almost the same substitution degree as SBE-β-CD, whereas it is about twice for Met-β-CD, changes of water ordering seem to be mainly related to the number of substituent groups rather than to their chemical nature. It is likely that a partial replacement of OH groups in the glucose units is going to impose a new local organization, which prevents the formation of a bulk-like arrangement of water within the hydration shell, typical of carbohydrates. This effect is probably related to an increased fraction of hydrophobic groups in the substituted CDs, as emerges by considering the case of Met-β-CD.

Thermally-induced effects on the H-bond network of water

Fig.6.5 shows the temperature evolution in the range 280-370 K of the Raman spectra of aqueous solutions of SBE-β-CD and α-CD prepared at a similar concentration ($\approx$150 mg/ml). The spectra qualitatively show the same temperature dependence of the OH-stretching signal as observed in pure water (inset of Fig.6.5). For both pure water and aqueous solutions, the increase of temperature leads to a rapid decrease in intensity of the lower wavenumber

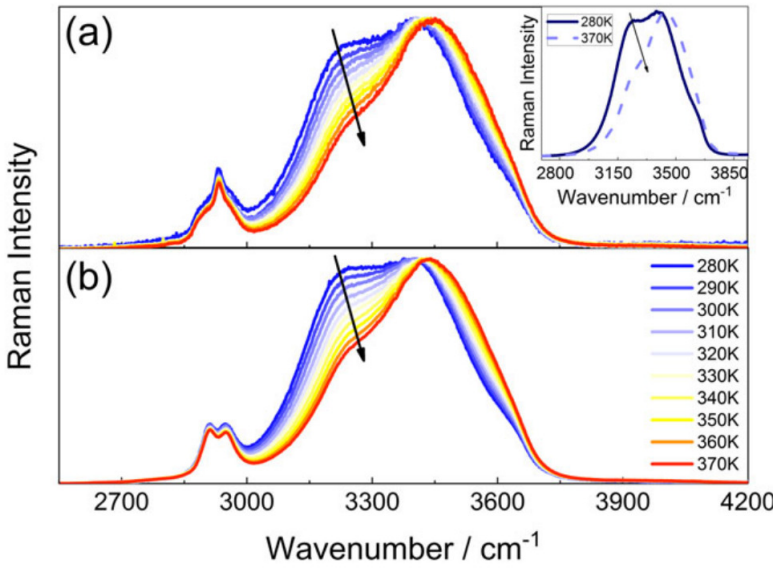

Figure 6.5: Temperature evolution of the Raman spectra for (a) sulfobutyl ether-β-cyclodextrin and (b) α-cyclodextrin aqueous solutions at a similar concentration ($\approx$140 mg/ml). The spectra are normalized to their maximum intensity. Inset: comparison between the OH stretching signal of pure water at T = 280 K (continuous line) and T = 370 K (dashed line). The arrows indicate increasing temperature.

component, along with a blue shift of the whole OH-stretching band due to a general weakening of H-bond interactions. By applying the same fit procedure discussed in the previous section, the quantity $C(c,T)$ has been calculated and used to describe the reorganization of tetrahedrally ordered water molecules (Fig.6.6). A linear decrease of C with temperature is found in pure water (in agreement with literature results [229, 237]) as well as in SBE-β-CD solutions, reflecting the destructuring caused by increased thermal motions. This effect is in addition to the C reduction caused by the presence of SBE-β-CD solute molecules, as discussed in the previous section, which is visible at all temperatures. The solute-induced effect becomes less important at higher temperatures, when thermal motions have a dominant role in decreasing the intermolecular order. However, differently from what reported in a previous study performed over a smaller concentration range [225], we observe that destructuring is clearly detected even at the highest temperatures. Fig.6.6b–d shows a comparison between C and T obtained for SBE-β-CD solutions and

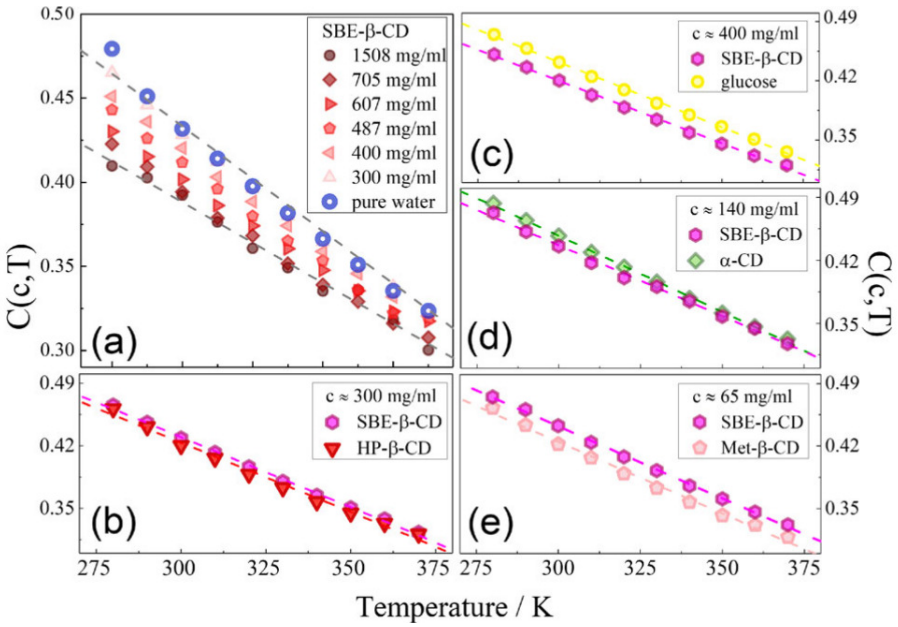

Figure 6.6: (a) Temperature dependence of the quantity $C(c,T)$ given by Eq.6.1, for pure water and SBE-β-CD aqueous solutions at increasing concentration. Comparison of C versus T for solutions of sulfobutyl ether-β-cyclodextrin (SBE-β-CD) and (b) hydroxypropyl-β-cyclodextrin (HP-β-CD); (c) glucose; (d) α-cyclodextrin (α-CD); and (e) Met-β-CD at similar concentrations (as indicated).

for other modified CDs, as well as for α-CD and glucose. In agreement with the behavior observed at a fixed T as a function of concentration (see Fig.6.4), Fig.6.6c,d confirms that both native CD and its constituent part, glucose, disturb the tetrahedral order of water less than SBE-β-CD and the disturbance tends to become less pronounced at higher temperatures. Moreover, SBE-β-CD and HP-β-CD affect the water structural order in a very similar way (Fig.6.6b), whereas Met-β-CD increases structural disorder to a greater extent, at all temperatures investigated (Fig.6.6e).

6.2 Probing the molecular connectivity of water confined in cyclodextrin-based pH-sensitive hydrogels

Hydrogels are an appealing class of cross-linked polymers that are able to absorb a large amount of water while preserving their three-dimensional structure [238–241]. Since these materials resemble living tissues more than other synthetic biomaterials, they are experiencing growing success as a main component of common products in the food industry, biomedicine [242–245], and pharmaceutics [246]. Among the wide range of polymeric formulations that give rise to biocompatible hydrogels, an attractive class of "smart gels" is represented by stimuli-responsive hydrogels [247–253]. The chemical-physical and mechanical changes occurring in these systems as a reaction to the modification of their environment have been largely investigated in the literature, especially in relation to the possibility of triggering the desired drug release [243,244,247,254]. In this framework, particular effort has been devoted to the systematic design [247–250] and characterization [251–257, 262, 263] of pH-responsive hydrogels that are particularly intriguing for use in the biomedical field due to the huge local variation of pH that occurs at several body sites under normal as well as pathological conditions [247, 251, 254]. The paradigmatic example is provided by the drug delivery of active ingredients in the intestine, characterized by a pH environment significantly higher than that of the stomach [254–257]. Several experimental techniques have been employed for the measurement and characterization of some crucial parameters in pH-responsive hydrogels [247]. For example, the morphology of the materials has widely been observed by scanning electron microscopy techniques [248–250] and the mechanical properties have usually been probed by rheological measurements [253]. At the same time, infrared and nuclear magnetic resonance spectroscopies have been used to obtain information on the chemical architecture of hydrogel materials [248, 249]. In this work, we propose a multi-scale approach for studying structural, viscoelastic and molecular properties in pH-responsive hydrogels by the joint use of UV Raman spectroscopy, Brillouin light scattering (BLS) and SANS experiments. As a prototype case study, we

explore the behaviour exhibited by natural and biodegradable cyclodextrin-based hydrogels, namely cyclodextrin nanosponges (NS) [258,259]. Compared to other strategies used for the design of smart hydrogels, the synthesis of NS offers the possibility to easily tune the properties of the final polymer network [260] and provides thesematerialswith a high versatility that opens the way to a broad range of applications [261]. SANS technique is a unique tool to characterize the structural properties of hydrogel systems. On the other hand, Raman and Brillouin spectroscopies provide access to complementary information, probing collective motions and molecular vibrations. Examples of a valuable combination of these two techniques include the study of the gel-liquid crystal phase transition in lipid membranes [276] and the estimation of the cross-linking density in polymers of cyclodextrins [277]. Moreover, dual Brillouin/Raman spectroscopy has been successfully applied for understanding the mechanical and chemical properties of nanostructured hydrogel networks and biological samples [282], confirming that this experimental approach can be very effective for studying biomaterials. Here we combine UV Raman, BLS and SANS techniques to investigate the structural and molecular response of NS hydrogels to pH changes, by focusing our attention on the properties of both polymeric and water species, with the final goal to clarify how the microscopic behaviour of the system is reflected in the water uptake of nanosponges [**?**, 283]. The case example of NS hydrogel is chosen since they are a good model system for the study of water-water and water-polymer interactions in hydrogel phases. Indeed, the structure of NS is characterized by the presence of both hydrogen-bond donor/acceptor groups and, additionally, some important parameters such as cross-linking degree, pore dimension, and hydrophilicity/hydrophobicity of the polymer matrix can be efficiently tuned by acting on the parameter n.

6.2.1 Experimental methods

Preparation of NS hydrogels

NS polymers were synthetized by following the protocols previously reported [281, 282, 284, 285]. Briefly, anhydrous β-CD was dissolved at room temperature in anhydrous DMSO containing anhydrous Et_3N and then the

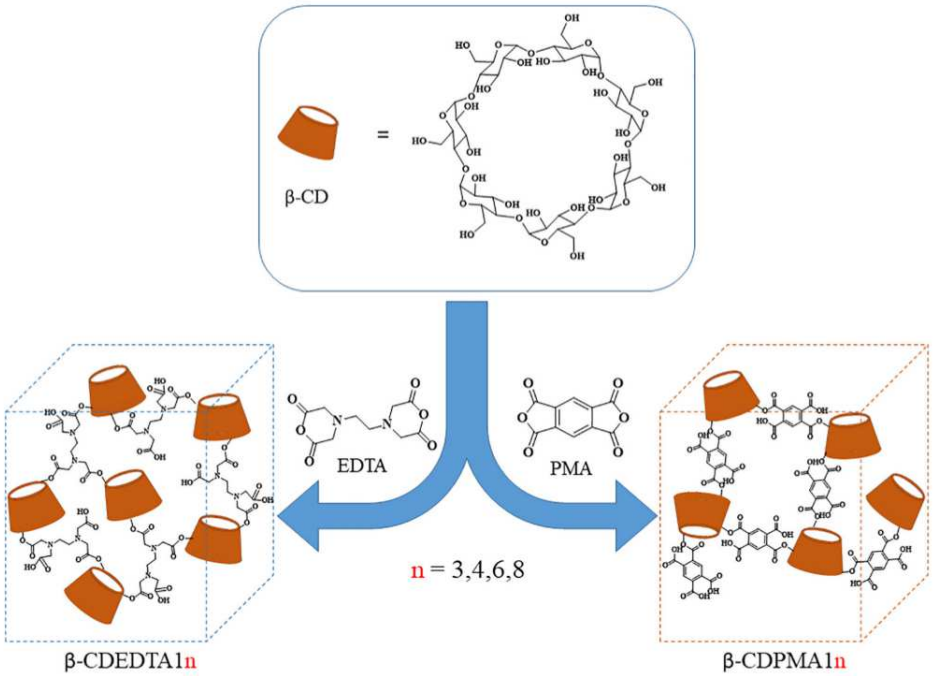

Figure 6.7: Schematic illustration of the NS synthesis by means of the two different cross-linker families, EDTA and PMA. The nomenclature adopted for the different classes of nanosponges is reported in the figure.

cross-linking agent ethylenediaminetetraacetic acid dianhydride (EDTA) or pyromellitic anhydride (PMA) was added to this solution at molecular ratios of 1:n (with n = 3, 4, 6, 8) with respect to the monomer β-CD. In the following, the acronyms β-CDEDTA1n (β-CDPMA1n) indicate the NS polymers obtained by the polycondensation process between β-CD and EDTA (PMA) with starting molar ratios β-CD:EDTA (PMA) = 1:n. Fig.6.7 reports a schematic illustration of the NS synthesis by means of the two different cross-linker families. The results of a preliminary characterization, at molecular level, of the structure of EDTA- and PMA-NS polymers (in dry state) by varying the main parameters of the synthesis are summarized in Ref. [278]. The corresponding NS hydrogels, to be used for Brillouin, UV Raman scattering and SANS experiments, were prepared by adding a suitable amount of double distilled water H_2O (for BLS and Raman spectroscopy measurements) or deuterated water D_2O (for SANS experiments) to a weighed quantity of dry NS polymer in order to obtain the desired hydration level h (where h is defined as the

weight ratio of water/NS). In order to reduce the incoherent contribution to the total scattering cross sections measured, the NS hydrogels used for SANS measurements were prepared by repeating the D_2O swelling and freeze drying cycles several times, in order to promote the hydrogen-deuterium exchange. In all the hydrogel preparations, an increasing quantity of anhydrous Na_2 CO_3 was dissolved in the hydrating H_2O or D_2O solution (at concentrations ranging from 5 to 25% w/w) to achieve the desired pH of the resulting gel phase. Na_2 CO_3 was selected as pH modulator for the following reasons: i) stable, high concentrated solutions can be prepared and used without interfering with the analytical techniques, as would happen by using organic bases; ii) the use of NaOH or other strong bases would promote hydrolysis of the NS, altering the structure of the network. The pH values reported in the following for NS hydrogels have been measured by using a standard pH meter (HALO© Wireless pH Meter). The pH values between β-CDEDTA and β-CDPMA nanosponges differ even when using the same Na_2 CO_3 % w/w solutions. This behavior should be ascribed to the different content of free-carboxylic groups present in the two NS hydrogels.

SANS measurements

SANS measurements were performed at constant temperature (298 K) at the KWS-2 diffractometer of Jülich Centre for Neutron Scattering at the Heinz-Meier Leibnitz Center, Garching (Germany) [286–289]. Neutrons with a wavelength spread $\Delta\lambda/\lambda = 0.2$ were used. Three different wavelength (W)/collimation (C)/sample-to-detector distance (D) combinations ($W_{5.2\mathring{A}}$ C_{8m} $D_{1.2}$m , $W_{5.2\mathring{A}}$ C_{8m} D_{8m} , $W_{5.2\mathring{A}}$ C_{20m} D_{20m} , and $W_{19.6\mathring{A}}$ C_{20m} D_{20m}) allowed measuring cross sections in a range of the scattering wave-vector transfer modulus between $7.9 \cdot 10^{-4}$ and $0.34\mathring{A}^{-1}$. All the investigated samples were sealed in a closed round sandwich cell and measured for enough time to collect an intensity integrated over the whole 2D detector of about 2 million counts. The obtained raw data were then corrected for background and empty cell scattering. Detector sensitivity corrections and transformation to absolute scattering cross sections were made with a secondary plexiglass standard prior to radial averaging of data [286–289].

Brillouin light scattering measurements

Brillouin light-scattering measurements have been carried out by using an incident radiation with wavelength of 532 nm. The polarization was chosen to be perpendicular to the scattering plane and only scattered light with the same polarization (VV) was collected and analyzed by a high-resolution Sandercock-type tandem 3 + 3 pass Fabry-Pérot interferometer. The BLS spectra were recorded in the back-scattering geometry on freshly prepared samples of NS gels at h = 4 as a function of pH and at room temperature. No correction of BLS spectra for dark count was necessary.

UV Raman spectroscopy measurements

UV Raman spectra on NS hydrogels were carried out by using the setup descripted in detail in Chapter 2. All the samples were freshly prepared and placed in optical quartz cuvettes for the measurements.

6.2.2 Correlation between collective and molecular dynamics in pH-responsive cyclodextrin-based hydrogels

NS hydrogels exhibit marked modifications in their solvation and gelling behavior in response to changes in the temperature and pH of the environment [269–271, 297]. The pH range is limited by the experimental observation that a homogeneous hydrogel could only be obtained by swelling the polymer with a basic solution containing at least 5% w/w Na_2CO_3 [297]. Accordingly, we prepared four different gels with an increasing (5, 10, 15, 20%) amount of Na_2CO_3 , affording a pH value of 6.3, 8.7, 9.5 and 9.8, in that order. In the following, the effect of temperature and pH on the Raman and Brillouin spectra will be separately analyzed, and an interpretative model of the mechanism of responsivity of NS hydrogels will then be provided.

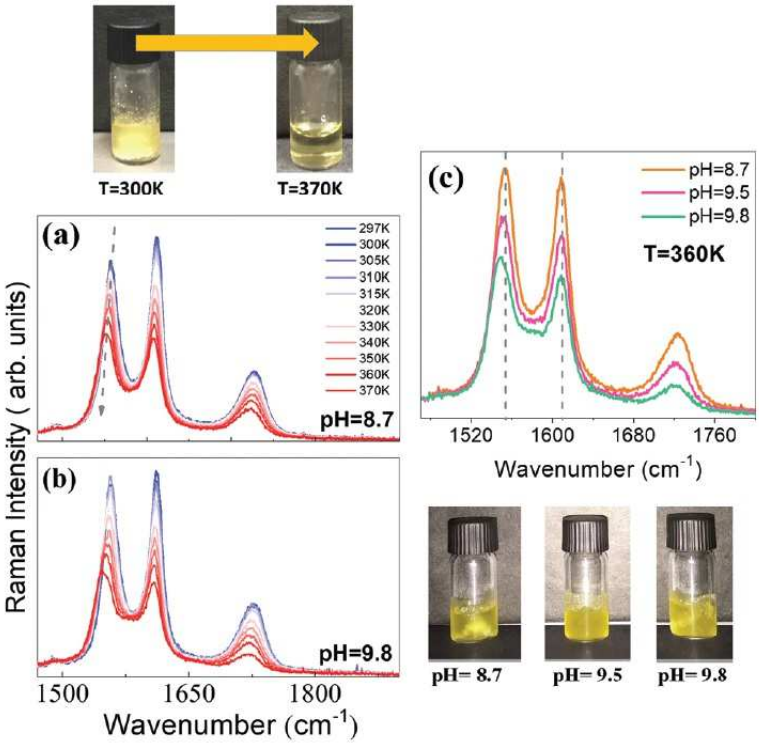

Figure 6.8: (a and b) Temperature evolution of Raman spectra collected for β-CDPMA13 hydrogels at pH = 8.7 and pH = 9.8, respectively. (c) Comparison between UV Raman spectra collected at T = 360 K on the β-CDPMA13 hydrogel at pH = 8.7, 9.5 and 9.8. The photographs reported in the panel show the macroscopic changes observed in the gel as function of temperature and pH.

Temperature and pH effects on the local molecular dynamics of NS hydrogels

On the basis of the assignment of vibrational Raman signals previously reported [269,297], the UV Raman spectra of the NS hydrogels were investigated in the spectral range of 1500-1800 cm^{-1}. Fig.6.8(a) and (b) show an example of polarized UV Raman spectra collected for two β-CDPMA13 hydrogels at pH = 8.7 and 9.8, respectively, and different temperatures. The spectra are dominated by the signals associated with the vibrations of the PMA residues, which cross-link different CD units. As already shown in previous work [269,280,297], these modes are sensitive to the water-polymer interactions, which change with temperature and pH. As revealed in previous work [278, 297], the increase in

temperature causes the transition of the nanosponge sample from a macroscopic self-sustained gel to a flowing system [302](see the pictures in Fig.6.8). Similar phase evolution, i.e. from flowing to rigid gel and vice versa, has already been observed and discussed in other nanosponge-based hydrogels under different experimental conditions [302]. In the present case, the phase transformation undergone by NS hydrogels as a function of temperature is associated with a general decrease in intensity of the Raman profiles, as evidenced in the spectra of Fig.6.8(a) and (b). A marked red-shift of the Raman peaks is also observed. This general wavenumber reduction appears more pronounced for the Raman mode at about 1555 cm^{-1} , as highlighted by the arrow in Fig.6.8(a). The Raman spectra also exhibit a great sensitivity to the pH variation, as can be noted from the comparison of experimental profiles at different values of pH reported in Fig.6.8(c). On increasing pH, the most relevant spectral change seems to be the shift toward lower frequency of the band at about 1555 cm^{-1}. Therefore, this Raman mode happens to be sensitive to temperature and pH variations.

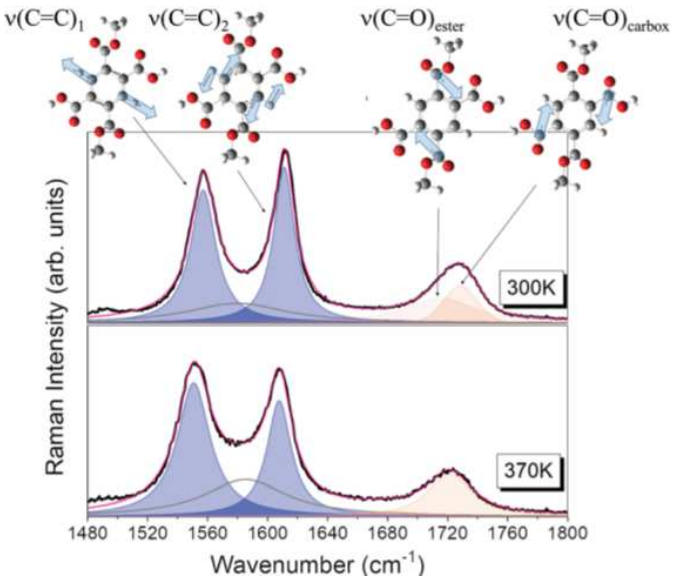

Figure 6.9: Example of fitting obtained on Raman profiles collected for the β-CDPMA13 hydrogel at pH = 8.7 at two different representative temperatures, 300 and 370 K. The sketches reported at the top of the panel represent the vibrational modes associated with the experimental Raman peaks.

For a more quantitative description of these modifications, the main spectral parameters of the investigated Raman bands have been obtained by means of a fitting procedure. Fig.6.9 displays the best-fitting curves of the Raman spectra for the β-CDPMA13 hydrogel at pH = 8.7, at two representative temperatures. A good decomposition of the experimental profiles has been achieved by means of the five spectral components displayed in Fig.6.9. The assignment of these components to the vibrational modes of PMA residues in the structure of NS (as sketched at the top of the figure) was made on the basis of the comparison between the experimental and theoretically computed Raman spectra [269, 297]. The band at 1550 cm^{-1} corresponds to a ring breathing motion of PMA and it is labeled as $\nu(C{=}C)_1$, whereas the component $\nu(C{=}C)_2$ arises from a combination of stretching vibrations of the aromatic CQC bonds and bending of the C-H groups on the PMA unit. Both these modes can be satisfactorily reproduced by using two Lorentzian functions (cyan filled components reported in Fig.6.9). The broad spectral band appearing at about 1580 cm^{-1} was described by using a Voight function (gray line in Fig.6.9). This vibrational component, already observed in the spectra of NS hydrogels [297], has been ascribed to the establishment of intermolecular interactions, mainly involving the CH groups of PMA. Finally, two Voigt functions, centered at about 1730 and 1715 cm^{-1} , were used to reproduce the asymmetry present in the band profile associated with stretching vibrations of the C=O groups. These two bands have been previously assigned to the different stretching vibrations arising from the C=O moieties that belong to the ester and carboxylic groups of PMA (components labeled as $\nu(C{=}O)_{ester}$ and $\nu(C{=}O)_{carbox}$, respectively), both present in the polymer network of PMA-based nanosponges [269–271, 297]. As already noted in previous work [269], the UV Raman spectra, excited with a light wavelength close to the $\pi - \pi^*$ electronic transitions of the aromatic groups, show a selective moderate enhancement of the intensity of the Raman peaks assigned to vibrations involving the aromatic moieties compared to those associated with functional groups such as carbonyl groups. This condition turns out to be useful to detect also slight spectral modifications occurring in the Raman bands connected to the aromatic moieties in the polymer network of the NS. The described fitting procedure has allowed us to extract reliable values for the frequency position of

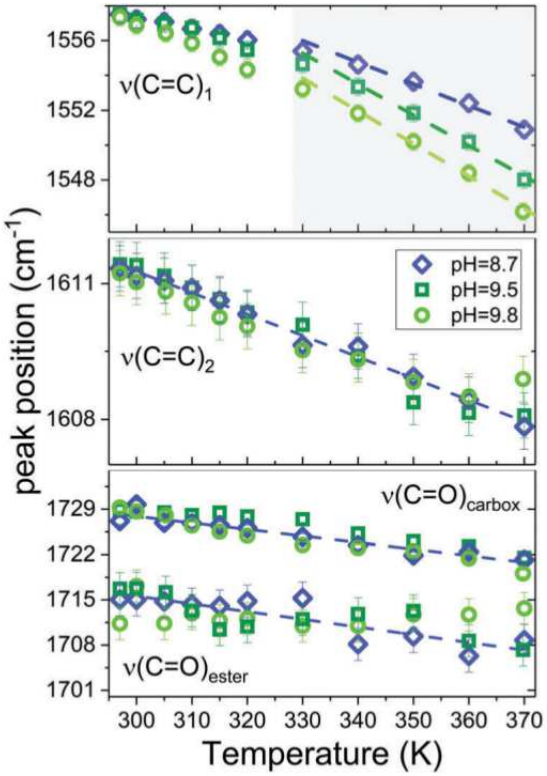

Figure 6.10: Temperature evolution of the wavenumber position of the modes ν(C=C)$_1$, ν(C=C)$_2$, ν(C=O)$_{ester}$ and ν(C=O)$_{carbox}$ (from the top to the bottom, respectively) obtained for βCDPMA13 hydrogels at different pH values. Solid lines represent linear fits of the experimental data. The rectangular box in the top panel indicates the T range where a linear behavior is expected.

all Raman peaks in the frequency range of 1500-1800 cm^{-1} , for NS hydrogels prepared at three different pH values. Fig.6.10 shows the temperature dependence of the frequency of Raman peaks related to aromatic ring vibrations, ν(C=C)$_1$ and ν(C=C)$_2$, and to carbonyl stretching modes, ν(C=O)$_{ester}$ and ν(C=O)$_{carbox}$. From this figure, the red-shift on increasing the temperature of all Raman modes in the investigated spectral window is clearly observed, confirming what was qualitatively noted in Fig.6.8. The plot at the bottom of Fig.6.10 shows some fluctuations, especially at high temperatures, in the frequency position of the ν(C=O)$_{ester}$ mode, although the overall trend is decreasing on heating the sample. On the other hand, the determination of this

frequency is more uncertain compared to that of the other vibration peaks due to a higher correlation between the fitting parameters describing the two peaks assigned to the carbonyl stretching modes. The red-shift behavior observed for the frequency positions reported in Fig.6.10 can be interpreted as the vibrational signature of the progressive phase modification occurring in the NS samples that at high temperatures appear in a completely solvated state of NS domains (see the photographs in Fig.6.8). Interestingly, the rate of decrease with temperature of the frequency position of the mode $\nu(C{=}C)_1$ increases on increasing pH, whereas the frequency of $\nu(C{=}C)_2$ and of the stretching modes associated with the C=O groups is almost pH-independent. The vibrational mode $\nu(C{=}C)_1$ is therefore a sensitive probe of the molecular rearrangements of the hydrogel structure in response to pH changes, consistent with observations in other types of NS gels [271,297,302]. This sensitivity can be explained on the basis of the strong influence on this mode of the establishment of interactions with water molecules, which are strongly directional and specifically involve the hydrophobic CH groups on PMA moieties [269]. The effect of pH on the $\nu(C{=}C)_1$ peak position is more evident in the high-temperature region (above E330 K), suggesting that the force constant of this ring-breathing mode tends to decrease more rapidly as a function of T the higher the value of pH (see the top panel of Fig.6.10). This indicates that basic pH-conditions promote the phase change in NS hydrogels, possibly through the activation of the C-H bond of the PMA unit toward solvation [271,297]. This transition is accompanied by a progressive reorganization of water-polymer interactions involving the PMA units, as suggested by previous work [280, 297]. In particular, the behavior of the $\nu(C{=}C)_1$ peak position indicates that the most hydrophobic parts of the polymeric network improve their accessibility to water molecules as the temperature increases. This process is markedly triggered by pH, which tends to favor the sensitivity of the NS polymer matrix to temperature variations.

Collective restructuring of hydrogen bonding in NS hydrogels

Fig.6.11 shows the typical profile of the BLS spectra of the NS hydrogels. The evolution from the rigid to flowing gel state, previously discussed, clearly affects also the BLS spectra. The intensity of light scattered from longitu-

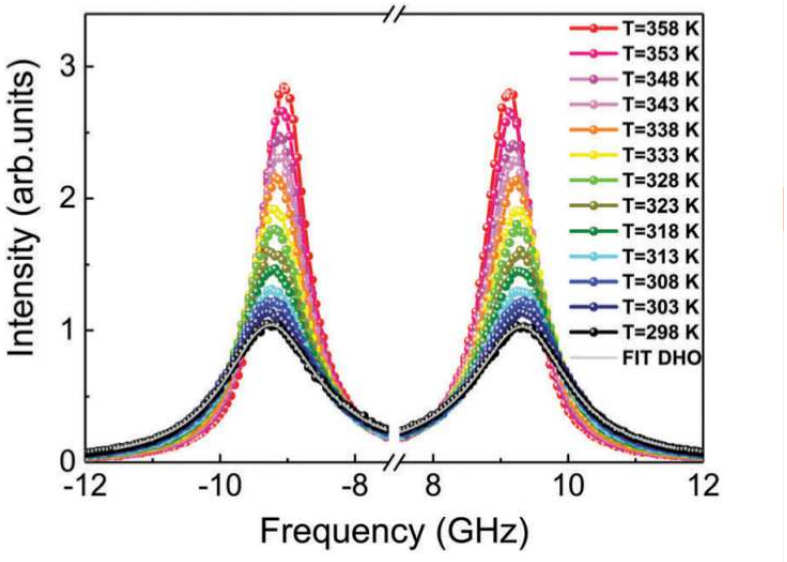

Figure 6.11: Brillouin spectra collected on the β-CDPMA13 hydrogel prepared at pH = 9.5 as a function of temperature. A typical fit curve using a DHO function (Eq.6.5) is reported as a gray line for the spectrum at T = 298 K.

dinal phonons at different temperatures is shown in Fig.6.11 for a sample of β-CDPMA13 gel prepared at pH = 9.5. Stokes and anti-Stokes frequency shifts are observed to the left and right of the Rayleigh line (broken axis). The frequency position $\omega_L/2\pi$ and linewidth $\Gamma_L/2\pi$ of the Brillouin peaks, obtained by fitting the spectra with Eq.6.2, are both sensitive to temperature changes. To analyze the temperature dependent behavior of the parameter $\Gamma_L/2\pi$ (directly related to the longitudinal viscosity of the sample [303]) we better represent the data on the Arrhenius plot (Fig.6.12) where a thermally activated behavior would appear as linear.

The qualitative similarity of the behavior of all samples suggests a common nature of the dynamic process experienced by the NS hydrogels prepared at different values of pH. Before proceeding to a quantitative description of this process, a preliminary evaluation of the T range suitable to extract the relevant physical information is needed. An indication is provided by the cases of pure water and aqueous solutions studied in ref. [303] and [304]. In such cases, the translational motion associated with density fluctuations and probed by BLS was found to be related to a local collective H-bond breaking and reforming

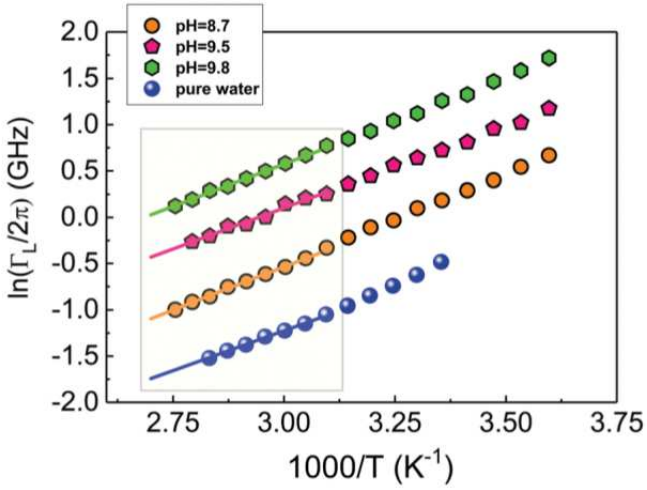

Figure 6.12: Arrhenius plot of the acoustic attenuation parameter $\Gamma_L/2\pi$ for β-CDPMA13 gels prepared at different pH. The data collected on pure water are also reported in the same graph for comparison. For the sake of clarity, the data were vertically shifted by a factor of 0.3 for the NS gel at pH = 9.5, and by a factor of 0.6 at pH = 9.8. Solid lines represent the fit with a thermally activated Arrhenius-law (Eq.6.2). The rectangular box indicates the T range where the Arrhenius behavior is expected (see the text).

mechanism, and the sound attenuation in the high temperature region to be an indirect probe of this restructuring process. Indeed, when T is sufficiently high the Brillouin peaks are located at frequencies much lower than the relaxation rate of this process ($\omega_L \ll 1/\langle\tau\rangle$, with the average relaxation time $\langle\tau\rangle$ ranging from fractions to a few picoseconds), i.e. the system is in a completely relaxed regime. In this regime, the linewidth $\Gamma_L/2\pi$ is directly related to $\langle\tau\rangle$, and exhibits the same thermally activated behavior [303, 304]. Therefore, it can be used to determine the activation energy of the relaxation process itself. In the present case of NS hydrogels, we find that in the temperature range of 323-353 K the relaxed condition is satisfied for all the investigated samples, and an Arrhenius behavior of $\Gamma_L/2\pi$ is expected. At lower temperatures the data should deviate from Arrhenius behavior due to the onset of cooperative motions with a different microscopic nature. Indeed, the data reported in Fig.6.12, including those for pure water, are well reproduced, in this range, by the expression

$$ln\Gamma_L = ln\Gamma_0 + E_A/RT \tag{6.2}$$

Sample of NS gel	E_A(kJ mol^{-1})
βCDPMA13 gel pH = 8.7	15.5 ± 0.3
βCDPMA13 gel pH = 9.5	14.8 ± 0.8
βCDPMA13 gel pH = 9.8	15.1 ± 0.4
Pure water	14.3 ± 0.3

Table 6.2: Estimated activation energy, E_A as obtained from the analysis of Brillouin linewidth for samples of NS gels prepared at different pH and pure water.

where Γ_0 is a pre-exponential factor, E_A the activation energy and R the gas constant. Tab.6.2 shows that the values of E_A obtained for the NS hydrogels are the same, within the experimental error, and almost equal to the value for pure water. This finding indicates that the translational collective dynamics probed by BLS in the hydrogels is dominated, similarly to water, by the thermally activated process of restructuring of the H-bond network, taking place in the picosecond time window. Interestingly, the H-bond restructuring process, which likely involves the more hydrophilic moieties in the polymer backbone of NS (C=O and OH chemical groups of cross-linking agent and CD units), is not affected by pH. This further supports that the pH-dependent mechanism in the thermoresponse of NS hydrogels is dominated by the hydrophobic solvation of the aromatic groups of PMA residues in the skeleton of the polymers [280,297] rather than the H-bond reorganization around hydrophilic parts of the NS domains.

pH-Dependence of phase changes in NS hydrogels

The changes with temperature of the BLS peak frequency position observed in the spectra of NS hydrogels (see Fig.6.11) can be attributed to a change in the average elastic properties of the sample, corresponding to a decrease in the longitudinal acoustic modulus, according to:

$$M'(\omega_L) = \rho\frac{\omega_L^2}{q^2}; M''(\omega_L) = \rho\omega_L\frac{\Gamma_L}{q^2} \tag{6.3}$$

Fig.6.13(a) displays the BLS frequency shift as a function of temperature, at different values of pH. As a common feature of all the gel samples, a decrease in

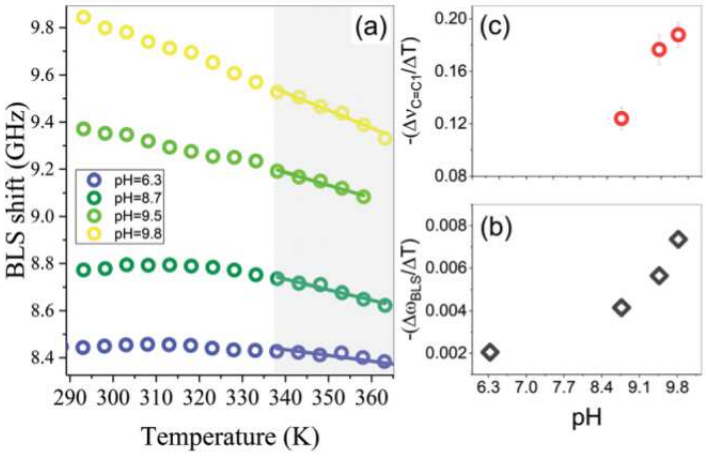

Figure 6.13: (a) Temperature evolution of Brillouin peak position for β-CDPMA13 gels at different pH; solid lines represent linear fits of the experimental data, and the rectangular box indicates the temperature range where a linear behavior is found. (b and c) pH dependence of the quantities $-\frac{\Delta\nu_{C=C1}}{\Delta T}$ and $-\frac{\Delta\omega_{BLS}}{\Delta T}$, respectively, calculated as described in the text.

the BLS frequency on heating is observed. A similar red-shift was also observed in the Brillouin peaks of dry NS as a function of the degree of cross-linking [277]. This behavior was ascribed to a change in the stiffness of the whole polymeric network, leading to general softening of the material. In a similar way, the data of Fig.6.13(a) are consistent with the transition of NS hydrogels from a state of connected gel toward a fully solvated state of NS domains, as the temperature increases. Further, a smooth change in the temperature dependence of the Brillouin frequency is visible in all the samples, suggesting that the inter- and intra-molecular rearrangements of the NS domains upon heating also affect the collective properties (propagation of acoustic waves) of the system. It should be noted that in the high-temperature region, above ≈335 K, the BLS frequency tends to decrease linearly with temperature, with a higher slope for samples prepared at higher pH. Fig.6.13(b) shows the value $-\frac{\Delta\omega_{BLS}}{\Delta T}$ of this slope as a function of pH, revealing a marked pH dependence. This quantity can be used as a physical descriptor of the rate of softening of the NS hydrogel upon heating the system. The results in Fig.6.13(b) indicate that the elastic modulus has a more pronounced temperature variation at higher pH, confirming that basic pH-conditions tend to favor the solvation of NS

domains, leading to phase change in the hydrogel. Interestingly, a similar pH-dependent effect is observed for the temperature dependence of the frequency position associated with the Raman mode $\nu(\mathrm{C{=}C})_1$, shown in the top panel in Fig.6.10. The slope $-\frac{\Delta\nu_{C=C1}}{\Delta T}$ of the curves, derived from a linear fit of the data in the high-temperature region, describes the rate of reduction of the force constant for the ring-breathing mode $\nu(\mathrm{C{=}C})_1$ due to the rearrangement of the intermolecular interactions involving the aromatic moieties of PMA in the NS polymer network and leading to a major exposure to the solvent of the hydrophobic residues. The increasing value of the slope $-\frac{\Delta\nu_{C=C1}}{\Delta T}$ with increasing pH (see Fig.6.13(c)) confirms the mechanism previously proposed [280, 297] the slightly acidic behavior of the CH groups in the aromatic rings of PMA is further activated at basic pH, thus promoting a greater exposure of these hydrophobic sites to the collision with solvent molecules. Intriguingly, the pH-dependence of the quantities $-\frac{\Delta\nu_{C=C1}}{\Delta T}$ and $-\frac{\Delta\omega_{BLS}}{\Delta T}$ is the same, according to Fig.6.13(b) and (c).

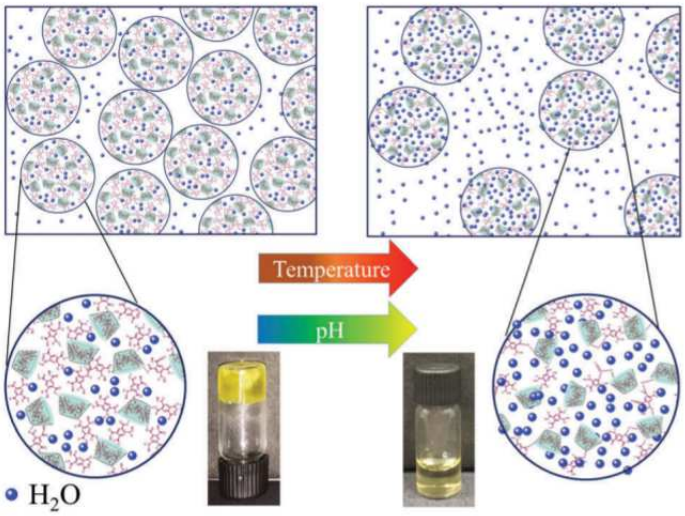

Figure 6.14: Sketch of the evolution of the nanosponge hydrogel from the macroscopic gel phase to the solvated state of NS domains, in response to variations of temperature and pH. The increasing of the temperature reflects both an increase of interpenetration of water molecules inside the pores of each NS molecule (sketches at the left) and a progressive distancing of the NS domains among them (panel at the right). Both of these effects are strongly favored at high pH.

This finding indicates a correlation between the local (molecular) and the collective properties of the NS hydrogels during the phase transformation triggered by pH. The two techniques, Raman and BLS spectroscopies, both provide indication that an increase in pH leads to an improved temperature-sensitivity of the NS hydrogel, which is reflected in the properties of the system at a mesoscopic and a macroscopic length-scale. The correlation between collective and molecular dynamic behavior revealed by Raman and BLS spectroscopies is suggestive of a mechanism for explaining the pH-sensitive phase change occurring in NS hydrogels on increasing the temperature, as sketched in Fig.6.14.

Heating the gel sample promotes two different effects that cooperate and drive the phase transformation of the system from the state of a rigid gel to a liquid suspension of NS domains (see the photographs reported at the left and the right in Fig.6.14, respectively), which is macroscopically observed in nanosponge samples. On one side, the T increase improves the accessibility of water solvent molecules to the hydrophobic sites of the NS backbone, as probed on a molecular length-scale by the changes in frequency of the Raman peaks and, in particular, of the peak associated with the ring breathing mode $\nu(\mathrm{C{=}C})_1$. At the same time, the T increase induces a rearrangement of the intermolecular interactions inside the gel network leading to a progressive separation of NS domains, and resulting in a decreased sound velocity. As a result of the combination of these two effects, heating induces a solvation process of the NS polymer network that is strongly triggered by the increase in pH. The process illustrated in Fig.6.14 also appears to be consistent with the interplay between physical and chemical interactions previously proposed to explain the peculiar gelling behavior exhibited by cyclodextrin-based hydrogels [305].

6.2.3 Structural and molecular response in cyclodextrin-based pH-sensitive hydrogels by the joint use of Brillouin, UV Raman and Small Angle Neutron Scattering techniques

SANS experiment: structurale response to pH After the investigation of the interesting behavior exhibited by PMA-NS as a function of

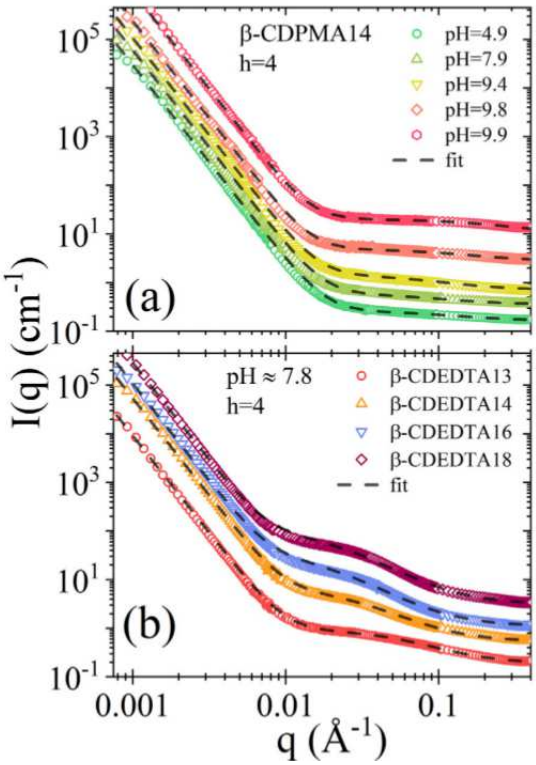

Figure 6.15: SANS patterns collected on β-CDPMA14 hydrogels swollen at h = 4 and at increasing pH (a) and on different gels of β-CDEDTA1n (n = 3, 4, 6, 8) prepared at fixed hydration h = 4 and pH $\approx$ 7.8 (b). Experimental data are reported as symbols and their corresponding fit curves as dashed lines. The different data sets have been multiplied for suitable factors in order to shift them and allow for a better visualization of both data and fitting curves.

temperature and pH, we go to compare the behaviour exhibited by NS hydrogel in presence of two different cross-linker: PMA and EDTA. The structural response of different type of NS hydrogels to pH changes were monitored and quantified by SANS experiments. Fig.6.15 (a) displays some representative SANS curves collected for β-CDPMA14 hydrogel at increasing pH values. Fig.6.15(b) reports a series of scattering intensities for different gels β-CDEDTA1n (n = 3, 4, 6, 8) at a fixed pH. All the experimental data show, as dominant features, an upturn at low q and a broad shoulder in the medium q-range located between about 0.01 and 0.1 $\mathring{A}^{-}1$ or larger. Similar SANS patterns were already observed for a series of similar PMA- and EDTA-NS

hydrogels at different hydration level [279]. The diffraction features described above were linked to specific structural properties of the polymer network of NS hydrogels at different length scales [279], spatial inhomogeneities on a scale from few to hundreds of nm and concentration fluctuations of the gel network arising from the inhomogeneity in the distributions of the chain-lengths and of the cross-linking sites, respectively. The comparison reported in Fig.6.15(a) and (b) points out qualitative differences in the shape of the SANS curves of NS hydrogels depending on the cross-linker used for polymerization of CD (EDTA or PMA). Indeed, the I(q) measured for EDTA-NS gels shows a more pronounced shoulder in the medium q-range that is centred at about 0.015 $\mathring{A}^{-1}$, while the same feature appears shifted toward higher q-values in the case of gels of PMA-nanosponge. This is consistent with previous SANS investigations [279] and confirms that the chemical nature of the cross-linker affects the local structure of the corresponding NS polymer. Moreover, the SANS data reported in Fig.6.15(b) suggest that the structural properties of the gel significantly vary when changing the parameter n, i.e. the relative quantity of cross-linking agent with respect to the CD monomer used during the synthesis of EDTA-NS polymers. The SANS curves similar to those collected on NS gels can be phenomenologically described as a combination of long-range frozen inhomogeneities and local liquid-like scattering functions [279, 290, 291]. Therefore, a two-correlation length model [279, 290–295] was employed to fit the SANS curve with the empirical functional form:

$$I(q) = \frac{A}{q^4} + \frac{B}{(1 + (\zeta q)^2)} + bkg \tag{6.4}$$

where the two factors A and B and the q-independent background bkg are used as fitting parameters. The parameter ζ corresponds to the short-range correlation length for polymer chains that, in the case of polymeric gels, can be considered as a reasonable estimate of the typical mesh size between neighbouring crosslinks [290–292, 294, 295]. In the specific case of NS, that are 3-D cross-linked polymers obtained by a step-growth polymerization process, the correlation length ζ has been interpreted as an experimental assessment of the average size of the hydrophilic pores where, in the gel phase, water is mainly confined [279]. The outcome of the fitting procedure through Eq.6.4 is shown in Fig.6.7(a)-(b) and it can be considered excellent if compared to those found

in the literature for similar systems [290, 291, 293]. The pH-dependence of the parameter ζ, estimated for PMA- and EDTA-NS prepared at the fixed hydration value h = 4, is reported in Fig.6.16(a)-(b). As first remark, the comparison

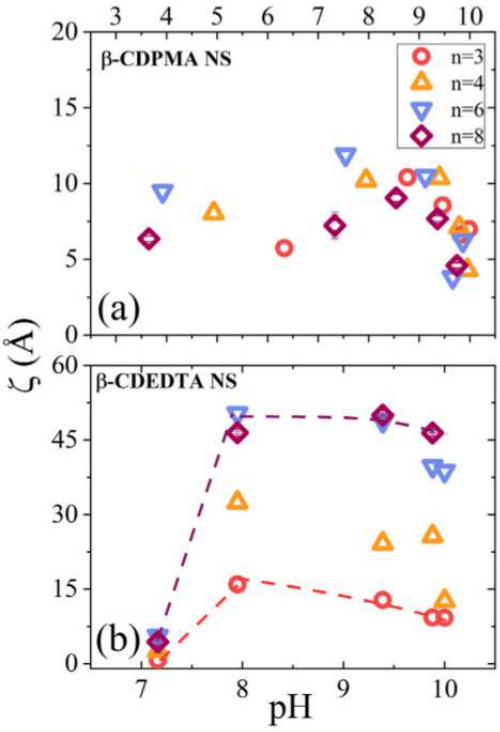

Figure 6.16: Correlation length ζ estimated for β-CDPMA1n (a) and β-CDEDTA1n (b) hydrogels as a function of pH measured in the sample; the dashed lines are guides for eyes. The error bars are not fully visible because the most of them are inside the dimension of the points.

between the plots reported in Fig.6.16 (a) and (b) gives evidence that the average size of the pores in PMA-hydrogels is smaller (about $2 \div 12$ $\mathring{A}$) than that observed in the other gels based on EDTA ($1 \div 55$ $\mathring{A}$). As PMA and EDTA are representative of short-rigid and long-flexible spacers, respectively, this finding confirms that a modulation of the void size in NS can be designed by properly choosing the cross-linking agent. This interpretation is also fully consistent with previous SANS investigations on the structural effects of water absorption in NS polymer network that gave evidence of the larger value of the upper limit of the mesh-size for EDTA nanosponges with respect to PMA

ones [279], reflected in turn in a better water uptake observed for the former type of NS. By inspection of Fig.6.16(b), we observe that the correlation length ζ in EDTA-based hydrogels sharply increases on passing from pH = 7 to pH = 8 and then attains a sort of plateau, before slowly dropping for higher pH values. Also, the pH response observed for β in EDTA-based NS hydrogels is markedly influenced by the parameter n (i.e. molar ratio between the cross-linker and the monomer in the polymerization), as clearly indicated by the plots of Fig.6.16(b). The data show that high values of molar ratio (n = 6, 8) lead to hydrogels with generally larger hydrophilic pores and more sensitive to pH changes. This is also in line with previous investigations that evidenced for n N 6 an increment in the degree of branching [278] leading to the formation of additional -COOH groups in the polymer network of the corresponding NS. On the other hand, in the case of PMA-based hydrogels (Fig.6.16(a)), ζ seems to be much less sensitive to pH variations. In addition, the local structure of PMA-NS hydrogels seems to be not significantly affected by the choice of molar ratio n during the polymerization, giving rise to materials that exhibit a less marked change in the mesh-size of hydrogel network even when pH is significantly changed. The overall structural picture emerging from the analysis of SANS data is that the type of cross-linking agent plays a key role in determining the structural properties of NS on the nanometer length scale. In particular, i) the larger molecular dimension, ii) the higher flexibility, related to the conformational degrees of freedom, and iii) the acid-base properties of the EDTA cross-linker seem to confer to NS a better responsivity to pH change.

BLS measurements: elastic characterization Brillouin spectroscopy detects photons that are inelastically scattered by spontaneously (thermally) induced collective density fluctuations that propagate in all directions (acoustic phonons), and offers a non-invasive method to investigate the mechanical properties of materials [281, 282, 296]. In particular, the frequency position of the Brillouin peaks can be used as a physical descriptor of the elasticity of the hydrogel network, over a mesoscopic length scale. Fig. 4(a)–(b) show the typical Brillouin spectra acquired in PMA- and EDTA-NS, respectively, prepared at fixed hydration level using a solution at 15% of Na_2CO_3. As a first remark, clear differences appear in the spectral shape of the BLS spec-

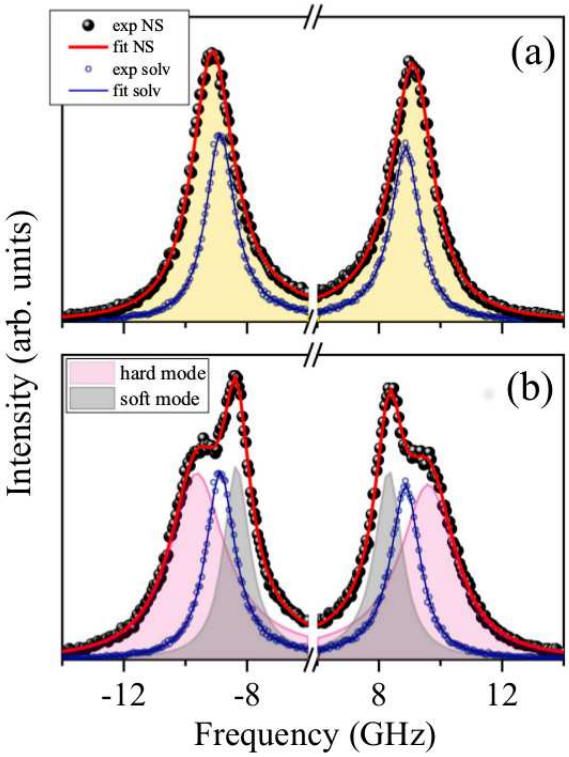

Figure 6.17: Brillouin spectra for (a) β-CDPMA18 and (b) β-CDEDTA18 at h = 4 and pH = 9.0. Experimental data are reported as symbols; solid lines represent the corresponding fit curves obtained by using one or two DHO functions. Coloured areas indicate the different DHO contributions. In both panels, the BLS spectrum of the solvent solution H_2O + Na_2CO_3 15% w/w and the corresponding fit curve are indicated with blue empty circles and full line, respectively.

tra from EDTA and PMA-based nanosponges. In particular, in the case of EDTA-NS (see Fig.6.17(b)) the spectra show two components at frequencies sufficiently separated to be clearly resolved, indicating the coexistence of a soft (at lower-frequency) and a hard (at higher-frequency) acoustic mode. This feature is observed in all samples but β-CDEDTA13. On the contrary, a single peak is found in the case of PMA-NS (see Fig.6.17(a)). It should be noted that the acoustic modes probed by BLS have a typical wavelength of ∼200 nm and involve cooperative motions propagating over a distance of at least a few wavelengths. Therefore, our findings suggest that, over the length-scale of several hundred nanometers, the hydration of EDTA-NS gives rise to a

more heterogeneous material compared to PMA-NS. To get more quantitative information, the spectra have been analyzed according to a well-established procedure [276, 277, 281]. Each contribution, I(ω), to the intensity of the totally scattered light has been modelled using a damped harmonic oscillator (DHO) lineshape, i.e.:

$$I(\omega) = R(\omega) \bigotimes \frac{I^0}{\pi} \frac{\Gamma_B \omega_B^2}{[\omega_B^2 - \omega^2] + [\omega \Gamma_B^2]} \tag{6.5}$$

where R(ω) is the instrumental resolution function, the symbol $\bigotimes$ represents the convolution operator, I^0 is an amplitude factor dependent on the scattering cross-section, and $\omega_B = 2\pi\nu_B$ and Γ_B represent the frequency position and the full width at half-maximum (FWHM) of the Brillouin peaks. In particular, the real part of the longitudinal elastic modulus of the sample at the frequency of the Brillouin peaks, M'(ω_B), is directly proportional to the squared frequency ν_B^2 . Representative examples of fitting curves are shown in Fig.6.17.

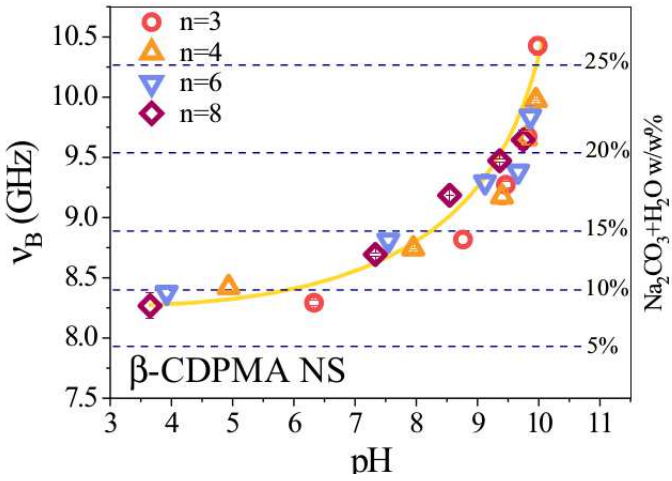

Figure 6.18: Brillouin frequency ν_B as a function of pH in samples of β-CDPMA1n (n = 3, 4, 6, 8) swollen at h = 4. The full line is a guide for the eyes. The values of ν_b measured for the solvent Na_2CO_3 + H_2O w/w % are reported in the same graph.

Fig.6.18 shows the dependence of ν_B on pH of the sample for PMA-based nanosponges. By comparison, the values of ν_B measured in the pure solvent are also reported, and a correlation with the amount of Na_2CO_3 in the solution is observed. However, different NS respond differently to the same solvent, and

a progressive increase of the Brillouin frequency appears indeed to be associated to the increasing value of pH in the samples, suggesting that they become progressively more rigid by passing from low to high pH. The picture emerging from this behaviour is that the higher the pH, the stronger the interconnections among NS domains, giving rise to an overall stiffer gel network. It is to be noted that according to BLS results, all types of PMA-based nanosponges exhibit a similar mechanical response under variation of pH, in agreement with information from SANS measurements revealing only a slight dependence of the structure on the molar ratio of the monomer constituents, n. A more

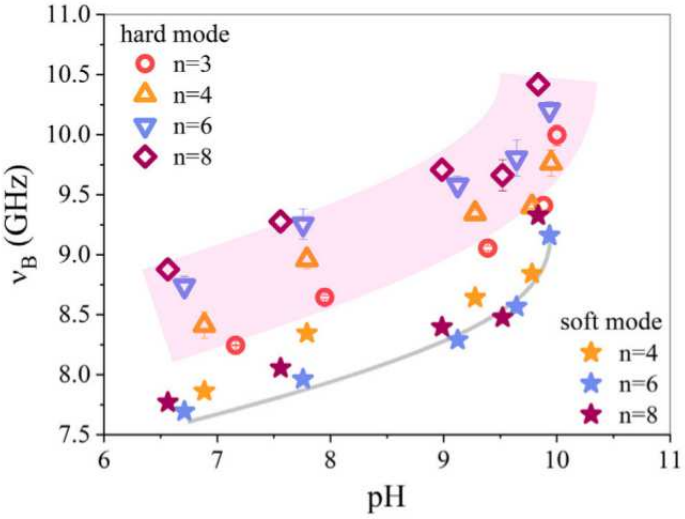

Figure 6.19: Brillouin frequency ν_B of the hard (open symbols) and soft mode (closed stars) in samples of β-CDEDTA1n (n = 3, 4, 6,8) swollen at h = 4. The pink coloured area covers the data of the hard mode; the solid line is a guide for the eyes running through the data of the soft mode.

complex scenario is found in the case of EDTA-based nanosponges. Fig.6.19 shows that the Brillouin frequency of both soft and hard acoustic mode shifts to higher values on increasing pH, similar to the behaviour observed in PMA-based nanosponges. The two modes, however, differ in their dependence on the composition of the polymer network, with the hard mode being significantly affected by a change of the parameter n and the soft mode being almost independent of it. This provides a clear indication that the hard and soft modes are associated tthe propagation of phonons in polymer- and solvent-rich en-

vironments, respectively. Such heterogeneity on the length scale probed by BLS is lost in the sample with $n = 3$ in which, as in the case of PMA-based nanosponges, only one mode is detected. Interestingly, in this case the pH dependence of the Brillouin frequency is very close to that found in PMA-NS. By comparison with the results of SANS experiments (see Fig.6.15), we note that heterogeneities on a micrometric length-scale are only revealed by BLS in hydrogels characterized by a mesh-size larger than $\sim 15\mathring{A}$, suggesting that the microscopic factors responsible for differences in the internal structure of NS domains also determine the interactions between them, responsible for the macroscopic hydrogel structure. Therefore, BLS provides an elastic characterization of the investigated systems coherent with their structural features.

UV Raman spectroscopy measurements As shown in previous works [269, 281, 297], UV Raman spectroscopy can be efficiently used for investigating water-polymer interactions in NS hydrogels in different experimental conditions. Here, we focus the attention on the high-wavenumber region of the Raman spectrum (2800-3800 cm^{-1}) that includes the CH stretching signals of EDTA-NS (2800-3000 cm^{-1}) as well as the OH stretching band of water (3000-3800 cm^{-1}), a particularly sensitive probe for the H-bond organization of water [268, 298–300]. The spectral analysis was carried out on β-CDEDTA18, as a representative NS sample, to gain structural information on the polymer matrix and on the water embedded in it. Fig.6.20 displays the resulting Raman spectra obtained for β-CDEDTA18 samples at different hydration levels. For the sake of comparison, the spectra were normalized to the maximum intensity of the OH stretching band at $\approx$3400 cm^{-1} . The CH signals of EDTA-NS polymer can be clearly seen between 2800 and 3100 cm^{-1}. The spectral contributions to the OH stretching band arising from the polymer OH groups can be safely neglected, as suggested by comparing the spectra of dry and hydrated NS samples. The Raman spectrum of the solvent (blue line in Fig. 7) evidences the presence of the three distinct components at $\omega_1 \approx 3200$, $\omega_2 \approx 3450$ and $\omega_3 \approx 3600$ cm^{-1} typical of water. Following a common interpretation [229, 232, 298, 301], the lowest wavenumber component refers to collective in-phase vibrations due to water molecules locally arranged in ordered *ice-like* tetrahedral configurations [229, 301]; the intermediate con-

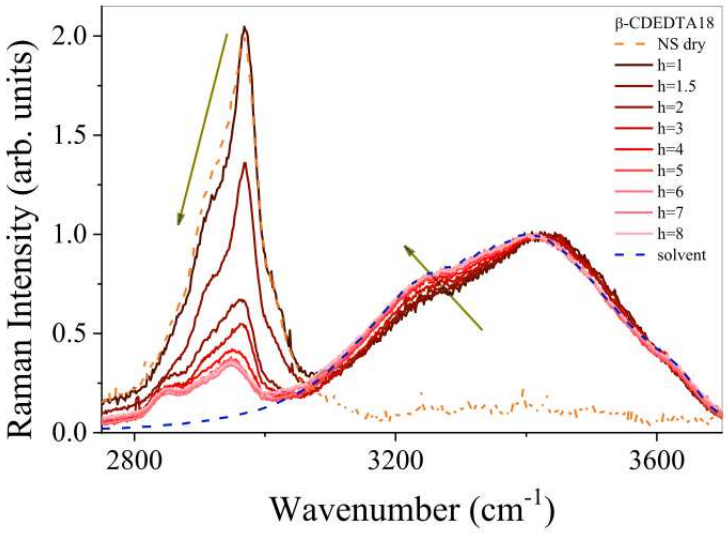

Figure 6.20: UV Raman spectra collected on β-CDEDTA18 gel swollen at increasing hydration value h and at fixed pH $\approx$ 9. The arrows indicate the increasing of hydration h. The spectra of pure solvent and of dry NS are reported in the same panel for comparison.

tribution is associated to water structures where H-bonds are partially elongated and/or distorted [301] and phase correlations among nearest oscillators vanish; the shoulder at higher wavenumbers is assigned to OH groups not involved (as H-donors) in H-bonds. To notice that these latter may be described as short-living species that transiently form during the H-bond rearrangement dynamics [232]. As it appears in Fig.6.20, the shape of OH stretching band in the spectrum of the β-CDEDTA18 gel hydrated at h = 1 differs significantly from that of the pure solvent. This finding suggests that the intermolecular structure of water in the compartmentalized spaces of the hydrogen network is different from the bulk water, in agreement with what already observed in other gel systems [268, 298–300]. In particular, the spectra in Fig.6.20 point out an overall blue-shift of the OH distribution on going from the pure solvent to the hydrogel at h = 1, together with a marked decrease of the ice-like component at about 3200 cm^{-1} . This clearly indicates that water hydrating the EDTA-NS matrix has partially lost its tetrahedral organization typical of the bulk. The observed destructuring effect on the interfacial water can be mainly attributed to the EDTA cross-linker, considering that β-CDs barely

affect the structure of water even at relatively high concentrations [74], and/or to a less specific confinement effect. Fig.6.20 also highlights that with the growth of the hydration level the distribution approaches to that of pure water, reflecting the increase of the population of bulk-like environment during the swelling process. The shape of the OH band in nanosponges swollen at h $>$ 5-7 and in the pure solvent practically coincides (see Fig.6.20), suggesting that, for high swelling degrees, the fraction bulk-like water is dominating and it is not significantly perturbed by the interaction with the polymer backbone. A similar behavior was reported for other gel systems [268, 299]. Interestingly, with the increase of h, relevant changes of the features of the CH signals can be also observed, indicating modifications on the intermolecular interactions experienced by the CH groups upon swelling. The spectral changes were quantified by a curve-fitting procedure [74, 233–235]. In particular, the OH distribution was reproduced considering three distinct components: a mixed Gaussian-Lorentzian form for the ice-like contribution ($\omega_1 \approx 3200$ cm^{-1}) and two Gaussian profiles for the contributions arising from water molecules involved in distorted configurations and H-bond-free OH groups ($\omega_2 \approx 3450$ and $\omega_1 \approx 3600$ cm^{-1}), respectively [74, 234]. During the fitting procedure, the widths of the three components was fixed to the values obtained for pure water [74], while three Voight functions were considered for reproducing the CH stretching signals. Even if various decomposition procedures have been proposed to describe OH band features [74, 229, 232–235, 237, 301], here we employed a relatively simple scheme that involves the minimum number of components needed to reproduce the distribution. This method, in which a reduced number of parameters are considered, has proved to be convenient for comparison ends [74, 234]. An example of fitting result is displayed in Fig.6.21 for the case of β-CDEDTA18 gel hydrated at h = 4 and at pH = 9.8. In order to quantify spectral changes, the quantity *C(h,pH)* (see eqn.6.1) was considered. This quantity is related to the fraction of OH groups involved in ordered ice-like configurations [74, 229, 233–235, 237]. As reported in Fig.6.22(a), for low h values (h = 1-1.5), the value of C is significantly lower compared to that of the pure solvent, suggesting that, at these hydration levels, the interactions with the polymer groups affect the tetrahedral ordering of a large fraction of water present into the NS matrix. It might be expected that the formation of

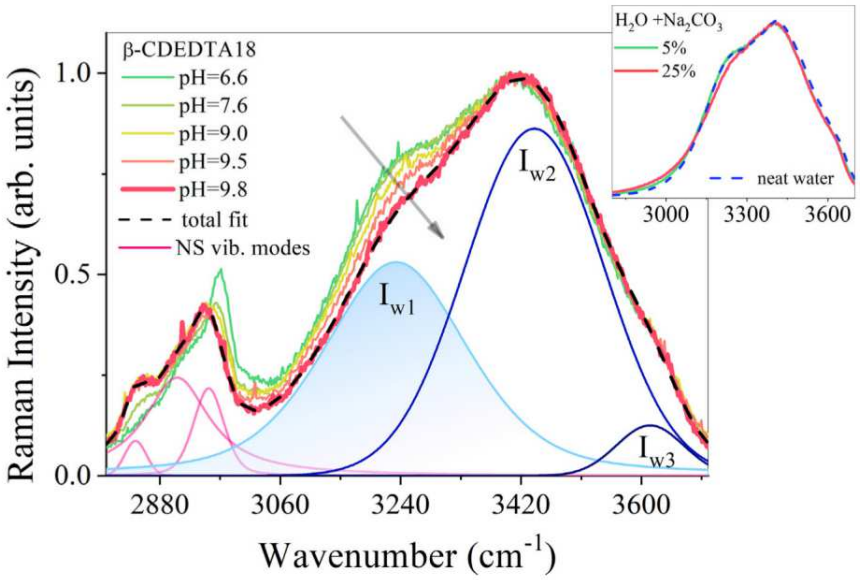

Figure 6.21: pH-evolution of UV Raman spectra collected on β-CDEDTA18 gel swollen at fixed value of hydration h = 4. The arrows indicate the increasing of pH measured in the gel phase. An example of best fitting result obtained for the experimental profile corresponding to the β-CDEDTA18 gel at pH = 9.8 (red line) is reported in the same panel with the single components assigned to the vibrational modes of NS and to the OH stretching components of water. Inset: comparison between the spectra of neat water and of the solution H_2O + Na_2CO_3 at 5 and 25% w/w.

H-bonds between water and carboxylate anions [285] would play an important role in the destructuring of the ice-like configurations typical of bulk water. Fig.6.22(a) points out that C increases with the hydration degree up to h = 4 ÷ 5, reaching a plateau corresponding to the value of the pure solvent. In a consistent way, the data from BLS collected on the same sample showed the presence of a "solvent rich" contribution to soft acoustic mode shift. This parallelism between the atomistic description of Raman spectroscopy and the long-range organization explored by BLS is of interest for the overall picture of the material's properties. Starting from h = 1, the addition of water leads to a progressive swelling of the NS matrix with a corresponding increase of the fraction of bulk water within the system. Likely, the full swelling is attained for h = 4 ÷ 5, when most of water shows a bulk-like structure; no further variations of C are then observed for h > 5, probably due to sensitivity rea-

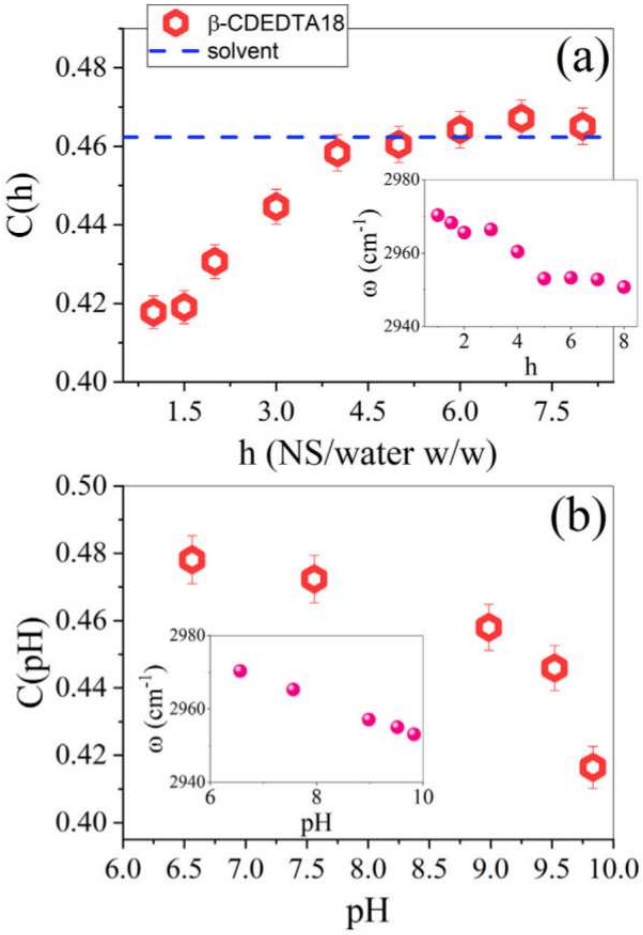

Figure 6.22: (a) Hydration-dependence of parameter C for β-CDEDTA18 gel swollen at fixed pH $\approx$ 9. The dashed line represents the value of C obtained for the solvent used for hydrating NS. Inset: h-dependence of the frequency position of the most intense mode at about 2970 cm^{-1} of NS. (b) pH-dependence of C for β-CDEDTA18 gel swollen at fixed h = 4. Inset: pH-evolution of the frequency position of the most intense mode at about 2970 cm^{-1} of NS.

sons. The peak position of the CH band of EDTA-NS polymer found at about 2970 cm^{-1} decreases significantly just up to h = 5 (inset of Fig.6.22(a)), with minor changes for higher hydration levels. This supports the idea that major structural modifications on the NS network occur in the h = 1-5 range. The effect of pH on the spectral distribution of the NS hydrogels (β-CDEDTA18) swollen at a fixed hydration level (h = 4) can be clearly observed in Fig.6.21.

The features of the CH stretching signals change by increasing pH, with variations qualitatively similar to those induced by increasing hydration degree. In fact, as shown in the inset of Fig.6.22(b), a continuous red shift is observed for the CH band at 2970 cm^{-1} as the pH increases, which could be interpreted as a signature of a progressive modification on the overall structure of the polymer network promoted by the pH variation. While this progressive phenomenon seems to be uncorrelated with the variation of the mesh-size ζ detected by SANS experiments for pH>8 (Fig.6.16), it might be connected to the modulation on the elastic properties probed by BLS (Fig.6.19). The pH increase is also accompanied by a significant destructuring of the tetrahedral organization of water, as testified by the depletion of the ice-like component (3200 cm^{-1}) of the OH band (see spectra reported in Fig.6.21). In fact, a noticeable reduction of C(pH) can be observed in Fig.6.22(b), especially evident for high pH values. This can be only partially ascribed to the increasing concentrations of Na_2CO_3 in the system that, as shown in the inset of Fig.6.21, causes a quite modest destructuring effect on pure water. Rather, it might be explained considering an overall increase of the solvent-exposed area of the polymer surface, as a consequence of pH-induced structural changes and/or the increase of ionic sites in the system, such as -COO^- groups of the cross-linker, with inherent destructuring character [285]. It is likely that the water taken up during the swelling process is mainly stored in the pores of nanosponges, whose average size is estimated by the correlation length ζ, and the intermolecular structure of these solvent molecules shows a relatively higher probability of H- bond defects than those of the bulk. The presence of spatial inhomogeneities on a scale of about tens of nm, revealed by SANS measurements [279], suggests that a fraction of the water molecules permeates the interstices among NS domains where the interaction with the polymer surface is probably slighter, thus favouring the formation of H-bonds structures similar to those formed in the free solvent, as revealed by the Raman analysis. The increase of pH promotes a switch in the characteristic size of the hydrophilic pores in those NS hydrogels where the cross-linker has a well defined acid-base property (EDTA-NS). The structural changes are accompanied by important molecular and viscoelastic modifications of the hydrogel system, reflected by a larger orientational disorder induced on the H-bond of water molecules and by an overall increased

stiffness of the gel network observed at high pH. These changes can definitively clarify the origin of the improved water uptake capability shown by NS in basic conditions [281, 297].

Conclusion

The results reported in this PhD thesis highlights the advantages of synchrotron-based UV Resonance Raman scattering technique for the investigation of intermolecular interactions in ionic liquid/water mixtures and of their solvation properties towards biological molecules. In particular, we can summarize the main results as it follows:

Chapter 3: the comparison between UVRR and spontaneous Raman spectra of ILs discussed in the chapter underlines how the unique tunability of SR in the UV range allows the selective enhancement of the vibrational signals arising from cations of ILs. We have recognized in the UV-resonance spectra some spectroscopic signals that are markers of the molecular reorganization of cation/anion domains induced by the presence of water molecules. At the same time, UVRR technique turned out to be particularly informative in probing the H-bond rearrangement of water network inside water-rich nano-domains known as water pockets.

Chapter 4: The solvation dynamics of small peptides has been studied by putting in evidence on the advantages of the use of SR-based UVRR scattering. The analysis of the spectra confirms that the UVRR cross sections and frequencies of amide bands can be used as strongly sensitive spectroscopic markers for probing the interactions between the amide backbone and the surronding solvent molecules in the presence of IL.

Chapter 5: The conformational stability of DNA in the presence of ILs has been investigated at molecular level thanks to the selectivity offered by SR-UVRR spectroscopy. The tunability of UV source has allowed to enhance specific vibrational signals associated to nitrogenous bases of DNA, through an appropriate tuning of the excitation wavelength. Such approach permitted

to probe the rearrangements of interactions in the local environment around specific nucleotides as a function of thermal denaturation. As main result, we observed a stabilizing effect on the natural conformation of DNA induced by the presence of imidazolium-based ionic liquids, in agreement also with some theoretical investigations reported in literature.

Chapter 6: UVRR scattering has been used in joint combination with Small Angles Neutron Scattering and Brillouin experiments to describe hydrophobic/hydrophilic effects in hydration water for different environments. The case of hydrophilic sugar solutes and polisaccharide hydrogels have been discussed. The reported results put in evidence the usefulness of a multitechnique approach to provide a picture of the intermolecular ordering of water due to solvent-solute interactions.

All these results corroborate the great potentiality of UV Raman spectroscopy to retrieve information on the intermolecular interactions in hydrated systems.

Acknowledgments

Undertaking this PhD would not have been possible without the support and guidance that I received from many people.

I would like to express my sincere gratitude to my supervisor Dr. Claudio Masciovecchio, whose office door was always open whenever I had some questions about my research. He consistently allowed this manuscript to be my own work, but steered me in the right direction whenever he thought I needed it.

My great and sincere thanks go to my co-supervisor Dr. Barbara Rossi: she represents a mentor for my Ph.D path and her patient guidance helped me in all the time of research and writing of this thesis. The joy and enthusiasm she has for the research was contagious and motivational for me, making my Ph.D. experience productive and stimulating. I am also thankful for the excellent example she has provided as a successful scientist and person.

Many thanks also to all the staff of IUVS BeamLine @ Elettra-Sincrotrone Trieste and in particular to Alessandro Gessini for his incessant assistance. I appreciated very much his enthusiasm, intensity, willingness and immense knowledge. Without his passionate participation and input, my Ph.D progect could not have been conducted. I have been lucky enough to have a chance to spend my Ph.D activity in this research group.

I gratefully acknowledge Sara Catalini for providing me with unfailing support and continuous encouragement throughout my years of study and through the process of researching and writing this thesis and for all the fun we have had in the last three years.

Finally, I express very profound gratitude to the below mentioned scientists for their insightful comments, but also for the hard questions which incented

me to widen my research from various perspectives: Prof. Andrea Mele, Prof. Marco Paolantoni, Prof. Ines Mancini, Dr. Alessandro Damin, Prof. Alessandro Paciaroni, Dr. Riccardo Mincigrucci, Dr. Riccardo Cucini, Dr. Almasy Laszlo, Dr. Diego Perinelli, Dr. Dan Dimitrescu and Dr. Andrea Fiorati.

This accomplishment would not have been possible without all of them. Thank you.

Appendix A

Small Angle Neutron Scattering, basic relations

Small angle neutron scattering (SANS) is a neutron technique able to probe structures at length scales from around 1 nanometre to more than 100 nanometres. It has a wide range of applications from studies of polymers, precipitates in metallurgical specimens, biological molecules, micelles and magnetic systems like ferrofluids. Small angle scattering (SAS) is the collective name given to the techniques of SANS, X-ray (SAXS) and light (SALS, or just LS) scattering. In each of these techniques radiation is elastically scattered by a sample and the resulting scattering pattern is analysed to provide information about the size, shape and orientation of some component of the sample. Neutron scattering has an advantage over X ray scattering due to selective absorption and scattering cross section of neutrons across the periodic table.

In general, neutron scattering is a process of collision between neutrons emitted by a source and a target which is the studied sample. When the scattering angles of these collisions are very small, the emitted neutrons are very close to the axis of the emerging beam. This process is thus referred to as SANS. The momentum exchange between the direction of the scattered neutron and the direction fo the initial beam can be expressed as:

$$\hbar q = \frac{4\pi\hbar}{\lambda}\sin(\theta/2) \tag{A.1}$$

where θ is the scattering angle, λ is the wavelength of the neutron, and q is

the amplitude of the scattering vector. Using neutrons with wavelenghts in the range of 4-20 $\mathring{A}$, permits to cover a q-range usually between 0.001 and $1\mathring{A}^{-1}$. Measurements at lower angles are limited by experimental difficulties while at higher angles it is possible to go out of the proper small angle scattering measurement, and other features of the structure become visible. Such momentum exchange permits to study the structure at length scales from one nanometer up to few hundreds of nanometers. The structural arrangement of the nuclei are correlated with the q-dependence of the scattering, being the former the space-Fourier transformation of the momentum exchange dependence of the scattering intensity. The length scales reached in small angle neutron scattering experiments do not permit to distinguish the individual atoms. Therefore, the quantity measured is the distribution of the scattering length $\rho_{sc.l}$. This quantity is defined as the ratio of the sum of the scattering lengths b_i of all nuclei to the volume V they are contained in:

$$\rho_{sc.l} = \frac{1}{V}\sum_i b_i \tag{A.2}$$

Correlation length is a useful quantity to characterize the spatial extension of inhomogenities inside a sample. In samples like compressible liquids close to the critical point or in two-component molecular mixtures, it is possible to describe the scattering length distribution using the Debye equation:

$$\langle(\rho_{sc.l}(r) - \rho_{average})^2\rangle^{1/2} \sim \frac{1}{r}exp(-r/\xi) \tag{A.3}$$

in which ξ indicates the correlation length. This quantity is roughly a distance up to which the correlation between the fluctuations of the local density extends. The corresponding scattering intensity is called Ornstein-Zernike formula [187]:

$$I(q) = \frac{I(0)}{1 + q^2\xi^2}. \tag{A.4}$$

It has the form of a Lorentzian function, resulting from the Fourier transform scattering length density distribution. The Ornstein-Zernike formula can be used for a graphical determination of the correlation length and of the scattering intensity at zero angle. At large values of the scattering vector the intensity decays proportionally to q^2.

List of Papers

- V. Crupi, V. Allodi, C. Bottari, F. D'Amico, G. Galli, A. Gessini, M.F.La Russa, F. Longo, D. Majolino, G. Mariotto, C. Masciovecchio, A. Pezzino, B. Rossi, S.A. Ruffolo, V. Venuti, "Spectroscopic investigation of Roman decorated plasters by combining FT-IR, micro-Raman and UV-Raman analyses Vibrational Spectroscopy", **83**, 78-84 (2016).

- C. Bottari, G. Mirocle Crisci, V. Crupi, V. Ignazzitto, M. F. La Russa, D. Majolino, M. Ricca, B- Rossi, S. A. Ruffolo, Jo. Teixeira, V. Venuti, "SANS investigation of the salt-crystallization- and surface-treatment-induced degradation on limestones of historic–artistic interest", Appl. Phys. A, 122-721 (2016).

- C. Bottari, L. Comez, S. Corezzi, F. D'Amico, A. Gessini, A. Mele, C. Punta, L. Melone, A. Pugliese, C. Masciovecchio, B. Rossi,"Correlation between collective and molecular dynamics in pH-responsive cyclodextrin-based hydrogels", Phys. Chem. Chem. Phys. **19**, 225557 (2017).

- C. Bottari, L. Comez, M. Paolantoni, S. Corezzi, F. D'Amico, A. Gessini, C. Masciovecchio, B. Rossi, "Hydration properties and water structure in aqueous solutions of native and modified cyclodextrins by UV Raman and Brillouin scattering", J Raman Spectrosc., **49**, 1076-1085 (2018).

- V. Crupi, M. F. La Russa, V. Venuti, S. Ruffolo, M. Ricca, G. Paladini, R. Albini, A. Macchia, L. Denaro, G. Birarda, C. Bottari, F. D'Amico, L. Vaccari, D. Majolino, "A combined SR-based Raman and Infrared investigation of pigmenting matter used in wall paintings: The San Gennaro and San Gaudioso Catacombs (Naples, Italy) case", The Eu. Phys. Journal **133** (9), 369 (2018).

- B. Rossi, C. Bottari, L. Comez, S. Corezzi, M. Paolantoni, A. Gessini, C. Masciovecchio, A. Mele, C. Punta, L. Melone, A. Fiorati, A. Radulescu, G. Mangiapia, A. Paciaroni, "Structural and molecular response in cyclodextrin-based pH-sensitive hydrogels by the joint use of Brillouin, UV Raman and Small Angle Neutron Scattering techniques", Journal of Molecular Liquids **271**, 738-746 (2018).

- S. Di Fonzo, C. Bottari, J. W. Brady, L. Tavagnacco, M. Caterino, L. Petraccone, J. Amato, C. Giancola, A. Cesàro, "Crowding and conformation interplay on human DNA G-quadruplex by ultraviolet resonant Raman scattering", Phys. Chem. Chem. Phys. **21** (4), 2093-2101 (2018).

- B. Rossi, S. Catalini, C. Bottari, A. Gessini, C. Masciovecchio, "Frontiers of UV resonant raman spectroscopy by using synchrotron radiation: the case of aqueous solvation of model peptides", Proc. SPIE 11086, UV and Higher Energy Photonics: From Materials to Applications 2019, 110860N (9 September 2019); doi: 10.1117/12.2529172.

- C. Bottari, I. Mancini, A. Mele, A. Gessini, C. Masciovecchio, B. Rossi, "Conformational stability of DNA in hydrated ionic liquid by synchrotron-based UV resonance raman", Proc. SPIE 11086, UV and Higher Energy Photonics: From Materials to Applications 2019, 110860Q (9 September 2019); doi:10.1117/12.2529077

- C. Bottari, B. Rossi, A. Mele, A. Damin, S. Bordiga, M. Musso, A. Gessini, C. Masciovecchio, "Synchrotron-based UV Resonance Raman Scattering for investigating Ionic liquid-water solutions", Cond. Matt. Phys., **22 (4)**, 2019.

- B. Rossi, C. Bottari, S. Catalini, F. D'Amico, A.Gessini, C. Masciovecchio, in Molecular and Laser Spectroscopy - Advances and Applications Volume 2, in press

List of Conferences

- Materials IT 2016
  12-16/12/2016 Catania (Italy)
  Oral Communication :"Pre-Resonant enhancement of amide Raman bands in peptides as revealed by tunable Raman scattering experiments"
  Oral Session: Thermo-activated solvation Mechanism in stimuli-responsive cyclodextrin-based hydrogels.

- Frontiers in water Biophysics 2017
  23-27/05/2017 Erice (Italy)
  Oral communication: "Hydrogen-bond rearrangement in cyclodextrin aqueous solutions probed by UV Raman and Brillouin Scattering".

- GISR 2017
  07-09/06/2017 Trieste (Italy)
  Oral communication: "Thermodynamic hydration shell behaviour of cyclodextrin aqueous solutions".

- 8th International Discussion Meeting on Relaxations in Complex Systems
  23-28/07/2017 Wisla (Poland)
  Oral communication: "Structural dynamics of hydration water in cyclodextrin aqueous solutions".

- FISMAT2017 – Italian National Conference on the Physics of Matter
  01-09/10/2017 Trieste (Italy)
  Oral communication: "Hydration properties of native and modified cyclodextrin: an UV Raman and Brillouin scattering study".

- Water X: exotic properties of water under extreme conditions
  03-08/06/18 La Maddalena (Italy)
  Oral communication: "Solvation mechanism in Ionic Liquid – water mixtures: a theoretical and experimental UV Raman investigation".

- 27^{th} Conference on Molten Salts and Ionic Liquids – EuCheMSIL 2018
  07-13/10/18 Lisbon (Portugal)
  Oral communication: "Hydrogen-bond rearrangement in imidazolium based Ionic Liquid – water mixture".

- Frontiers in Water Biophysics 2019
  21-26/07/19 Erice (Italy) Oral communication: "Biophysical properties of DNA in ionic liquid probed by UV- Resonance Raman Scattering".

- SPIE. Optics+Photonics
  11-15/08/19 San Diego, California, (USA) Oral communication: "Conformational stability of DNA in ionic liquids by synchrotron-based UV Resonant Raman".

- EMLG 2019
  08–13/09/19, Kutná Hora (Czech Republic) Oral communication: "Synchrotron-based UV Resonance Raman Scattering for investigating structural dynamics of hydrogen-bond in ionic liquids-water mixtures".

List of Figures

List of Tables

Bibliography

[1] D. A. Long, Raman spectroscopy. Great Britain: McGraw-Hill, 1977.

[2] D. A. Long, The Raman Effect: A Unified Treatment of the Theory fo Raman Scatteing by Molecules, John Wiley & Sons Ltd., 2002.

[3] F. D'Amico, M. Saito, F. Bencivenga, M. Marsi, A. Gessini, G. Camisacca, E. Principi, R. Cucini, S. Di Fonzo, A. Battistoni, E. Gangrisostomi, C. Masciovecchio, Nucl. Instrum. Meth. Phys. A **703** (2013).

[4] T. Tanaka, H. Kitamura, Nucl. Instrum. Meth. Phys. A **364** (1995).

[5] B. Diviacco, R. Bracco, D. Millo, D. Zangrando, Proceedings of the Eight European Particle Accelerator Conference, European Physical Society, Paris, 2610 (2002).

[6] C. Masciovecchio, S. C. Santucci, A. Gessini, S. Di Fonzo, G. Ruocco, F. Sette, Phys. Rev. Lett. **92**, 255507 (2004).

[7] H. Hiramatsu, T. Saito, J. Raman Spectrosc. **45**, 208-210 (2014).

[8] W. Kiefer, H. J. Bernstein, Appl. Spectrosc. **25**(6), 609-613 (1971).

[9] Seddon R., J. Chem. Tech. Biotechnol. **68**, 351-356 (1997).

[10] T. Welton, Chem. Rev. **99**, 2071-2084 (1999).

[11] J. P. Hallett, T. Welton, Chem. Rev. **111**(5), 3508-3576 (2011).

[12] D. R. MacFarlane, J. M. Pringle, P. C. Howlett, M. Forsyth, Phys. Chem. Chem. Phys. **12**, 1659-1669 (2010).

[13] M. Armand, F. Endres, D. R. MacFarlane, H. Ohno, B. Scrosati, Nat. Mater. **8**, 621-629 (2009).

[14] W. Xu, C. A. Angel, Science **302**, 422-425 (2003).

[15] T. Welton, Coord. Chem. Rev. **248**, 2459-2477 (2004).

[16] T. L. Greaves, C. J. Drummond, Chem. Rev. **108**, 206-237 (2008).

[17] P. Wasserscheid, T. Welton, Eds. Wiley-VCH: Weinheim, 1 (2008).

[18] N. V. Plechkova, K. R. Seddon, In: Methods and Reagents for Green Chemistry, Chap. 5, P. Tundo, A. Perosa, F. Zecchini, (Eds.), U.S. Government Printing Office, Washington, D.C.(2007).

[19] G. Chatel, J. F. B. Pereira, V. Debbeti, H. Wang, R. D. Rogers, Green Chem. **16**, 2051 (2014).

[20] H. Rodriguez, J. F. Brennecke, J. Chem. Eng. Data **51**, 2145-2155 (2006).

[21] V. L. Martins, B. G. Nicolau, S. M. Urahata, M. C. C. Ribeiro, R. M. Torresi, J. Phys. Chem. B **117**, 8782-8792 (2016).

[22] N. Kaftzik, P. Wasserscheid, U. Krag, Org. Proc. Res. Dev. **6**, 553-557 (2002).

[23] Y. Kohno, N. O. H. Nakamura, Australian Journal of Chemistry **65**, 1548-1553 (2012).

[24] K. S. Egorova, E. G. Gordeev, V. P. Ananikov, Chem. Rev. **117**(10), 7132-7189 (2017).

[25] H. Zhoi, Chem Technol Biotechnol, **91**, 25-50 (2016).

[26] R. J. Lovelock, R. Soc. open sci. (2017).

[27] V. H. Paschoal, L. F. O. Faria, M. C. C. Ribeiro, Chem. Rev. **117**(10), 7053-7112 (2017).

[28] V. Mazzacurati, M. A. Ricci, G. Ruocco, M. Sampoli, Chem. Phys. Lett. **159**, Issue 4, 383-387 (1989).

[29] L. Cammarata, S. G. Kazarian, P. A. Salter, T. Welton, Phys. Chem. Chem. Phys. **3** (2001).

[30] M. Klaähn,, C. Stuüber, A. Seduraman, P. Wu, J. Phys. Chem. B. **114**, 2856-2868 (2010).

[31] T. Köddermann, C. Wertz, A. Heintz, R. Ludwig, Angew. Chem. Int. Ed. Engl. **45**, 3697-3702 (2006).

[32] J.M. Andanson, M. J. Beier, A. Baiker, J. Phys. Chem. Lett. **2**(23), 2959-2964 (2011).

[33] B. Fazio, A. Triolo, G. Di Marco, J. Raman Spectrosc. **39**, 233-237 (2008).

[34] V. Aleksa, J. Kausteklis, V. Klimavicius, Z. Gdaniec, V. Balevicius, J. Mol. Struct. **993**, 91-96 (2011).

[35] T. Takekiyo, Y. Imai, N. Hatano, H. Abe, Y. Yoshimura, Chem. Phys. Lett. **511**, 241-246 (2011).

[36] N. Yaghini, J. Pitawala, A. Matic, A. J. Martinelli, Phys. Chem. B **119**, 1611-1622 (2015).

[37] D. S. Caswell, G. S. Thomas, J. Am. Chem. Soc. **108**, 6470-6477 (1986).

[38] S. A. Asher, J. L. Murtaugh, Appl. Spectry., **42**, 83 (1988).

[39] M. Majoube, M. Henry, L. Chinsky, P. Y. Turpin, Chem. Phys. **169**, 231 (1993).

[40] L. M. Markham, L. C. Mayne, B. S. Hudson, J. Phys. Chem. **97**, 10319-10325 (1993).

[41] M. C. C. Ribeiro, J. Phys. Chem. B **116**, 7281-7290 (2012).

[42] Z. Wu, C. Zhang, P. C. Stair, Catal. Today **113**, 40-47 (2006).

[43] Z. Hong, S.A. Asher, Appl. Spectr. **69**, 75-83 (2015).

[44] R. Dovesi, A. Erba, R. Orlando, C. M. Zicovich-Wilson, B. Civalleri, L. Maschio, M. Rerat, S. Casassa, J. Baima, S. Salustro, B. Kirtman.; WIREs Comput Mol Sci. **8**, e1360 (2018).

[45] R. Dovesi, V. R. Saunders, C. Roetti, R. Orlando, C. M. Zicovich-Wilson, F. Pascale, B. Civalleri, K. Doll, N. M. Harrison, I. J. Bush, P. D'Arco, M. Llunell, M. Causà, Y. Noël, L. Maschio, A. Erba, M. Rerat and S. Casassa; CRYSTAL17 User's Manual (University of Torino, Torino, 2017).

[46] D. A. Carter, J. E. Pemberton, J. Raman Spectrosc. **28**, 939-946 (1997).

[47] C. Perchard, A. Novak, Spectrochim. Acta Part A, 23 (1953).

[48] J. Grondin, J. C. Lassegues, D. Cavagnat, T. Buffeteau, P. Johansson, R. Holomb, J. Raman Spectrosc. **42**, 733-743 (2011).

[49] S. A. Katsyuba, P. J. Dyson, E. E. Vandyukova, A. V. Chernova, A. Vidis, Helv. Chim. Acta **87**, 2556-2565 (2004).

[50] A. Dominguez-Vidal, N. Kaun, M. J. Ayora-Canada, B. Lendl, J. Phys. Chem. B **111**(17), 4446-4452 (2007).

[51] A. M. Bellocq, C. Garrigou-Lagrange, J. Chim. Phys. Physico-Chim. Biol. **66**, 1511 (1969).

[52] A. Mele, C. D. Than, S. H. De Paoli Lacerda, Angew. Chem. Int. Ed. **42**, 4364-4366 (2003).

[53] A. Triolo, O. Russina, H. J. Bleif, E. D. Cola, J. Phys. Chem. B **111**, 4641–4644 (2007).

[54] S. M. Urahata, M. C. C. Ribeiro, J. Chem. Phys. **120**, 1855–1863 (2004).

[55] Y. Wang, G. A. Voth, J. Am. Chem. Soc. **27**, 12192–12193 (2005).

[56] J. N. A. C. Lopes, A. A. H. Pàdua, J. Phys. Chem. B **110**, 3330–3335 (2006).

[57] Y. Khono, N. Nakamura, and H. Ohno, Australian J. Chem. **65**, 1548-1553 (2012).

[58] Y. Kohno, Y. Deguchi, and H. Ohno, Chem. Commun. **48**, 7119-7130 (2012).

[59] J. Bowers, C. P. Butts, P. J. Martin, M. C. Vergara-Gutierrez, Langmuir **20**, 2191–2198 (2004).

[60] L. Almasy, M. Turmine, A. Perera, J. Phys. Chem. B **112**, 2382-2387 (2008).

[61] K. Nishikawa, H. Hayashi, T. Iijima, J. Phys. Chem. **93**, 6559-6565 (1989).

[62] A. Wakisaka, S. Komatsu, Y. Usui, J. Mol. Liquids **90**, 175–184 (2001).

[63] T. Takamuku, M. Tabata, A. Yamaguchi, J. Nishimoto, M. Kumamoto, H. Wakita, T. Yamaguchi, J. Phys. Chem. B **102**, 8880–8888 (1998).

[64] T. Takamuku, T. Shimomura, K. Sadacane, H. Seto, Phys. Chem. Chem. Phys. **14**, 11070–11080 (2012).

[65] T. Takamuku, Y. Honda, K. Fujii, H. Kittaka, Anal. Sci. **24**, 1285–1290 (2008).

[66] T. Shimomura, K. Fujii, T. Takamuku, Phys. Chem. Chem. Phys. **12**, 12316–12324 (2010).

[67] N. A. Smirnova, A. A. Vanin, E. A. Safonova, I. B. Pukinsky, Y. A. Anufrikov, A. L. Makarov, J. Colloid Interface Sci. **336**, 793-802 (2009).

[68] N. A. Smirnova, E. A. Safonova, Russ. J. Phys. Chem. A **84**, 1695-1704 (2010).

[69] N. A. Smirnova, E. A. Safonova, Colloid J. **74**, 254–265 (2012).

[70] N. M. Vaghela, V. Sastry, V. K. Aswal, Colloid Polym. Sci. **289**, 309-322 (2011).

[71] L. Rosta, Appl. Phys. A **74**, 52-54 (2002).

[72] Y. Marechal, J. Mol. Struct. **322**, 105 (1994).

[73] M. E. Gallina, P. Sassi, M. Paolantoni, A. Morresi, R. S. Cataliotti, J. Phys. Chem. B **110**, 8856 (2006).

[74] C. Bottari, L. Comez, M. Paolantoni, S. Corezzi, F. D'Amico, A. Gessini, C. Masciovecchio, B. Rossi, J. Raman Spectrosc. **49**, 1076-1085 (2018).

[75] B. Bracco, Tesi di Laurea Magistrale in Scienze Chimiche, Università degli Studi di Perugia, AA. 2017/18.

[76] L.F. Scatena, M.G. Brown, G.L. Richmond, Science **292**, 908-912 (2001).

[77] Y. Yoshimura, T. Goto, H. Abe, Y. Imai, J. Phys. Chem. B **113**, 8091-8095 (2009).

[78] F. Franks, S. Mathias, [Biophysics of Water] Eds., John Wiley & Sons: Chichester (1982).

[79] S. K. Pal, J. Peon, B. Bagchi, A. H. Zewail., J. Phys. Chem. B **106**, 12376-12395 (2002).

[80] F. Garczarek, K. Gerwert, Nature **439**, 109-112 (2006).

[81] S. J. Kim, B. Born, M. Havenith, M. Gruebele, Angew. Chem. Int. Ed. **47**, 6486-6489 (2008).

[82] L. Zhang, Y. Yang, Y. T. Kao, L. Wang, D. J. Zhong, J. Am. Chem. Soc. **131**, 10677-10691 (2009).

[83] J. A. Rupley, G. Careri, Adv. Protein Chem. **41**, 37-172 (1991).

[84] R. S. Jakubek, S. E. White, S. A. Asher, J. Phys. Chem. B **123**(8), 1749-1763 (2019).

[85] D. Punihaole, R. S. Jakubek, E. M. Dahlburg, Z. Hong, N. S. Myshakina, S. Geib, S. A. Asher, J. Phys. Chem. B **119**, 3931-3939 (2015).

[86] A. V. Mikhonin, N. S. Myshakina, S. V. Bykov, S. A. Asher, J. Am. Chem. Soc. **127**, 7712-7720 (2005).

[87] L. Ma, Z. Ahmed, A. V. Mikhonin, S. A. Asher, J. Phys. Chem. B **111**, 7675-7680 (2007).

[88] K. Xiong, L. Ma, S. A. Asher, Biophys Chem. **162**, 1-5 (2012).

[89] S. A. Oladepo, K. Xiong, Z. Hong, S. A. Asher, J. Phys. Chem. Lett. **2**, 334-344 (2011).

[90] R. S. Jakubek, J. Handen, S. E. White, S. A. Asher, I. K. Lednev, Trends Anal. Chem. **103**, 223-229 (2018).

[91] A. V. Mikhonin, Z. Ahmed, A. Ianoul, S. A. Asher, J. Phys. Chem. B. **108**, 19020-19028 (2004).

[92] D. Russo, R. K. Murarka, J. R. D. Copley, T. J. Head-Gordon, J. Phys. Chem. B **109**, 12966-12975 (2005).

[93] D. Russo, G. L. Hura, J. R. D. Copley, Phys. Rev. E **75**, 040902 (2007).

[94] D. Russo, J. Ollivier, J. Teixeira, Phys. Chem. Chem. Phys. **10**, 4968-4974 (2008).

[95] D. Russo, J. Teixeira, J. Ollivier, J. Chem. Phys. **130**, 235101 (2009).

[96] S. Perticaroli, L. Comez, M. Paolantoni, P. Sassi, A. Morresi, D. Fioretto, J. Am. Chem. Soc. **133**, 12063-12068 (2011).

[97] S. Perticaroli, D. Russo, M. Paolantoni, M. A. Gonzalez, P. Sassi, J. D. Nickels, G. Ehlers, L. Comez, E. Pellegrini, D. Fioretto, A. Morresi, Phys. Chem. Chem. Phys. **17**, 11423-11431 (2015).

[98] S. Boopathi, P. Kolandaivel, J Biomol Struct Dyn. **31**, 158-173 (2013).

[99] B. Born, H. Weingartner, E. Bründermann, M. Havenith, J. Am. Chem. Soc. **131**, 3752-3755 (2009).

[100] L. Comez, S. Perticaroli, M. Paolantoni, P. Sassi, S. Corezzi, A. Morresi, D. Fioretto, Phys. Chem. Chem. Phys. **16**, 12433-12440 (2014).

[101] K. Mazur, I. A. Heisler, S. R. Meech, J. Phys. Chem. B **114**, 10684-10691 (2010).

[102] J. Qvist, B. Halle, J. Am. Chem. Soc. **130**, 10345-10353 (2008).

[103] Y. Sugawara, H. Matsuura, T. Shimanouch, J. Raman Spectrosc. **4**, 91-98 (1975).

[104] Y. Sugawara, I. Harada, H. Matsuura, T. Shimanouchi, Biopolymers. **17**, 1405-1421 (1978).

[105] X. G. Chen, P. Li, J. S. W. Holtz, Z. Chi, V. Pajcini, S. A. Asher, L. A. Kelly, J. Am. Chem. Soc. **118**, 9705-9715 (1996).

[106] X. G. Chen, S. A. Asher, R. Schweitzer-Stenner, N. G. Mirkin, S. Krimm, J. Am. Chem. Soc. **117**, 2884-2895 (1995).

[107] R. D. Jiji, G. Balakrishnan, Y. Hu, T. G. Spiro, Biochemistry **45**, 34-41 (2006).

[108] J. Shi, J. Wang, J. Phys. Chem. B. **118**, 12336-12347 (2014).

[109] S. Catalini, B. Rossi, P. Foggi, C. Masciovecchio, F. Bruni, J. Mol. Liq. **283**, 537-547 (2019).

[110] Z. Chi, S. A. Asher, Biochemistry **38**, 8196-8203 (1999).

[111] A. V. Mikhonin, S. V. Bykov, N. S. Myshakina, S. A. Asher, J. Phys. Chem. B **110**, 1928-1943 (2006).

[112] N. S. Myshakina, Z. Ahmed,S. A. Asher, J. Phys. Chem. B **112**, 11873-11877 (2008).

[113] E. S. Manas, V. Getahun, W. W. Wright, W. F. Degrado, J. M. Vanderkooi, J. Am. Chem. Soc. **122**, 9883-9890 (2000).

[114] S. A. Asher, A. V. Mikhonin, S. Bykov, J. Am. Chem. Soc. **126**, 8433-8440 (2004).

[115] M. E. Johnson, C. Malardier-Jugroot, R. K. Murarka, T. Head-Gordon, J. Phys. Chem. B **113**, 4082-4092 (2009).

[116] A. Benedetto, P.Ballone, ACS Sustainable Chem. Eng. **4**, 392-412 (2016).

[117] A. Benedetto, H. J. Galla, Biophys Rev. **9**(4), 279-281 (2017).

[118] K. S. Egorova, E. G. Gordeev, V. P. Ananikov, Chem. Rev. **117**, 7132-7189 (2017).

[119] S. N. Baker, A. Angell, Chem. Commun. 940-941 (2004).

[120] V. Zeindlhofer, C. Schröder, Biophysical Reviews **10**, 825-840 (2018).

[121] A. A. Tietze, F. Bordusa, R. Giernoth. D. Imhof, T. Lenzer, A. Maaβ, C. Mrestani-Klaus, I. Neundorf, K.Oum, D. Reith, A. Stark, ChemPhysChem **14**, 4044-4064 (2013).

[122] A. Richardt, C. Mrestani-Klaus, F. Bordusa, Journal of Molecular Liquids **192** 9-18 (2014).

[123] V. Govinda, P. Venkatesu, Ind. Eng. Chem. Res. **53**, 19628-19642 (2014).

[124] D.M. Townsend, K.D. Tew, H. Tapiero, Biomed. Pharmacother. **57**, 145-155 (2003).

[125] J. Sastre, F.V. Pallardo, J. Vina, Age (Omaha) **19**, 129-139 (1996).

[126] G. Jerzy, R. Roman, R. Jerzy, Folia Neuropathol. **42**, 203-207 (2004).

[127] D. Constantinescu, H. Weingärtner, C. Herrmann, Angew Chem Int Ed Engl. **46**, 8887-8889 (2007).

[128] Z. Yang, J Biotechnol. **144**, 12-22 (2009).

[129] B. Rossi, S. Catalini, C. Bottari, A. Gessini, C. Masciovecchio, Proc. SPIE 11086, UV and Higher Energy Photonics: From Materials to Applications 2019, 110860N

[130] Zhang, Y. Ma, Food Chem. **141**, 41-47 (2013).

[131] Y. Yoshikawa, Angew. Chem. **52**, 3712-3716 (2013).

[132] M. A. Kutzler, D. B. Weiner, Nat. Rev. Gen. **9**, 776-788, (2008).

[133] Y. Krishnan, F. C. Simmel, Angew. Chem. **50**, 3124-1256, (2011).

[134] R. C. Lord, G. J. Jr. Thomas, Developments in Applied Spectroscopy **6**, Plenum Press: NewYork (1968).

[135] M. Tsuboi, S. Takahashi, S. Muraishi, T. Kajiura, S. Nishimura, Science **174**, 1142-1144 (1971).

[136] S. C. Erfurth, E. J. Kiser, W. L. Peticolas, Proc. Natl. Acad. Sci. USA **69**(4), 938-941 (1974).

[137] W. L. Peticolas, W. L. Kubasek, G. A. Thomas, M. Tsuboi, In Biological Applications of Raman Spectroscopy **1**, Wiley: New York (1987).

[138] J. M. Benevides, S. A. Overman,G. J. Thomas, J. Raman Spectrosc. **36**, 279–299 (2005).

[139] J. R. Perno, C. A. Grygon, T. G. Spiro, J. Phys. Chem. **93**, 5672-5678 (1989).

[140] S. S. Chan, R. H. Austin, I. Mukerji, T. G. Spiro, Biophys. J. **72**, 1512-1520 (1997).

[141] W. Hug, J. Tinoco, J. Am. Chem. Soc. **95**, 2803-2813 (1973).

[142] S. P. A. Fodor, T. G. Spiro, J. Am. Chem. Soc. **108**, 3198-3205 (1986).

[143] Z. Q. Wen, G. J. Thomas, Biopolymers **45**(3), 247-256 (1998).

[144] S. A. P. Fodor, R. P. Rava, T. R. Hays, T. G Spiro, J. Am. Chem. Soc. **107**, 1520-1529 (1985).

[145] F. Bianchi, L. Comez, R. Biehl, F. D'Amico, A. Gessini, A. M. Longo, C. Masciovecchio, C. Petrillo, A. Radulescu, B. Rossi, F. Sacchetti, F. Sebastiani, N. Violini, A. Paciaroni, NAR **46**(22), 11927-11938, (2018).

[146] E. Westhof, Annu. Rev. Biophys. Bio. **7**, 125-144 (1988).

[147] W. Saenger, Annu. Rev. Biophys. Bio. **16**, 93-114 (1987).

[148] G. Bonner, A. M. Klibanov, Biotechnol. Bioeng. **68**, 339-344, (2000).

[149] J. G. Duguid, V. A. Bloomfield, J. M. Benevides, G. J. Thomas, Biophysical Journal **71**, 3350-3360 (1996).

[150] S. C. Erfurth, W. I. Peticolas, Biopolymers **14**, 247-264 (1975).

[151] L. Movileanu, J. M. Benevides, G. J. Thomas, Journal of Raman Spectroscopy **30**, 637 (1999).

[152] L. Rimai, V. M. Maher, D. Gill, I. Salmeen, J. J. McCormick, Biochimica et Biophysica Acta **361**, 155-165 (1974).

[153] I. Mukerji, A. P. Williams, Biochemistry **41**, 69-77 (2002).

[154] B. Tomlinson, W. L. Peticolas, The Journal of Chemical Physics **52**, 2154 (1970).

[155] S. A. Asher, Anal. Chem. **65**(2), 59A-66A (1993).

[156] B. R. Wood, Chem. Soc. Rev. **45**(7), 1980-1988 (2016).

[157] P. Zucchiatti, K. Latella, G. Birarda, L. Vaccari, B. Rossi, A. Gessini, C. Masciovecchio, F. D'Amico, J. Raman Spectrosc. **49**(6), 1-10 (2018).

[158] M. Banyay, M. Sarkar, A. Gräslund, Biophys. Chem. **104**(2), 477-488 (2003).

[159] M. Lukin, C. de Los Santos, Chem. Rev. **106**, 607-686 (2006).

[160] A. Arcella G. Portella, R. Collepardo-Guevara, D. Chakraborty, D. J. Wales, M. Orzoco, J. Phys. Chem. B **118**(29), 8540-8548 (2014).

[161] N. Singh, M. Sharma, D. Mondal, M. M. Pereira, K. Prasad, ACS Sustainable Chem. Eng. **5**, 1998-2015 (2017).

[162] N. Nishimura, Y. Nomura, N. Nakamura, H. Ohno, Biomaterials **26**, 5558-5563 (2005).

[163] J. H. Wang, D. H. Cheng, X. W. Chen, Z. Du, Z. L. Fang, Anal. Chem. **79**, 620-625 (2007).

[164] R. S. S. de Zoysa, D. A. Jayawardhana, Q. T. Zhao, D. Q. Wang, D. W. Armstrong, J. Phys. Chem. B **113**, 13332-13336 (2009).

[165] R. Vijayaraghavan, A. Izgorodin, V. Ganesh, M. Surianarayanan, D. R. MacFarlane, Angew. Chem. **49**, 1631-1633 (2010).

[166] A. Chandran, D. Ghoshdastidar, S. Senapati, J. Am. Chem. Soc. **134**, 20330-20339 (2012).

[167] K. Jumbri, M. B. Abdul Rahman, E. Abdulmalek, H. Ahmad,N. Micaelo, Phys. Chem. Chem. Phys. **16**, 14036-14041 (2014).

[168] C. Mukesh, D. Mondal, M. Sharma, K. Prasad, Chem. Comm. **49**, 6849-6851 (2013).

[169] Y. Ding, L. Zhang, J. Xie, R. Guo, J. Phys. Chem. B **114**, 2033-2043 (2010).

[170] Y. Hea, Y. Shanga, Z. Liua, H. Shaob, H. Liua, Y. Hu, Colloids and Surfaces B: Biointerfaces **101**, 398-404 (2013).

[171] I. Tinoco, J. Am. Chem. Soc. **82**, 4785, (1960).

[172] P. Sassi, A. Gugliarelli, M. Paolantoni, A. Morresi, G. Onori, Biophyis. Chem. **158**, 46-53 (2011).

[173] J. G. Duguid, V. A. Bloomfield, J. M. Benevides, G. J. Thomas, Biophys. J. **69**, 2623-2641 (1995).

[174] Y. Nishimura, M. Tsuboi, T. Sato, K. Akoi, J. Mol. Struct. **146**, 123-153 (1986).

[175] J. M. Benevides, M. A. Weiss, G. J. Thomas Jr., Biochemistry **30**, 4381-4388 (1991).

[176] J. G. Duguid, V. A. Bloomfield, J. M. Benevides, G. J. Thomas Jr., Biophys. J. **65**, 1916-1928 (1993).

[177] A. V. Lukashin, A. V. Vologodskii, M. D. Frank-Kamenetskii, Y. L. Lyubchenko J. Mol. Biol. **108**, 665-682 (1976).

[178] A. M. J. J. Bonvin, M. Sunnerhagen, O. G., J. Mol. Biol. **282**, 859-873 (1998).

[179] D. S. Studdert, M. Patroni, R. C. Davis, Biopolymers **11**, 761-779 (1972).

[180] S. Parodi, F. Kendall, C. Nicolini, NAR **2**, 477 (1975).

[181] D. Cheng, X. Chen, J. Wang, Z. Fang, Chemistry **13**(17), 4833-4839 (2007).

[182] S. Satpathi, A. Sengupta, V. M. Hridya, K. Gavvala, R. Koninti, B. Roy, P. Hazra, Scientific Report **5**, 9137 (2015).

[183] E. Zabost, A. Nowicka, M. Donten, Z. Stojek, Phys. Chem. Chem. Phys. **11**, 8933-8938 (2009).

[184] C. Bottari, I. Mancini, A. Mele, A. Gessini, C. Masciovecchio, B. Rossi, Proc. SPIE 11086, UV and Higher Energy Photonics: From Materials to Applications 2019, 110860Q

[185] W. Saenger, Principles of Nucleic Acid Structure, Springer-Verlag (1984).

[186] L. Movileanu, J. M. Benevides, G. J. Thomas, Biopolymers **63**, 181-194 (2002).

[187] H. E. Stanley, "Introduction to phase transition and critical phenomena", Clarendon Press, Oxford (1971).

[188] K. Shimizu, M. Tariq, M. F. C. Gomes, L. N. Rebelo, J. N. C. Lopes, J. Phys. Chem. B **114**, 5831-4 (2010).

[189] L. Santos, J. N. C. Lopes, J. A. P. Coutinho, J. Esperanca, L. R. Gomes, I. M. Marrucho, L. N. Rebelo, J. Am. Chem. Soc. **129**, 284 (2007).

[190] T. Koddermann, D. Paschek, R. Ludwig, ChemPhysChem **9**, 549 (2008).

[191] T. Umecky, M. Kanakubo, Y. Ikushima, J. Mol. Liq. **119**, 77-81 (2005)

[192] T. Afrin, S. N. Karobi, M. M. Rahman, M. Y. A. Mollah, M. A. B. H. Susan, J. Solution Chem. **42**, 1488-1499 (2013).

[193] J. H. Crowe, L. M. Crowe, D. Chapman, Science, **223**, 701-703 (1984).

[194] D. Corradini, E. G. Strekalova, H. E. Stanley, P. Gallo, Sci. Rep. **3**, 1218 (2013).

[195] L. Comez, M. Paolantoni, P. Sassi, S. Corezzi, A. Morresi, D. Fioretto, Soft Matter **12**, 5501 (2016).

[196] P. E. Mason, G. W. Neilson, J. E. Enderby, M. L. Saboungi and J. W. Brandy, J. Phys. Chem. B **109**, 13104-13111 (2005).

[197] G. Walrafen, J. Chem. Phys. **44**, 3726-3727 (1966).

[198] W. Saenger, T. Steiner, Water-Biomolecule Interactions, Bologna: SIF, (1993).

[199] A. Marini, V. Berbenni, G. Bruni, V. Massarotti, P. M. Villa, J. Chem. Phys. **103** ,7532 (1995).

[200] S. Li, W. C. Purdy, Chem. Rev. **92**, 1457 (1992).

[201] J. Szejtli, Chem. Rev. **98**, 1743 (1998).

[202] G. Crini, Chem. Rev. **114**, 10940 (2014).

[203] G. Astray, C. Gonzales-Barreiro, J. Mejuto, R. Rial-Oter, J. Simal-Gándara, Food Hydrocoll. **23**, 1613 (2009).

[204] M. E. Davis, M. E. Brewster, Nat. Rev. Drug Discov. **3**, 1023 (2004).

[205] R. Riahi, A. Tamayol, S. Shaegh, A. Ghaemmaghami, M. Dokmeci, A. Khademshosseini, Curr. Opin. Chem. Eng. **7**, 101 (2015).

[206] M. V. Rekharsky, Y. Inoue, Chem. Rev. **98**, 1875 (1998).

[207] L. Liu, Q. X. Guo, J. Inclusion Phenom. Macrocyclic Chem. **42**, 1 (2002).

[208] K. A. Connors, Chem. Rev. **97**, 1325 (1997).

[209] K. J. Naidoo, J. Y. J. Chen, J. L. M. Jansson, G. Widmalm, A. Maliniak, J. Phys. Chem. B **108**, 4236 (2004).

[210] R. G. Winkler, S. Fioravanti, G. Ciccotti, C. Margheritis, M. Villa, J. Comput. Aided Mol. Des. **14**, 659 (2000).

[211] M. Jana, S. Bandyopadhyay, J. Phys. Chem. B **115**, 6347 (2011).

[212] C. De Brauer, P. Germain, M. P. Merlin, J. Inclusion Phenom. Macrocyclic Chem. **44**, 197 (2002).

[213] E. Sabadini, T. Cosgrove, F. do Carmo Egıdio, Carbohydr. Res. **341**, 270 (2006).

[214] W. Cai, T. Sun, X. Shao, C. Chipot, Phys. Chem. Chem. Phys. **10**, 3236 (2008).

[215] A. R. Khan, P. Forgo, K. J. Stine, V. T. D'Souza, Chem. Rev. **98**, 1977 (1998).

[216] T. Irie, K. Uekama, J. Pharm. Sci. **86**, 147 (1997).

[217] C. W. Yong, C. Washington, W. Smith, Pharm. Res. **25**, 1092 (2008).

[218] T. Shikata, R. Takahashi, Y. Satokawa, J. Phys. Chem. B **111**, 12239 (2007).

[219] B. Rossi, L. Comez, D. Fioretto, L. Lupi, S. Caponi, F. Rossi, J. Raman Spectrosc. **42**, 1479 (2011).

[220] B. Rossi, L. Comez, L. Lupi, S. Caponi, F. Rossi, Food Biophys. **6**, 227 (2011).

[221] M. Jana, S. Bandyopadhyay, Langmuir **25**, 13084 (2009).

[222] M. Jana, S. Bandyopadhyay, Langmuir **26**, 14097 (2010).

[223] M. Jana, S. Bandhyopadhyay, J. Chem. Phys. **134**, 025103 (2011).

[224] M. Jana, S. Bandhyopadhyay, Chem. Phys. Lett. **509**, 181 (2011).

[225] V. Venuti, B. Rossi, V. Crupi, F. D'Amico, A. Gessini, D. Majolino, C. Masciovecchio, R. Stancanelli, C. A. Ventura, J. Phys. Chem. B **120**, 3746 (2016).

[226] C. Branca, S. Magazú, G. Maisano, P. Migliardo, J. Chem. Phys. **111**, 281 (1999).

[227] A. Lerbret, P. Bordat, F. Affouard, Y. Guinet, A. Hedoux, L. Paccou, D. Prevost, M. Descamps, Carbohydr. Res. **340**, 881 (2005).

[228] W. B. Monosmith, G. E. Walrafen, J. Phys. Chem. **81**, 669 (1984).

[229] J. L. Green, A. R. Lacey, M. G. Sceats, J. Phys. Chem. **90**, 3958 (1986).

[230] G. E. Walrafen, Y. C. Chu, J. Phys. Chem. **99**, 11225 (1995).

[231] G. E. Walrafen, J. Chem. Phys. **120**, 4868 (2004).

[232] J. D. Eaves, J. J. Loparo, C. J. Fecko, S. T. Roberts, A. Tokmakoff, P. L. Geissler, Proc. Natl. Acad. Sci. U. S. A. **102**, 13019 (2005).

[233] P. Sassi, M. Paolantoni, R. S. Cataliotti, F. Palombo, A. Morresi, J. Phys. Chem. B **108**, 19557 (2004).

[234] A. Di Michele, M. Freda, G. Onori, M. Paolantoni, A. Santucci, P. Sassi, J. Phys. Chem. B **110**, 21077 (2006).

[235] V. S. Marinov, Z. S. Nickolov, H. Matsuura, J. Phys. Chem. B **105**, 9953 (2001).

[236] M. Paolantoni, L. Comez, D. Fioretto, M. E. Gallina, A. Morresi, P. Sassi, F. Scarponi, J. Raman Spectrosc. **39**, 238 (2008).

[237] M. Paolantoni, N. Faginas Lago, M. Albertí, A. Laganá, J. Phys. Chem. A **113**, 15100 (2009).

[238] D. De Rossi, K. Kajiwara, Y. Osada. A. Yamauchi, Polymer Gels, Plenum, New York (1991).

[239] Y. Osada, K. Kajiwara, Gel Handbook, Academic Press, New York (2001).

[240] N. A. Peppas, B. V. Slaughter, M. A. Kanzelberger in: Hydrogels, in Comprehensive Polymer Science **9**, (2011).

[241] O. Wichterle, D. Lim, Nature, **185**, 117 (1960).

[242] L. A. Sharpe, A. M. Daily, S. D. Horava, N. A. Peppas, Expert Opin. Drug Delivery **11**, 901 (2014).

[243] J. X. Cui, D. P. Wang, K. Koynov, A. del Campo, ChemPhysChem **14**, 2932 (2013).

[244] G. B. Demirel, R. von Klitzing, ChemPhysChem **14**, 2833 (2013).

[245] A. S. Hoffman, Adv. Drug Delivery Rev. **54**, 3 (2002).

[246] N. A. Peppas, P. Bures, W. Leobandung, H. Ichikawa, Eur. J. Pharm. Biopharm. **50**, 27 (2002).

[247] P. Gupta, K. Vermani, S. Garg, Drug Discovery Today **7**(10), 569 (2002).

[248] A. V. Reis, M. R. Guilherme, O. A. Cavalcanti, A. F. Rubira, E. C. Muniz, Polymer **47**, 2023 (2006).

[249] Q. Wei, F. Fu, Y. Zhang, L. Tang, J. Polym. Res. **22**, 15 (2015).

[250] S. L. Banerjee, M. Khamrai, P. P. Kundu, N. K. Singha, RSC Adv. **6**, 81654 (2016).

[251] T. R. Hoare, D. S. Kohane, Polymer **49**, 1993 (2008).

[252] Z. Chen, L. Xu, Y. Liang, M. Zhao, Adv. Mater. **22**, 1488 (2010).

[253] V. Yesilyurt, M. J. Webber, E. A. Appel, C. Godwin, R. Langer, D. G. Anderson, Adv. Mater. **28**, 86 (2016).

[254] L. Klouda and A. G. Mikos, Eur. J. Pharm. Biopharm. **68**, 34 (2008).

[255] G. H. Chen, A. S. Hoffman, Nature **373**, 49 (1995).

[256] C. A. Schoener, H. N. Hutson, G. K. Fletcher, N. A. Peppas, Ind. Eng. Chem. Res. **50**, 12556 (2011).

[257] W. B. Liechty, M. Caldorera-Moore, M. A. Phillips, C. Schoenerand, N. A. Peppas, J. Controlled Release **155**, 119 (2011).

[258] A.P. Sherje, B.R. Dravyakar, D. Kadam,M. Jadhav, Carbohydr. Polym. **173** 37-49, (2017).

[259] F. Caldera, M. Tannous, R. Cavalli, M. Zanetti, F. Trotta, Int. J. Pharm. **531**(2), 470-479 (2017).

[260] V. Venuti, B. Rossi, A. Mele, L. Melone, C. Punta, D. Majolino, C. Masciovecchio, F. Caldera, Expert Opin. Drug Deliv. **14**(3), 331-340 (2017).

[261] D. Lembo, F. Trotta, R. Cavalli, Nanomedicine (2018).

[262] G. S. Longo, I. Szleifer, J. Phys. D: Appl. Phys. **49**, 323001 (2016).

[263] N. A. Peppas, J. Z. Hilt, A. Khademhosseini, R. Langer, Adv. Mater. **18**, 1345 (2006).

[264] S. Lehmann, S. Seiffert, W. Richtering, J. Am. Chem. Soc. **134**, 15963 (2012).

[265] B. Amsden, Macromolecules **31**, 8382 (1998).

[266] Y. Sekinea, T. Ikeda-Fukazawa, J. Chem. Phys. **130**, 034501 (2009).

[267] M. N. Olejniczak, M. Kozanecki, J. Saramak, M. Matusia, S. Kadlubowski, K. Matyjaszewskia, J. Raman Spectrosc. **48**, 465 (2017).

[268] M. Pastorczak, M. Kozanecki, J. Ulansky, Polymer **50**, 4535 (2009).

[269] B. Rossi, V. Venuti, F. D'Amico, A. Gessini, F. Castiglione, A. Mele, C. Punta, L. Melone, V. Crupi, D. Majolino, F. Trotta, C. Masciovecchio, Phys. Chem. Chem. Phys. **17**, 963 (2015).

[270] B. Rossi, V. Venuti, A. Mele, C. Punta, L. Melone, V. Crupi, D. Majolino, F. Trotta, F. D'Amico, A. Gessini, C. Masciovecchio, J. Chem. Phys. **142**(1), 014901 (2015).

[271] B. Rossi, V. Venuti, A. Mele, C. Punta, L. Melone, F. D'Amico, A. Gessini, V. Crupi, D. Majolino, F. Trotta, C. Masciovecchio, Phys. Chem. Chem. Phys. **18**, 12252 (2016).

[272] G. Lepert, R. M. Gouveia, C. J. Connon, C. Paterson, Faraday Discuss. **187**, 415 (2016).

[273] P. Zhao, J. J. Vanderwal, Polym. Gels Networks **5**, 23 (1997).

[274] A. Adshead, S. M. Lindsay, Polymer **23**(13), 1884 (1982).

[275] S. Caponi, S. Corezzi, M. Mattarelli, D. Fioretto, J. Chem. Phys. **141**, 214901 (2014).

[276] P. Sassi, S. Caponi, M. Ricci, A. Morresi, H. Oldenhof, W. F. Wolkers, D. Fioretto, J. Raman Spectrosc. **46**, 644 (2015).

[277] B. Rossi, S. Caponi, F. Castiglione, S. Corezzi, A. Fontana, M. Giarola, G. Mariotto, A. Mele, C. Petrillo, F. Trotta, G. Viliani, J. Phys. Chem. B **116**(17), 5323 (2012).

[278] V. Venuti, B. Rossi, A. Mele, L. Melone, C. Punta, D. Majolino, C. Masciovecchio, F. Caldera, Expert Opin. Drug Delivery **14**(3), 331 (2017).

[279] B. Rossi, A. Paciaroni, V. Venuti, G. C. Fadda, L. Melone, C. Punta, V. Crupi, D. Majolino, A. Mele, Phys. Chem. Chem. Phys. **19**, 6022 (2017).

[280] B. Rossi, V. Venuti, F. D'Amico, A. Gessini, A. Mele, C. Punta, L. Melone, V. Crupi, D. Majolino, C. Masciovecchio, Soft Matter **12**, 8861 (2016).

[281] C. Bottari, L. Comez, S. Corezzi, F. D'Amico, A. Gessini, A. Mele, C. Punta, L. Melone, A. Pugliese, C. Masciovecchio, B. Rossi, Phys. Chem. Chem. Phys. **19**, 22555-22563 (2017).

[282] Z. Meng, T. Thakur, C. Chitrakar, M.K. Jaiswal, A.K. Gaharwar, V.V. Yakovlev, ACS Nano **11**(8), 7690-7696 (2017).

[283] B. Rossi, C. Bottari, L. Comez, S. Corezzi, M. Paolantoni, A. Gessini, C. Masciovecchio, A. Mele, C. Punta, L. Melone, A. Fiorati, A. Radulescu, G. Mangiapia, A. Paciaroni, J. Mol. Liq. **271**, 738-746 (2018).

[284] F. Scarponi, S. Mattana, S. Corezzi, S. Caponi, L. Comez, P. Sassi, A. Morresi, M. Paolantoni, L. Urbanelli, C. Emiliani, L. Roscini, L. Corte, G. Cardinali, F. Palombo, J.R. Sandercock, D. Fioretto, Phys. Rev. **X**(7), 031015 1-11 (2017).

[285] M. Ferro, F. Castiglione, C. Punta, L. Melone, W. Panzeri, B. Rossi, F. Trotta, A. Mele, Beilstein J. Org. Chem. **10**, 2715-2723 (2014).

[286] A. Radulescu, N.K. Szekely, M.S. Appavou, V. Pipich, T. Kohnke, V. Ossovyi, S. Staringer, G.J. Schneider, M. Amann, B. Zhang-Haagen, G. Brandl, M. Drochner, R. Engels, R. Hanslik, G. Kemmerling, J. Vis. Exp. **118**, e54639 (2016).

[287] G.D. Wignall, F.S. Bates, J. Appl. Crystallogr. **20**(1), 28-40 (1987).

[288] T.P. Russell, J.S. Lin, S. Spooner, G.D. Wignall, J. Appl. Crystallogr. **21**(6), 629-638 (1988).

[289] A. Radulescu, V. Pipich, H. Frielinghaus, M.-S. Appavou, KWS-2, J. Phys. Conf. Ser. **351**, 012026-1-13 (2012).

[290] M. Shibayama, Soft Matter **8**, 8030-8038 (2012).

[291] E. Mendes, A. Hakiki, J. Herz, F. Boue, J. Bastide, Macromolecules **37**, 2643–2649 (2004).

[292] F. Di Lorenzo, S. Seiffert, Polym. Chem. **6**, 5515-5528 (2015).

[293] J. Bastide, L. Leibler, Macromolecules **21**, 2647-2649 (1988).

[294] B. Hammouda, D. Ho, S. Kline, Macromolecules **37**, 6932-6937 (2004).

[295] M. Shibayama, Polym. J. **43**, 18-34 (2011).

[296] G. Scarcelli, W.J. Polacheck, H.T. Nia, K. Patel, A.J. Grodzinsky, R.D. Kamm, S.H. Yun,, Nat. Methods **12**(12), 1132-1134 (2015).

[297] B. Rossi, V. Venuti, F. D'Amico, A. Gessini, A. Mele, C. Punta, L. Melone, V. Crupi, D. Majolino, F. Trotta, C. Masciovecchio, Soft Matter **11**, 5862-5871 (2015).

[298] Y. Maeda, H. Kitano, Spectrochim. Acta A **51**, 2433-2446 (1995).

[299] A. Joachimiak, T. Halamus, P. Wojciechowski, J. Ulanski, J. Macromol. Chem. Phys. **206**(1), 59-65 (2005).

[300] B. Ratajska-Gadomska, W. Gadomski, J. Chem. Phys. **121**, 12583-12588 (2004).

[301] G.E. Walrafen, J. Chem. Phys. **47**, 114-126 (1967).

[302] X. Wei, W. Liang, W. Wu, C. Yang, F. Trotta, F. Caldera, A. Mele, T. Nishimoto, Y. Inoue, Org. Biomol. Chem. **13**, 2905 (2015).

[303] L. Lupi, L. Comez, C. Masciovecchio, A. Morresi, M. Paolantoni, P. Sassi, F. Scarponi, D. Fioretto, J. Chem. Phys. **134**, 055104 (2011).

[304] L. Comez, S. Corezzi, A. Orecchini, A. Paciaroni, C. Petrillo, S. C. Santucci, F. Sacchetti and D. Fioretto, J. Mol. Liq. **176**, 76 (2012).

[305] V. Crupi, D. Majolino, A. Mele, B. Rossi, F. Trotta, V. Venuti, Soft Matter **9**, 6457 (2013).